



UNIVERSITÀ DI PARMA

Università degli Studi di Parma

Dottorato di ricerca in Ingegneria Industriale

CICLO XXXII

Design and characterisation of polymeric nanocomposites for automotive sector by additive manufacturing technology

Coordinatore:

Chiar.mo Prof. Gianni Royer Carfagni

Tutore:

Chiar.ma Prof.ssa Federica Bondioli

Co-tutore:

Chiar.mo Prof. Rinaldo Garziera

Dottorando: *Dott. Gabriele Taormina*

Anni 2016/2019

And thank you for the evening of the night on which
I fell off my horse in the shadows. That was really useful.

Kenneth Koch – Thank you

Abstract

Additive manufacturing (AM) is emerging in recent years, not only as a rapid prototyping technique that can help the design steps, but more and more as a proper production mean with intrinsic advantages. However, one of the main limitations is, at the moment, the relative lack of materials suitable for this kind of production. This doctorate dissertation reports some of the efforts made to try to fill this gap, developing new functional AM materials to serve in the automotive sector, as well as in other industrial fields. The work here reported is focused on vat photopolymerisation (VP) techniques, a branch of AM technologies, for the production of polymer nanocomposites. In particular, unmodified commercial desktop stereolithographic printers (SLA) based on the laser scanning system was used, as well as prototypical stereo-thermo-lithographic printers based on the mask projection process. The developed polymer nanocomposite have acrylic mixtures matrixes and silver nanoparticles, graphite flakes or graphene sheets as fillers. The developed materials were characterised with different techniques to gather information on structural and functional properties. Mechanical and viscoelastic properties were increased significantly by the addition of fillers, as well as electrical properties, but, more remarkably, an innovative method for the production of nanocomposite materials was developed.

Acknowledgement

All the work of the last 3 years presented in this dissertation, has been made possible thanks to the funding of the Regione Emilia-Romagna, under the “Automotive Academy” project (POR FSE 2014/2020 Obiettivo tematico 10) with the scholarship for my Ph.D. position.

I would like to thank, first of all, my tutor Professor Federica Bondioli for the guidance and support and for all the things, scientific and non-scientific, that I learned from her.

I would also like to thank Professor Massimo Messori for co-tutoring my thesis, Professor Gianni Royer Carfagni and Professor Rinaldo Garziera for the support and interest in my PhD at UNIPR, Professor Elena Bassoli that was the first to believe that I was suitable for this role and that kindly provided support for the characterisation at CIGS in Modena, Dr Corrado Sciancalepore for all the help, the presence and the loyalty he showed me, but most of all for sending me that package when I was in need.

Moreover, I would like to thank Dr Rosa Taurino, Dr Francesca Bisi and (future) Dr Alberto Giubilini for the precious advices and the strong support that they all gave me, I will carry with me everything.

Also, I cannot forget to thank Professor Geoffrey Mitchell, vice director of CDRSP, for the trust and opportunity to visit his beautiful labs in Portugal and all the fellow researchers that welcomed me warmly and took care of me and my research along five unforgettable months of spring and summer. A special thank goes to João Ferreira Gil for the assistance with the setup of the machine and to João David Índio Pinheiro for the constant help but most importantly for the friendship and the truth and wisdom (and of course for saving me from sublimation, literally).

A special thanks to Vanessa Gatto from Allnex company that kindly provided a great part of the resins used, to her and to her company goes my gratitude for the hardly replaceable contribution.

I would also like to thank Professor Carlo Concari, Dr Alessandro Soldati and all the “Palazzina 4” team for the help in the interpretation and analysis of electrical data.

I would like to thank also Dino Boccaccini and Guglielmo Morini of Tecno Italia S.r.l. for the support during the development of our common project.

Now, informally, I would like to express all my gratitude and friendship to the fellows that shared a portion of their path with me. From the Parma campus: the “Gruppo Pranzo” Esse, Dario, Luso (the photo-contest is still open...), Emir, Bubee, Francesco, Carlo, Luca, Matte, Simo, Irina, Xenia, Giorgio and the occasional others, the physicists Silvio, Giacomo, Michi, Laura, Alberto, Daniele and Mauro, the other people from around the campus Alberto, Josef, Vinicius, Gabriel, Vanessa, Leticia, Davide, Luca, Davide, Sergiu, Miriam, Nello, Remis, Elena and all the others. From the Modena campus: Vitto, Rachel, Anto, Fra, Franci, Kate, Max, Alle, Stefania, Manu, Daniele, Veronica, Silvio, Richi, Fede and all the others. From Leiria and CDRSP: Hodhaifa, Zach, Yuri, Edgar, João(s), Cristiana, Pedro, Ricardo, Dora, Sachin, Paulo, Nance, Maryam, Thomas, Daniel, Margarida, Jorge, Juliana, Mauro, Carla, Saba, Catarina, Diana, Miguel, Sara, Renato and the others. The people I met in Gargnano: Sasan, Silvia, Rosaria, George and the others.

Special gratitude goes to my parents whom supported me since I was born and through all the stages of my instruction. I know today you can be proud of me. To my family and to my friends, and especially to those that belong to both categories, I give my gratitude. And to Ludovica, she knows for what.

Finally, I would like to thank Leiria city and Portugal in general for the warmth of the welcome, my supercar Honda Jazz for carrying me, the materials, the instruments and the samples everywhere (literally), the polar explorers for the lesson of stubbornness and success, the roman emperors for the lesson of greatness and its consequences, and Mario Draghi for the meaning of words and their power.

Table of content

Abstract	
Acknowledgement.....	
Table of content.....	
Table of figures.....	
Table of tables.....	
Introduction.....	1
1 State of the art.....	5
1.1 Definitions	5
1.2 Background, evolution, future trends.....	6
1.3 Fields of application	6
1.3.1 Automotive sector	7
1.4 Comparison with traditional production.....	9
1.4.1 AM production flow.....	10
1.5 AM: one family, many different technologies.	11
1.5.1 Powder bed fusion.....	13
1.5.2 Material extrusion.....	14
1.5.3 Material Jetting.....	15
1.6 Vat Photopolymerisation techniques.....	16
1.6.1 Stereolithography - SLA	16
1.6.2 Digital Light Processing - DLP	18
1.6.2.1 Micro-stereo-thermo-lithographic system - STLG.....	19
1.6.3 Two-photon polymerisation (2PP).....	20
1.6.4 Other techniques.....	21
1.6.4.1 Solution Mask Liquid Lithography - SMaLL.....	21
1.6.4.2 3D magnetic printing	22
1.6.5 Materials for VP	24
1.6.5.1 Photopolymer families and polymerisation types.....	24
1.6.5.1.1 Free-radical photopolymerisation.....	25
1.6.5.1.2 Cationic photopolymerisation	27
1.6.5.2 Composite and functional materials.....	27
1.6.5.2.1 Functional materials.....	27
1.6.5.2.1 Nanocomposites.....	30

1.6.6	Problems and limitations.....	33
1.6.6.1	Preparation treatments	34
1.6.6.2	Postprocessing.....	35
2	Materials and methods	37
2.1	Materials.....	37
2.1.1	Base monomers	37
2.1.1.1	PEGDA 250 - 700.....	38
2.1.1.2	PETIA	39
2.1.1.3	Ebecryl 7100.....	40
2.1.1.4	TMPTA.....	40
2.1.1.5	Other monomers for initial tests and matrix development	41
2.1.2	Fillers	50
2.1.2.1	Silver salts	50
2.1.2.1.1	Silver nitrate	52
2.1.2.1.2	Silver acrylate and methacrylate	52
2.1.2.1.3	Silver acetate.....	54
2.1.2.2	Copper salts.....	54
2.1.2.3	Sodium salts	55
2.1.2.3.1	Sodium acrylate	56
2.1.2.3.2	Sodium methacrylate	56
2.1.2.4	Graphite	56
2.1.2.5	TEGO (thermally expanded graphite oxide).....	57
2.1.3	Additives.....	58
2.1.3.1	Initiators	59
2.1.3.1.1	Photoinitiators.....	59
2.1.3.1.2	Thermoinitiators	59
2.1.3.2	Dyes (UV absorber)	61
2.1.3.3	Diluents	61
2.2	Technology	62
2.2.1	Hardware	62
2.2.1.1	Form 1+.....	62
2.2.1.2	Form 2.....	63
2.2.1.3	Stereo-thermo-lithographic system - STLG	64
2.2.1.4	Process parameters.....	68
2.2.1.4.1	Disposition on the build platform.....	68

2.2.1.4.2	Offset	72
2.2.1.4.3	Layer thickness.....	72
2.2.1.4.4	DLP and SLA process parameters.....	73
2.2.2	Software	73
2.2.2.1	Preform (with Openform)	73
2.2.2.2	STLG printer manager program.....	75
2.2.2.3	Electrical data measurement custom software	76
2.2.2.4	SolidWorks	76
2.2.2.4.1	Partial-contact models: a no-success story	77
2.3	Methods	79
2.3.1	Dispersion and homogenisation.....	79
2.3.1	Matrix initial tests under UV lamp	81
2.3.2	VP processes	82
2.4	Material Characterisation	91
2.4.1	Differential Scanning Calorimetry - DSC.....	91
2.4.2	X-ray diffraction - XRD	92
2.4.3	Scanning Electron Microscopy - SEM.....	92
2.4.4	Transmission Electron Microscopy - TEM.....	93
2.4.5	Dynamic-mechanical thermal analysis - DMTA	93
2.4.6	UV-Vis Spectrophotometer	95
2.4.7	Durometer.....	95
2.4.8	Fourier Transform Infrared Spectroscopy - FT-IR	95
2.4.9	Micro computer tomography - Micro-CT	96
2.4.10	Tensile and compression tests.....	96
2.4.10.1	Data conditioning and identification of the quasi-linear region.....	97
2.4.10.2	Mechanical data processing	97
2.4.11	Electrical properties test systems.....	98
2.4.11.1	Electrical data processing	99
2.4.11.2	Insulation tester.....	100
2.4.11.1	Homemade dynamic resistivity/conductivity tester	100
3	Results and discussion	103
3.1	Preliminary tests under UV lamp.....	103
3.2	Unfilled SLA samples: PEGDA 250-700 – thermo-mechanical properties modulation	103
3.2.1	Results - PEGDA 250-700.....	104
3.2.1.1	DSC	104

3.2.1.2	FTIR	105
3.2.1.3	Tensile characterisation.....	106
3.2.1.4	DMTA characterisation.....	107
3.2.2	Discussion - PEGDA 250-700	109
3.2.3	Conclusions - PEGDA 250-700.....	111
3.2.4	Application (ceramic industry patent).....	111
3.3	Filled samples.....	114
3.3.1	SLA - AgNPs – simultaneous photopolymerisation and in situ photoreduction of AgNPs	114
3.3.1.1	Results	114
3.3.1.1.1	XRD analysis	114
3.3.1.1.2	TEM micrographs	115
3.3.1.1.3	DSC Analysis.....	116
3.3.1.1.4	Tensile properties	118
3.3.1.1.5	DMTA properties.....	119
3.3.1.1.6	Creep Properties	120
3.3.1.2	Discussion.....	121
3.3.1.3	Conclusions	123
3.3.2	STLG – Ag, graphite and TEGO composites	124
3.3.2.1	Results (and discussion)	125
3.3.2.1.1	DSC.....	125
3.3.2.1.2	FTIR	127
3.3.2.1.3	XRD.....	128
3.3.2.1.4	Micro computer tomography - m-CT	129
3.3.2.1.5	Compression.....	130
3.3.2.1.6	Conductivity.....	133
3.3.3	Discussion (final considerations).....	134
3.3.4	Conclusion	137
3.4	“Failures” (that is opportunities).....	138
3.4.1	Silver nitrate in situ reduction	138
3.4.2	TEGO compatibility and dispersion issues.....	139
3.4.3	Graphene synthesis inside monomer.....	140
3.4.4	Partial-contact models: a no-success story (see section 2.2.2.4.1).....	141
3.4.5	Copper.....	141
3.5	Future perspectives	142

3.5.1	Variation in the filler concentration, addition and combination of different fillers	142
3.5.2	The variation of process parameters	143
3.5.3	GO: in situ photo-reduction to enhance conductivity	143
	Conclusion	i
	References	iv
	Appendix A - Publications	xiv
	Appendix B – Patent.....	xv
	Appendix C - Conferences.....	xvi
	Oral presentations.....	xvi
	Poster presentations	xvii

Table of figures

Figure 1: AM market slices according to 2016 Wohlers' report	7
Figure 2: (a) F1 upright (right) cast via rapid casting process using polystyrene patterns produced by SLS (left) (Source: CRP Technology http://www.crptechnology.com); (b) suspension mounting bracket for Red Bull Racing produced by LENS (Source: Optomec http://www.optomec.com); (c) race car gear box produced by EBM (Source: Arcam http://www.arcam.com); (d) exhaust manifold produced by SLM (Source: Concept Laser http://www.concept-laser.de); (e) oil pump housing produced by SLM (Source: Concept Laser http://www.concept-laser.de); (f) engine block cast using the mould and cores fabricated by 3DP (Source: Prometal http://www.prometal-rct.com)	8
Figure 3: a scheme of the entire additive manufacturing process, from the conceptual design to the final product. On the left the software processes, on the right the hardware processes and in the centre the product.....	10
Figure 4: AM technological families, with more detail for the VP [1].....	13
Figure 5: Powder Bed Fusion process scheme.....	14
Figure 6 Material Extrusion process scheme	15
Figure 7: Material Jetting process scheme	16
Figure 8: SLA process scheme.....	17
Figure 9 inverted SLA process scheme	18
Figure 10 DLP process scheme	19
Figure 11: STLG process scheme	20
Figure 12: 2PP process scheme	21
Figure 13: SEM micrographs of untreated surfaces of cones printed by SMaLL (a) and SLA (b) [84]	22
Figure 14: radical polymerisation initiation and propagation scheme of PEGDA activated by the photocleavage of the Irgacure 819 photoinitiator	26
Figure 15: PEGDA molecular structure	39
Figure 16: PETIA pentaerythritol triacrylate molecular structure.....	39
Figure 17: PETIA pentaerythritol tetraacrylate molecular structure.....	40
Figure 18: HDDA molecular structure	40
Figure 19: TMPTA molecular structure.....	41

Figure 23: silver acrylate (a) and methacrylate (b) synthesis reaction scheme	53
Figure 27: SEM images of GO vigorously exfoliated at 1323 K (TEGO).....	58
Figure 28: representative TEM image from TEGO, where stacked graphene sheets are present. Here a single layer sheet with a prominent tear and crumpling at the edge is observed. Scale bar indicates 100 nm	58
Figure 29: Bis-(2,4,6-trimethylbenzoyl)-phenylphosphine oxide (Irgacure 819) molecular structure	59
Figure 30: benzoyl peroxide molecular structure	60
Figure 31: 2,2'-Azobis(2-methylpropionitrile) molecular structure.....	60
Figure 32: 1-Phenylazo-2-naphthol (Sudan I) molecular structure	61
Figure 33: Form 1+ components scheme	62
Figure 34: inside of Form 1+ case [132]	63
Figure 35: Form 2, Formlabs.....	64
Figure 36: a photograph of the STLG printing system.....	66
Figure 37: FSR-BG38 blue glass bandpass filter (left) and 10LF30-1550 IR bandpass filter (right)...	66
Figure 38: FSR-BG38 Blue Glass Bandpass Filter transmission diagram.....	67
Figure 39: extinction diagram of Irgacure 819	67
Figure 40: photomask for the DMD, 1024 x 768 pixels	67
Figure 41: poor disposition of the samples on the build platform too close to the hinge on the right	68
Figure 42: effects of the overcuring on the printed samples due to the poor disposition.....	69
Figure 43: a better sample disposition, far from the hinge side	70
Figure 44: better sample disposition results, the sample on the right is still somehow slightly overcured.....	70
Figure 45: another better sample disposition, far from the hinge side and asymmetrical.....	71
Figure 46: staircase effect depending on the layer thickness: finer (a) and higher (b).....	72
Figure 47: Preform interface	74
Figure 48: process parameters available with Openform	74

Figure 49: paths of the laser scan applied for each model slice, the perimeter is considered differently from the bulk	75
Figure 50: the three different regions of an additive manufactured object: the base attached to the build platform, the supports and the model.....	75
Figure 51: software for the programming of the Genuino 101 microcontroller	76
Figure 52: SolidWorks interface.....	77
Figure 53: a micro-CT image of a STLG printed sample (i) and the images of the models used: linear (a), pyramid convex (b), pyramid concave (c), barrel convex (d), barrel concave (e), paraboloid convex (f), paraboloid concave (g)	79
Figure 54: UP200Ht ultrasonic tip, Hielscher	80
Figure 55: T 25 digital ULTRA-TURRAX, IKA.....	80
Figure 56: NEYA 16, REMI Neya Centrifuges.....	81
Figure 57: double glass slide mould for initial test under UV lamp	82
Figure 58: a scheme of the entire SLA process for unfilled samples, from the preparation of the formulations and CAD design to the post-treatments	83
Figure 59: An image of printed samples	84
Figure 60: a scheme of the entire SLA process for silver nanocomposites, from the preparation of the formulations and CAD design to the post-treatments	85
Figure 55: 3D printed specimens: (a) unfilled; (b) 0.5% AgAcr; (c) 1% AgAcr; (d) 2% AgAcr; and (e) 1% AgMAcr.	86
Figure 56: Scheme of the expected reactions during the 3D printing process (b).	87
Figure 63: a scheme of the entire STLG process for silver, graphite and TEGO composites, from the preparation of the formulations and DMD set up to the post-treatments	88
Figure 64: 3D printed specimens: i) control; ii) AgMAcr; iii) m-G; iv) TEGO	91
Figure 77: representative stress-strain curve of a TEGO filled sample processed through STLG. The image shows the mechanical quasi-linear strain and the process to obtain it	98
Figure 78: representative conductivity-strain curve of a TEGO filled sample processed through STLG. The image shows the electrical quasi-linear strain and the process to obtain it, as well as the unique value of conductivity.	100
Figure 80: schematic representation of the circuit for the experimental setup	101
Figure 81: model of the assembly to the compression plates of the holders for the electrical testing.	101

Figure 82: schematic representation of the circuit used.....	102
Figure 83: differential scanning calorimetry (DSC) thermogram (exothermic up) of PEGDA 250 before (PEGDA A NT) and after (PEGDA A UV) post-treatment. Sample PEGDA A is shown as representative.....	104
Figure 84: Fourier transform infrared spectra (FTIR) of PEGDA 700 before (a) and after (b) SLA printing and UV treatment. Only the PEGDA 700 spectra are reported here as representative of the other formulations that exhibited the same behaviour.....	105
Figure 85: Representative stress-strain diagram with each formulation displayed.....	106
Figure 86: dynamic-mechanical thermal analysis (DMTA) thermograms of the storage modulus (E') of the five different formulations.....	108
Figure 87: dynamic-mechanical thermal analysis (DMTA) thermograms of the Tan Delta of the five different formulations.....	108
Figure 88: dynamic-mechanical thermal analysis (DMTA) thermograms of the loss modulus (E'') of the five different formulations.....	109
Figure 89: the printed polymeric pad with the surface to impress on the ceramic powders	112
Figure 90: the pressed ceramic powder forming a green tile	113
Figure 91: another example of pressed ceramic powder forming a green tile.....	113
Figure 92: X-ray diffraction (XRD) diffraction pattern of 3D printed materials containing different amount of AgNPs from AgAcr and AgMAcr as precursors.....	115
Figure 93: Transmission electron microscopy (TEM) micrographs at two different magnifications of "Unfilled" (a,e); "AgAcr 1%" (b,f); "AgAcr 2%" (c,g); and "AgMAcr 1%" (d,h); as representative.	116
Figure 94: Differential scanning calorimetry (DSC) thermograms (exo up) of "Unfilled", "AgAcr x%" and "AgAcr 1%" (TT: after thermal treatment; NT: no thermal treatment; I: first heating scan, II: second heating scan).....	117
Figure 95: Representative stress-strain diagram for Ag-filled and unfilled samples.....	118
Figure 96: Relative storage modulus as a function of AgNPs volume fraction. A comparison between predicted and experimental values for the AgAcr filled series.....	120
Figure 97: Master curves of compliance as a function of time at the reference temperature of 10 °C for "Unfilled", "AgAcr x%", and "AgMAcr 1%" samples.....	121
Figure 98: expected reactions during STLG 3D printing process, photodegradation of the photoinitiator and radical polymerisation initiation and propagation. In the central box, the silver ions reduction, nucleation and growth.....	124

Figure 99: differential scanning calorimetry (DSC) thermograms (exothermic up) of all the different composition printed specimens (first two heating scans shown).....	126
Figure 100: FTIR spectra of the liquid monomer mixture and of the 3 loaded composition printed samples.....	128
Figure 101: X-ray diffraction pattern of 3D printed material containing 0.5% w/w AgNPs from AgMAcr as precursor. In red the position of the diffraction peaks of metallic Ag as shown in the peak list (JCPDS 04-0783).....	129
Figure 102: virtual cross sections of the fabricated objects made with micro computer-tomography (m-CT):. (I) control; (II) Ag; (III) m-G; (IV) TEGO.....	130
Figure 103: test direction, Z axis on the left and XY plane on the right. The layers and their direction are clearly visible.	131
Figure 104: representative stress-strain curves for the 3D printed samples.	132
Figure 105: representative conductivity vs strain curves of the 3D printed samples	134
Figure 106: ϵ_{ql^m} ϵ_{ql^e} “quasi linear strain” values derived from mechanical (ϵ_{ql^m}) and electrical (ϵ_{ql^e}) data processing.	136
Figure 107: XRD diffraction pattern of an untreated samples right after SLA process, the silver nitrate is largely unreacted or oxidised, with just traces of metallic silver	139
Figure 108: TEGO filled samples at different concentration (a) unfilled, (b) 0.005%, (c) 0.01%, (d) 0.05%, (e) 0.1%. at low concentration (b, c) the small black dots are the visible aggregates.....	140
Figure 109: copper nitrate 0.01 M in 10 ml EtOH, Ir 819 0.02 M, ethanolamine as reducing agent 0.04 M, 3 minutes ultrasonic dispersion of the salt, 1 to 60 minutes UV lamp.	142

Table of tables

Table 1: materials processed by AM and their process family [14].	12
Table 2: table of all the monomers, and their relevant properties, used to test and optimise the matrix formulations [122].	42
Table 3: table of all the silver salts used as silver nanoparticles precursors or as direct fillers or in the synthesis of other silver salts.	51
Table 4: table of all the copper salts used and of their main properties.	55
Table 5: a table of the sodium salts used and of their main properties.	56
Table 6: technical specifications comparison between Form1+ and Form 2.	64
Table 7: table of the five different formulations prepared highlighting the relative percentages of the two monomers.	83
Table 8: prospect summing up the main process parameters used to print the four different sample types.	89
Table 9: mean values and standard deviations of tensile strength, tensile strain at break and Young's modulus.	107
Table 10: characteristic temperatures and moduli of the different printed formulations, respectively E' and E'' at 25 °C, T_g at $\tan \delta$ maximum.	109
Table 11: Tensile properties of 3D printed specimens (E_t : Young's modulus; σ_M : tensile strength; σ_B : tensile strain at break, according to ISO 527 technical standard).	119
Table 12: Glass transition temperature (T_{gDMTA} , evaluated as temperature value corresponding to $\tan \delta$ peak) and storage modulus at 60 °C values for all the printed specimens, from DMTA analyses.	120
Table 13: volume and porosity of the samples used for m-CT scans.	129
Table 14: tensile properties of 3D printed specimens tested on xy direction (E : Young's modulus; UCS: ultimate compression strength; ϵ_B compression strain at break).	132
Table 15: tensile properties of 3D printed specimen tested on z direction (E : Young's modulus; UCS: ultimate compression strength; ϵ_B compression strain at break).	132
Table 16: conductivity values in xy direction.	133
Table 17: conductivity values in z direction.	134
Table 18: duration of compression tests in xy direction.	135

Table 19: duration of compression tests in z direction..... 135

Table 20: “quasi linear strain” values derived from mechanical (ϵ_{ql}^m) and electrical (ϵ_{ql}^e) data processing for specimens in xy direction. The ratios between those quantities are reported as a proof of the goodness of the procedure..... 136

Table 21: “quasi linear strain” values derived from mechanical (ϵ_{ql}^m) and electrical (ϵ_{ql}^e) data processing for specimens in z direction. The ratios between those quantities are reported as a proof of the goodness of the procedure. 136

Introduction

The research work presented in this doctorate thesis was financed by the Regione Emilia-Romagna under the project “Automotive academy: a learning by doing project for the innovation in vehicle engineering”. The project aim was to investigate the connection between additive manufacturing (AM) and automotive industry, specially the racing sector, to spin innovation in an “old” industry with a “new” technology.

This dissertation, in particular, focuses on the design, production and characterisation of polymer nanocomposites with functionalisation (e.g. electrical, mechanical, thermo-mechanical, antimicrobial) suitable for, but not limited to, automotive sector. It was tried to maintain an innovative approach not only for the development of the materials themselves, but also for the AM methods and in the ways these methods were applied.

The first, most versatile and most precise AM technology, stereolithography and vat photopolymerisation processes (VP) in general, was considered. Moreover, innovative materials such as graphene was included in the research process.

The project became international, with numerous collaborations that added ideas, materials, expertise and helped consistently to the development of the whole work. Collaborations were established, within the University of Parma, with the Professor Carlo Concari research group (Department of Engineering and Architecture) and the Professor Mauro Riccò research group (Department of Mathematical Physical and Computer Sciences), outside with University of Modena and Reggio Emilia, Professor Massimo Messori research group (Department of Engineering “Enzo Ferrari”) and Politecnico di Torino (Applied Science and Technology Department), and abroad with the Centre for Rapid and Sustainable Product Development (CDRSP) of the Polytechnic Institute of Leiria (Portugal).

How do competition and high level sport vehicles combine with the opportunities of AM, and how can AM in general, and VP processes in particular, meet the requirements of such sector? Automotive high-level sector needs a lot of personalisation, both for luxury customised solutions and for ever-changing competitions needs where a fast production of

Introduction

new parts in small quantities is always required. AM can provide solutions to both these necessities, supplying a rapid method to produce parts with a high level of complexity and diversity without impacting on the production cost. For traditional technologies, on the contrary, customisation is something that impacts heavily on the production costs and times.

Another important aspect to be considered in the design and production of vehicles (as well as in other important sectors, like aerospace) is lightness. AM can face this need in three ways.

It can provide lightness by means of the reduction of the volume (and consequently mass) of the component by means of the so-called “topological optimisation”. Topological optimisation is a technique through which a component is redesigned to withstand all the solicitations and stresses occurring, but with the subtraction of all the superfluous material. Traditional methods of production are bounded by time, cost and technological intrinsic limitations, to the fabrication of somehow regular forms. On the contrary, AM can produce quasi-arbitrary geometries with the same time and cost of any other traditional form, but without the limitations of subtractive manufacturing. This opportunity gives the chance to lighten the components choosing the best geometry that fulfils the structural needs, unlocking the possibilities of topological optimisation.

Lightness can be achieved with AM also by drastically diminishing the components of a complex assembly, the minor quantity of coupling systems will decrease the total weight.

The last way in which AM can reduce weight in vehicles is represented by the metal replacement. Metal replacement is the practise of substituting metal parts mainly with polymeric or composite materials, even for structural applications. The development of new polymeric and composite materials for AM can supply new solutions for the metal replacement strategy.

That is why AM and material development are important for automotive sector. The combination of these three factors can produce significant reduction in the weight of a vehicle, enhancing performances and lowering consumption and thus the impact on the environment.

Introduction

The mere reduction of weight can also be accompanied by the functionalisation of the material. Nanofillers can give many different functionalities to the matrix, enhancing the existing properties or bringing new ones.

The thesis is structured in chapters. The first chapter recalls the state of the art for AM and was used for the review “3D printing processes for photocurable polymeric materials: technologies, materials and future trend” published in 2018 [1]. The main definitions are presented together with a short report on AM history, evolution and future trends. A deeper analysis on the different fields of application is then presented with a special focus on automotive sector. A short comparison with the traditional production methods is followed by an analysis of the AM production flow, then the attention shifts on the AM processes. A short presentation of the main families of processes (powder bed fusion, material extrusion and material jetting) is given before focusing on the VP processes. Stereolithography, digital light processing and stereo-thermo-lithography (STLG) are explained and discussed, as well as other minor VP techniques. Afterwards, it comes a section on VP processable materials. The photopolymer families with their specific polymerisation reaction mechanisms are presented before shifting the focus on a composite and functional materials overview. The problems and limitations occurring during the VP processes, including preparation and post-processing steps, are then explored.

The second chapter reports the materials and methods adopted during the research work in laboratory and in the treatment and interpretation of data and results. Firstly, the different base monomers are presented, followed by the fillers and necessary additives. Afterwards, it comes a technological overview on both hardware (the different printers used with their process parameters) and software aspects (the programs to control printers, to get and interpret data, and to design parts). Then it comes a method section where initial tests procedures, dispersion and homogenisation issues, silver nanoparticle synthesis and the VP processes workflows are reported. The subsequent section is dedicated to the material characterisation. The different characterisation techniques are presented together with a description of the adopted instrument. Special attention is given to the simultaneous compression and electrical conductivity test that was developed specifically for this research project.

Introduction

The third chapter, results and discussion, deals with the outcomes of the different research branches investigated. The published results, and those under publication, are here presented and discussed [2]. The first section is about unfilled SLA samples obtained with PEGDA with different molecular weight for a modulation of the mechanical and viscoelastic properties. A section on filled samples follows the first one, starting with silver nanoparticles (AgNPs) filled samples obtained in a SLA double simultaneous process of photopolymerisation and *in situ* reduction of silver precursor salts. Afterward, an entire section is dedicated to the STLG samples filled with AgNPs, micrometric graphite and nanostructured heavily-reduced graphene oxide (TEGO), the focus of this last project is the enhancement of electrical conductivity and the comparison of the action of different fillers on the composite properties.

The results chapter is completed by two sections. The first and less orthodox one is a section named “failures” (that is opportunities), in which the problems and issues emerged during this work are presented. The section is based on the presupposition that errors are the best teachers and “to research” does not always mean “to find”. Some hypothetical solutions are given together with the reported problem, and strategies to overcome the obstacles are presented. The other section that completes the results chapter is the future perspectives section, where some interesting possible developments and implementable solutions are hypothesised.

Another important paragraph of the results chapter is the one that reports an application specifically developed, in collaboration with a company of the ceramic industry sector, to apply AM to ceramic tile surface structuring. This applied research resulted in the presentation of a patent.

A conclusion final chapter summarise all the thesis and usefully recalls all the main concepts and results.

1 State of the art

This chapter was used for the review published during this research titled “3D printing processes for photocurable polymeric materials: technologies, materials and future trend” [1]. The paper was updated and correlated with additional material.

1.1 Definitions

Additive manufacturing (AM), as defined by the ASTM F2792 – 12a Standard Terminology for Additive Manufacturing Technologies [3], is the process of joining materials to make objects from 3D model data, usually layer upon layer, as opposed to subtractive manufacturing methodologies. Despite of its broad use, the term “3D printing” (3DP) refers only to a single AM technology and moreover it is a registered trademark. So, it is wrong to address all the AM processes as 3DP.

AM technologies have been initially collectively known as rapid prototyping (RP) because of their main use as a cheap, lean and quick way to produce prototypes for parts or products that, once developed, would have been produced in a traditional subtractive manufacturing way. Since in the recent years more and more parts and products have been produced directly with AM technologies, the term RP has declined. Now it is perfectly common in many industrial sectors to use AM machines directly for the production, especially but not limited to sectors that can take real advantages from the intrinsic capabilities of AM process: most of all its versatility and low set up costs. Those characteristics translate into a strong advantage in terms of personalisation and geometric freedom [4].

1.2 Background, evolution, future trends

Since photopolymers have been firstly developed in the 60's they have been used for many different sectors from dentistry to coatings industry. But it is only in 1986 that Chuck Hull, an American engineer, patented an "Apparatus for Production of Three-Dimensional Objects by Stereolithography" [5]. Additive manufacturing was born, or at least its earliest technology: the stereolithography. Stereolithography is described as a method to make solid objects by successively "printing" thin layers of the UV curable polymer one on top of the other. Since then, all the other main AM technologies have been invented and developed. A significant increase to the distribution and impact of these technologies is coming also from the expiring of the old patents of the 80's and 90's. This "liberalisation" spins the research and the industrial world into this relevant part of the 4th industrial revolution [6–8].

1.3 Fields of application

It is now more than 30 years since AM commercial technological development has become. Since the beginnings, the processes had become more accurate and rapid, bringing to higher mechanical properties. The machines and the construction of the parts have become less expensive and the constant increase of different technologies and materials brought to a significant increase in the range of applications. The three major trending applications for AM technologies are biomaterials, aerospace and automotive [4,9,10]. Even if nowadays AM can find applications in almost every consumer product sector, those three sectors can particularly take advantage from the intrinsic capabilities of AM process. Automotive industries and aero-space sector can benefit mostly from saving time in the product development while biomaterials can take advantage from the great customisation potential of AM.

1.3.1 Automotive sector

The Wohlers' report (Figure 1) shows that automotive industry accounts for 13.8% of the entire AM market, the second largest sector following aerospace.

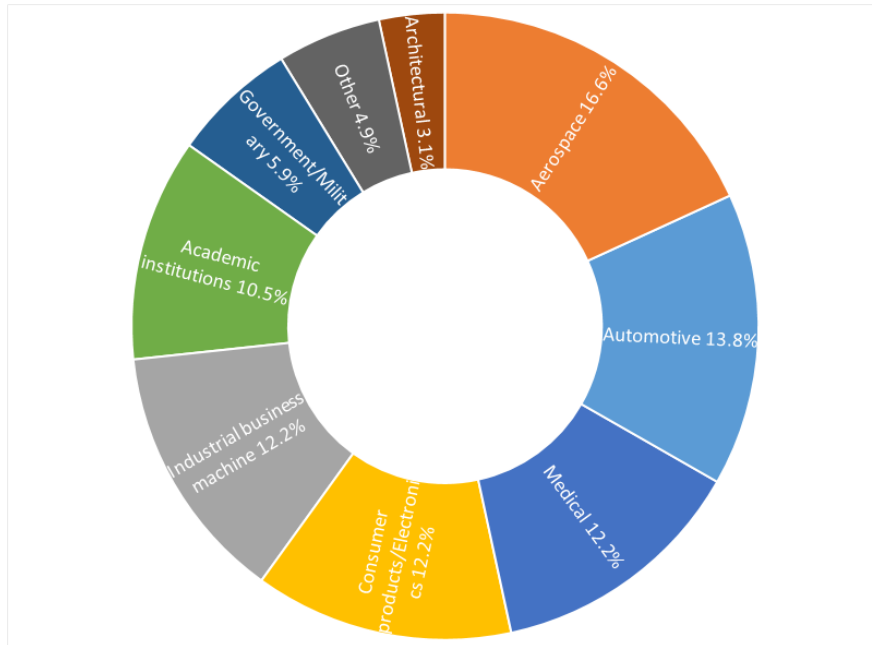


Figure 1: AM market slices according to 2016 Wohlers' report

AM techniques are considered ideal for automotive components because of their specific necessities:

- Complex geometry
- Customisation
- On demand manufacturing
- Lightness and topological optimisation

State of the art

The automotive industry has an increasing necessity to develop new products in ever shorter times. AM can face this need by supplying a shorter development cycle decreasing costs of production and manufacturing. Moreover, AM has also been applied to the production of small batches of functional parts mainly intended for luxury or motorsport low volume vehicles. For those small quantities of high level products, the customisation and on demand manufacturing guaranteed by the AM is very valuable.

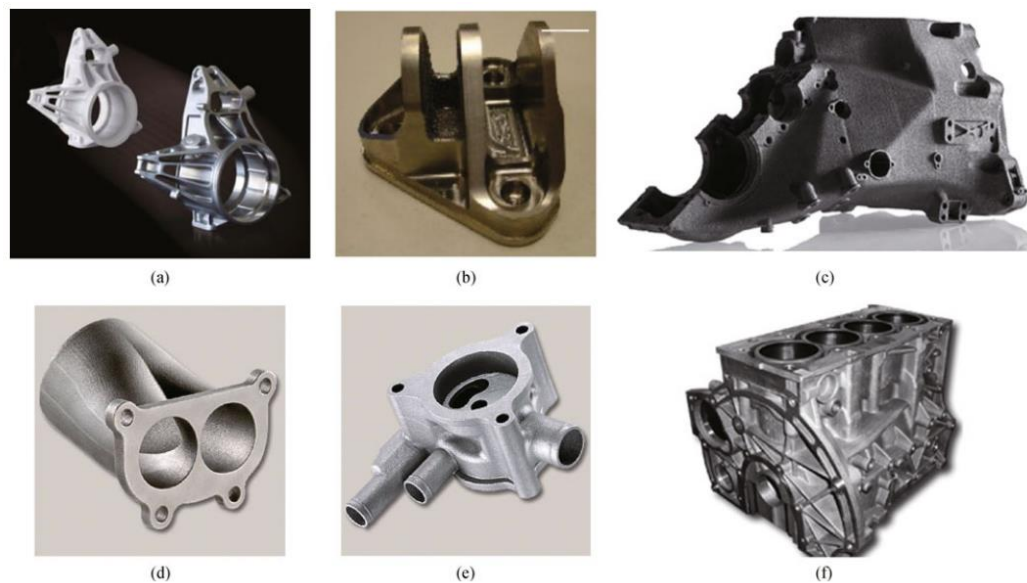


Figure 2: (a) F1 upright (right) cast via rapid casting process using polystyrene patterns produced by SLS (left) (Source: CRP Technology <http://www.crptechnology.com>); (b) suspension mounting bracket for Red Bull Racing produced by LENS (Source: Optomec <http://www.optomec.com>); (c) race car gear box produced by EBM (Source: Arcam <http://www.arcam.com>); (d) exhaust manifold produced by SLM (Source: Concept Laser <http://www.concept-laser.de>); (e) oil pump housing produced by SLM (Source: Concept Laser <http://www.concept-laser.de>); (f) engine block cast using the mould and cores fabricated by 3DP (Source: Prometal <http://www.prometal-rct.com>)

Examples from automotive industry [9]:

Suspension systems and gearboxes have been produced by CRP Technology for F1 and MotoGP [CRP Technology. <http://www.crptechnology.com>] (Figure 2a), Optomec applied AM to the fabrication of components such as suspension mounting brackets and drive shaft spiders for the Red Bull Racing cars, saving more than 90% of the material and reducing significantly times and costs [Optomec. <http://www.optomec.com>] (Figure 2b). Arcam produced Ti6Al4V parts for gearboxes, suspensions and engine components for race

cars [Arcam A B. <http://www.arcam.com>] (Figure 2c). Concept Laser applied AM to the fabrication of many aluminium and steel parts such as suspensions, manifolds, engine and valve blocks [Concept Laser GmbH. <http://www.concept-laser.de>] (Figure 2d-e). Prometal exploited AM for engine components, such as cylinder heads, intake manifolds, and engine blocks for passenger and race vehicles [Prometal RCT. <http://www.prometal-rct.com>] (Figure 2f).

Examples from automotive-related research in academia:

Research centres and universities around the world also set their interest to AM technologies for automotive applications. A water pump for motorsport cars has been developed using AlSi10Mg and no mechanical properties loss was found with the conventionally manufactured equivalent [Vilaro T, Abed S, Knapp W. *Direct manufacturing of technical parts using selective laser melting: example of automotive application. In: Proceedings of 12th European Forum on Rapid Prototyping. 2008*]. Not only finished engine components like engine exhaust valves and pistons [11], but also Ti6Al4V open cellular foams that can be applied to automotive systems thanks to the high mechanical properties and lightness [12]. An intake system for racing engines to minimise pressure losses, has also been developed with AM [13].

1.4 Comparison with traditional production

Additive manufacturing has several advantages to traditional production methods (that we can describe with the retronym “subtractive manufacturing”). The most evident is that AM avoids material wasting because it only puts material where is needed, for the piece itself or for the supports, whereas in traditional subtractive manufacturing a lot of material is usually wasted during the manufacturing process. Another bonus of the AM is the high level of geometric freedom, in fact one of the synonyms of Additive Manufacturing is Free Form Fabrication (FFF). This is an advantage because it allows to produce a complex object that used to be assembled from many components in fewer or even just one part, or it permits

to optimise geometry with the topological optimisation process that is capable to put material only where it is needed removing it from other unsolicited zones. This process usually brings to very complex geometries, even impossible to produce with conventional manufacturing methods. Another advantage of the geometrical freedom is the chance to customise the production with a much lower set up cost than conventional manufacturing, making possible the concept of mass-customisation and affordable small batches for high level production (luxury, racing, aerospace, on demand production, etc.). The last interesting advantage to point out is the one that gave the “old” Rapid Prototyping (RP) its name. In fact, these AM techniques still serve as a support to the development process of many parts and products mainly because of the rapidity that some of them have in the creation of a 3D object from a CAD model, because it is always better to evaluate something in 3D rather than on a screen.

1.4.1 AM production flow

The scheme reported in Figure 3 shows all the different steps of a general AM production flow.

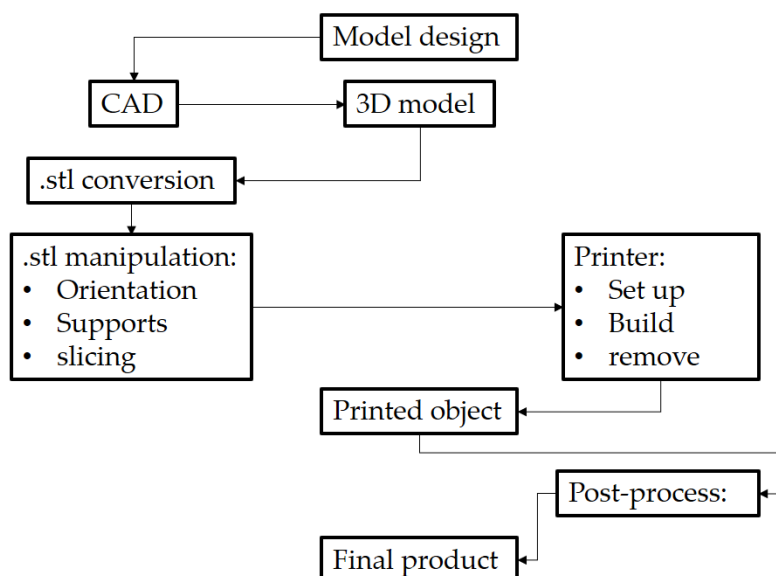


Figure 3: a scheme of the entire additive manufacturing process, from the conceptual design to the final product. On the left the software processes, on the right the hardware processes and in the centre the product.

Once you have designed your model using a CAD software, you must convert it into a STL file, one of the main file format that AM machines software can process. This file can be manipulated and prepared for the print in dedicated software that are able to orient the model, generate supports if needed and finally complete the slicing operation that transforms a 3D object into a stack of 2D layers to be printed one on the top of the other. The resulting file with the instruction for the printer is then transferred to the AM machine, that must be set up for a new print. Then the real printing process takes place. After that, the piece must be removed from the printer and the printed object can then undergo some post-processing steps like washing, thermal or UV post-curing, surface finishing, joining with other parts until it reaches its final destination.

1.5 AM: one family, many different technologies.

AM is a great family of technologies capable of processing many different materials. As illustrated in Table 1: pure metals like silver, gold and titanium as well as metal alloys like Aluminium, Co-Cr and Nickel alloys along with the versatile Ti6Al4V and stainless steel; thermoplastic polymers like polycarbonate (PC), polylactic acid (PLA), Polyetherimide (PEI), polyamide (Nylon, PA), Polyester, Polyether ether ketone (PEEK), polypropylene (PP), polystyrene (PS), ABS (Acrylonitrile Butadiene Styrene), thermoplastic polyurethane (TPU), and a certain number of these polymers' blends. Of course, also thermosets like acrylic and epoxydic resins. But additive manufacturing processes are not limited to the metals and polymers only. Alumina, lead zirconate titanate and silicon oxycarbide, as well as other ceramics, can be processed. Glass additive manufacturing is reported as well as concrete material extrusion. AM processable materials are ample and diverse; moreover, almost all these materials can be filled to obtain some kind of composite material.

However, this thesis will be focused on the AM technologies capable to process polymeric materials and mainly on the vat photopolymerisation techniques.

Table 1: materials processed by AM and their process family [14].

Material	Material Extrusion	Vat Photopolymerisation	Material Jetting	Powder Bed Fusion
ABS	[15,16]			
PC	[17,18]			
PLA	[19]			
PEI	[20,21]			
Acrylates		[22,23]	[24,25]	
Epoxies		[26]		
PA 11/12	[27,28]			[29,30]
PS				[30,31]
PP	[32,33]			[34]
Polyester		[35,36]		
PEEK	[37,38]			[29,39]
TPU	[40]			[29,41]
Chocolate	[42]			
Al alloys				[43–46]
Co-Cr alloys				[47,48]
Gold				[49–51]
Ni alloys				[52,53]
Platinum				[51]
Stainless Steel				[54,55]
Titanium				[56]
Ti6Al4V				[57,58]
Alumina				[59–61]
Lead zirconate titanate	[62]			
Ceramics	[63,64]	[65–67]		
Glass	[68]			[69]
Concrete	[70,71]			
Silicon oxycarbide		[72]		

It is possible to group the printing technologies developed for polymeric materials, starting from the different forms of material they are able to process (Figure 4). Some technologies start from powder materials and create an object by depositing a binder on the layers of powder (binder jetting) or by selectively sintering or melting them (powder bed fusion). Some other technologies use solid materials (usually pellets or wires) that are melted to be selectively deposited to form each layer to build the object (material extrusion). Finally,

other technologies start from a liquid material either to locally deposit and cure it (material jetting) or to selectively cure it from a liquid vat (vat photopolymerization, or VP). Each technology can reach different levels of accuracy and complexity for the object constructed [73].

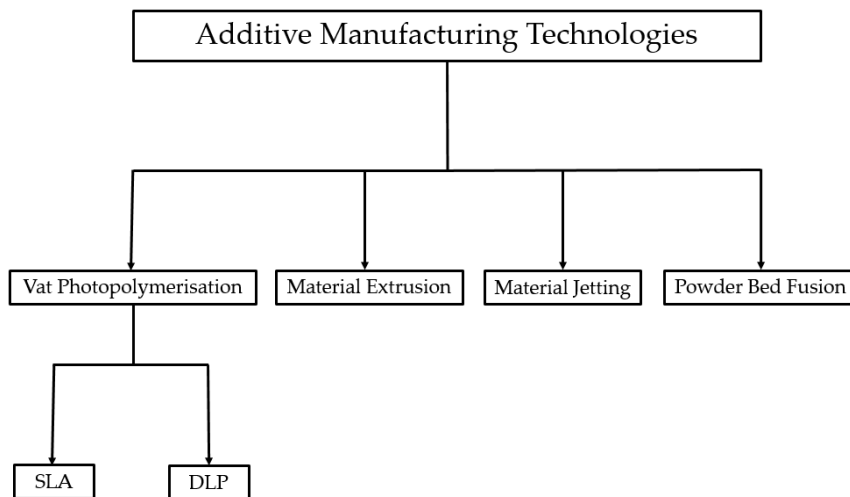


Figure 4: AM technological families, with more detail for the VP [1].

1.5.1 Powder bed fusion

Among AM techniques, the family of processes that starts from powder layers to create the object collectively goes under the Powder Bed systems. In the field of polymers, Selective Laser Sintering (SLS) was the first commercialised powder bed process. In every SLS system there is a mechanism that supply new smooth powder layer of the desired height (typically 0.1 mm), at least one thermal energy source able to sinterise powder particles between them and all the control apparatus to direct and regulate that energy source (Figure 5).

Once the powder layer has been spread across the surface of the build chamber, usually with a levelling roller or blade, the laser scans through the surface of the layer fusing the powder particles together to form the first layer of the object. Afterwards, the build platform goes down of a single layer height and a new powder layer is spread and levelled

by the roller. The whole operation takes place into an inert gas filled build chamber to prevent degradation of the powders. The chamber and the powders are kept at a high temperature, above glass transition temperature, to avoid using too high power lasers and to prevent warping and curling due to high differences of temperature. The loose powder that remains surrounding the solidified layer of the object, can be used to support the successive layers making this process self-supporting, within certain limits [73].

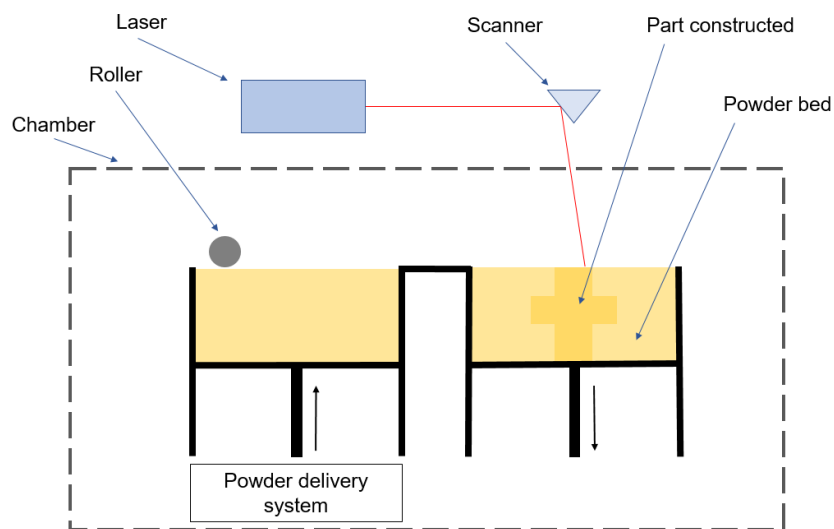


Figure 5: Powder Bed Fusion process scheme

1.5.2 Material extrusion

One of the simplest AM technique is the Material Extrusion (ME) (Figure 6). It all starts with a solid material, usually wires or pellets, softened by a heater element before the nozzle. Pressure is then applied to the softened material to let it flow through the nozzle in a constant smooth way, in accordance with the movements of the nozzle scanning the layer. The material should harden right after the extrusion and must bond to the previous layer to form a coherent solid structure. There can be support structures, even in a secondary material extruded by a different nozzle, to permit the construction of very geometrically complex structures [73].

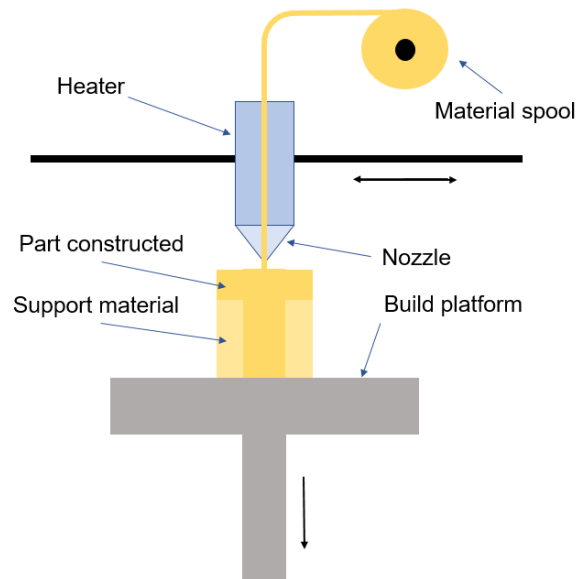


Figure 6 Material Extrusion process scheme

1.5.3 Material Jetting

Another relevant AM technology is Material Jetting (MJ) (Figure 7), the most similar to 2D printing. In fact, MJ printers have printheads that dispense droplets of photocurable acrylic thermosets that are solidified by the passage of UV lamps, thus forming each layer. The liquid material must be preheated before printing to achieve the right viscosity, then the jetting head scans the build platform and deposit the liquid material in a line-wise fashion (an exception from the other AM processes). The curing is provided by the UV lamps attached to the same jetting head. After each layer is completed the platform is lowered by a layer height and the machine is ready to deposit and cure a second layer.

The fact that many printheads are attached to the jetting head allows usage of multiple materials (colours and dissolvable support materials allowed). The MJ liquid based printing system makes the usage of support material always necessary [73].

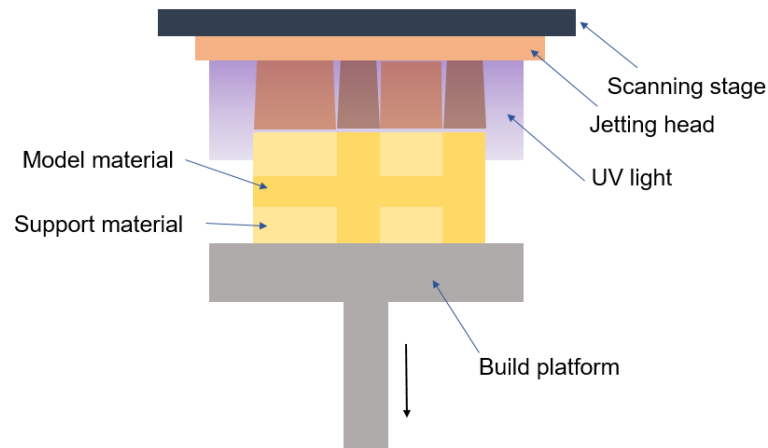


Figure 7: Material Jetting process scheme

1.6 Vat Photopolymerisation techniques

Vat photopolymerisation (VP), as defined by the ASTM F2792 – 12a Standard Terminology for Additive Manufacturing Technologies [3], is an additive manufacturing process in which liquid photopolymer in a vat is selectively cured by light-activated polymerisation.

This family of AM processes can provide the highest standards in terms of part complexity and shape accuracy. There are two main VP typologies: vector scanning based processes, like Stereolithography (SLA), and mask projection based processes, like digital light processing (DLP), but they both start from a liquid to solidify the desired object by the action of light, which activates the polymerisation reaction.

1.6.1 Stereolithography - SLA

Stereolithography (SLA) is a VP process used to produce parts from photopolymer materials in a liquid state using one or more focused lasers to scan the surface of each layer and selectively cure to a predetermined thickness and harden the material into shape, providing the energy to initiate polymerisation [1,3].

There are two different configurations for an SLA machine: top-down or normal SLA (Figure 8) and bottom-up or inverted SLA (Figure 9). The top-down process uses the build platform as base for the construction of the object, the platform should be immersed layer after layer into the liquid photopolymer to allow the prosecution of the process. Differently, in the bottom-up process the objects are attached upside-down to the build platform that rises each time a new layer is completed.

From the comparison between those two different approaches, it is clear that inverted SLA has many advantages over the normal SLA [74]: thinner layers make possible to reach higher vertical resolution and surface quality, avoiding or limiting staircase effects, moreover the height of the object is vat independent, not being correlated to the depth of the resin container. Another important advantage is the possibility to work and print with less material, avoiding waste and making this technology more suitable for research activity. A final bonus is that recoating operation is eased by the part not being inside the vat [1].

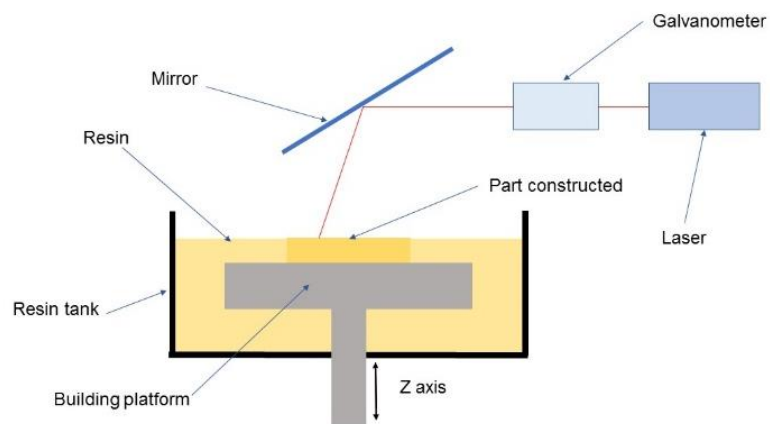


Figure 8: SLA process scheme

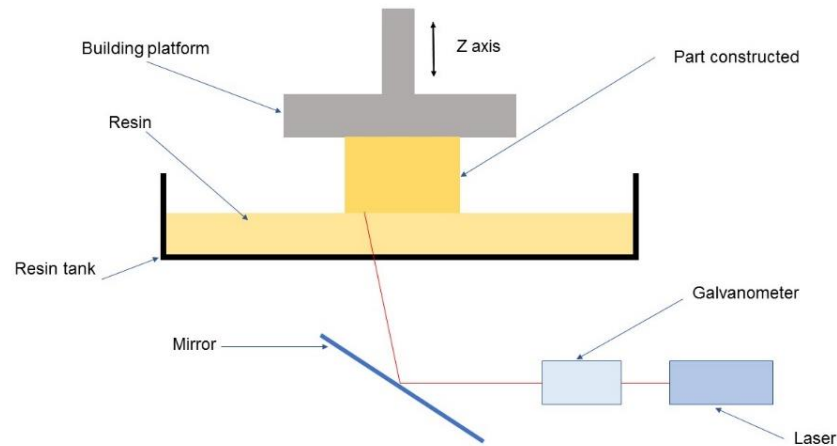


Figure 9 inverted SLA process scheme

1.6.2 Digital Light Processing - DLP

The DLP (Figure 10) differentiates from SLA because, instead of a laser scanning, it has a digital micromirror device (DMD) projecting a photomask for each layer. A DMD is a micro-opto-electromechanical system, a chip whose surface is made of many hundred thousand microscopic mirrors. Those mirrors are disposed in a rectangular array to form the pixels of the image to be displayed. The mirrors can rotate individually from ON to OFF state, in the ON state the light from the source is directed on the build platform to produce the image of the object to cure, while the light that hits the pixels in the OFF state is deflected elsewhere.

The photomasks allow to cure whole layers in less time than in vector scanning systems, dramatically reducing printing time. But the higher speed of the process is balanced from the intrinsic lesser accuracy of DLP, in fact in SLA laser spot size is smaller than the minimum pixel size of the DMD, providing smaller minimum feature size.

Another significant difference between the two main VP technologies is that after SLA a post-treatment is generally needed because the laser scanning pattern focuses mostly on the outline of each layer to reduce the building time. This strategy can leave some uncured resin on the inside of the object that must be post-cured either using an ultraviolet (UV) lamp or an oven for thermal curing. The intrinsic advantage of DLP is that this technology allows

State of the art

curing the whole surface of the layer at once, with no difference between the outline and the inner area, making post-curing less necessary [1].

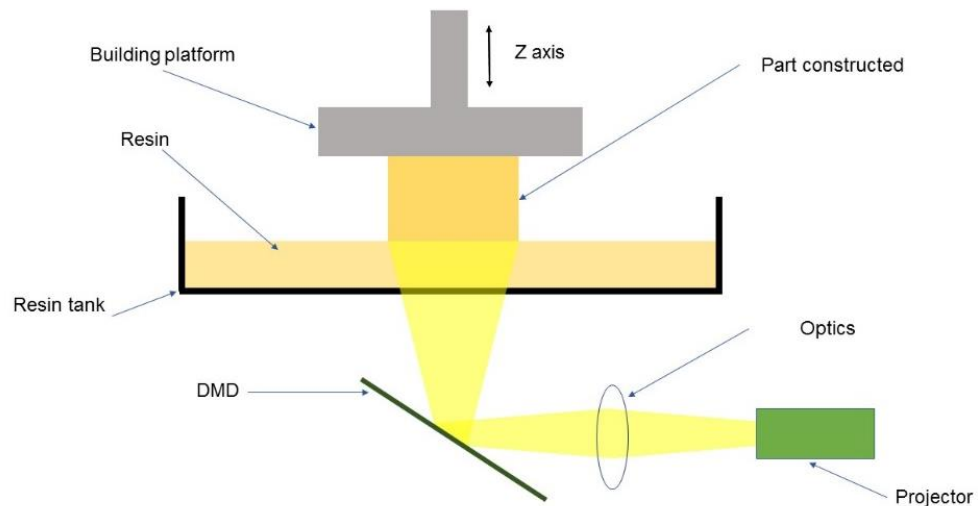


Figure 10 DLP process scheme

1.6.2.1 Micro-stereo-thermo-lithographic system - STLG

The micro-stereo-thermo-lithographic system (STLG) of the CDRSP (Polytechnic Institute of Leiria, Marinha Grande, Portugal) (Figure 11), is a homemade modified DLP prototype system [75]. It is based on a double concurrent radiation system. The large spectrum (UV, Vis, IR) radiation resulting from a mercury lamp is split in two and then selected by two filters into UV and IR beams. The UV-part is directed to the DMD and finally to the build platform, while the IR-part is used to rise the build platform temperature and ease the polymerisation process along with the other possible reactions occurring. It is a sort of application of the Two-Photon Polymerisation (2PP) concept to the DLP technology but using two different radiations.

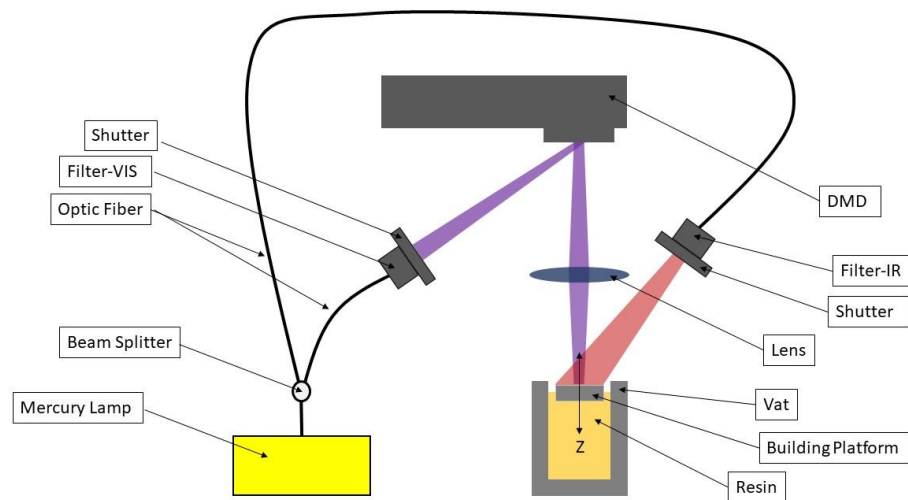


Figure 11: STL process scheme

1.6.3 Two-photon polymerisation (2PP)

Two-Photon Polymerisation (2PP) Figure 12 is a relatively new and very specific technology for the fabrication of *quasi* arbitrary 3D microstructures. It is an inherently 3D process, not limited to the layer-wise process of general VP [76]. It works focusing femtosecond laser pulses into the photopolymer, the reaction remains confined to the small focal volume because the two-photon absorption process is strongly limited by the light intensity. When the focal volume has scanned the entire object the process is completed by the solvent washing of the unreacted resin. Since 2PP, being a threshold process, is not limited by the optical diffraction, the proper adjustment of the photon dose makes possible to reach the 100 nm order feature size [77,78]. In fact, 2PP is the AM process with the best resolution and accuracy [23,79,80]. This exceptional precision has the main drawback in the low writing speed, 2PP is much more slow than conventional VP processes, if SLA has a 200-500 mm/s speed, 2PP is roughly one or two orders of magnitude slower (circa 0.5–2 mm/s)[23]. The other limitation is, for the moment, that the maximum height of the part cannot exceed 1 mm, a very strong limitation for the fabrication of many products.

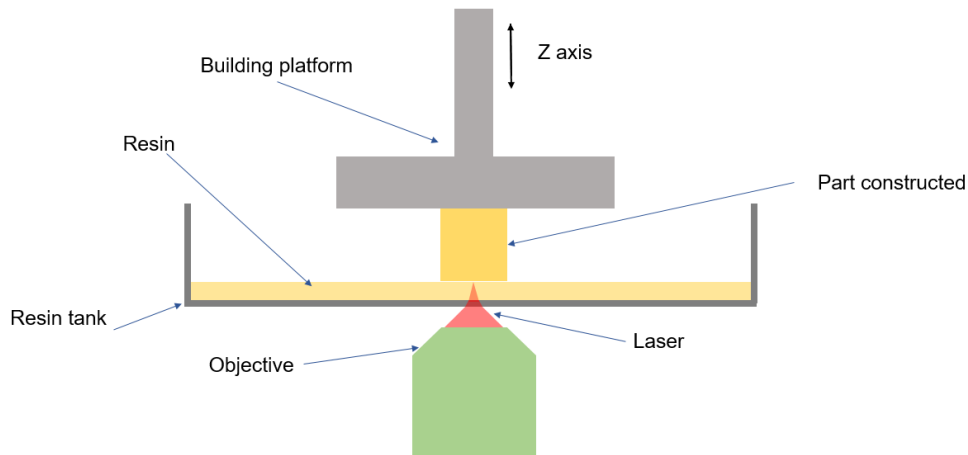


Figure 12: 2PP process scheme

1.6.4 Other techniques

The following technologies are interesting even if not very diffused, they are modifications or customisation of VP technologies for specific targets. They are presented here to show that VP technologies can serve a large amount of purposes.

1.6.4.1 Solution Mask Liquid Lithography - SMaLL

To avoid the staircase effect on the sidewalls of 3D printed object, some have developed a modified DLP technique capable of synchronising the build platform movement with the appropriate change in the projected masks so that the process is capable to obtain smooth sidewalls. This technique has several names: dynamic optical projection stereolithography (DOPsL) [81], layerless fabrication with Continuous Liquid Interface Production [82,83], Solution Mask Liquid Lithography (SMaLL) [84].

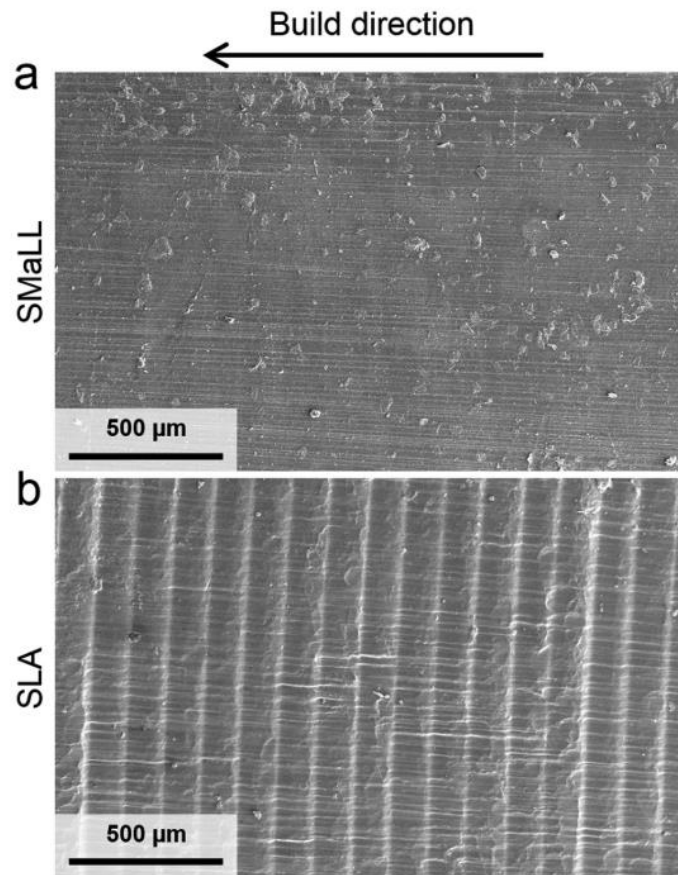


Figure 13: SEM micrographs of untreated surfaces of cones printed by SMaLL (a) and SLA (b) [84]

1.6.4.2 3D magnetic printing

A magnetic DLP system to allow the selective orientation of reinforcement fibres inside the polymer matrix have been developed to build biomimetic structures recalling natural composites for more performative applications [85]. The process is defined as an AM approach that combines real-time colloidal assembly with existing additive manufacturing technologies to create highly programmable discontinuous fibre composites. The fillers are not magnetic, in fact alumina, silica and calcium phosphate are employed, but they all are coated with iron oxide nanoparticles through magnetic-labelling techniques [86,87]. Once the applied external magnetic field has given the nanoparticles the right orientation, the polymerisation occurs freezing the disposition of the filler inside the matrix, then the field is removed and a second layer is set up for the prosecution of the print. The magnetic field can

1.6.5 Materials for VP

1.6.5.1 *Photopolymer families and polymerisation types.*

Every starting material for VP processes needs to contain, regardless of the specific technique or of the possible filler, some mandatory elements:

- The reactive, UV-curable monomer/oligomer or blends of different ones, capable of cross-linking to obtain the desired solid object;
- The initiator (or a blend of different ones) to be photodegraded under the action of the light source. The degradation of the photoinitiator forms radicals, cations, or carbene-like species, that are responsible of the activation of the polymerisation process [107].

Monomers and initiators are the basic materials for VP, but there are also some additional materials that can be included in the formulations to improve printability or offer important properties:

- A dye can be added to the basic formulation for many purposes. It can, with its bright colour, prevent undesired light leakages from the illumination area, helping maintaining control over layer thickness [89,101]. For example, the dye called Reactive Orange has a well-known and established photocatalytic degradation [103,108]. Similarly, Orange Orasol G dye has been added to photocurable formulations in small quantities to set the right light penetration depth [102].

Dyes are used also to tune the refractive index of the resin to match the one of the filler [5]. Dyes can also serve as overcuring inhibitors, preventing the typical loss of

fabrication resolution occurring in the case of an over reacting resin formulation or excessive diffraction of the light inside the vat [90];

- Some reactive diluents, basically low viscosity monomers, can also be added to the main resin formulation to adjust viscosity, a key technological parameter in every liquid AM process;
- Finally, it must be noted that many different fillers can be added to the matrix to adjust its properties or add new ones.

There are two main families of base materials used in VP processes. Each family relies on a different polymerisation process: radical polymerisation of acrylic or methacrylic-based resins (or other resins modified with acrylate ends) and cationic polymerisation of epoxy or vinyl ether-based resins. As already said, the base material of the matrix is very important because it sets the starting properties that can be modified by the addition of fillers, and it regulates the curing mechanism.

The radical polymerisation based on acrylates and methacrylates is the most commonly used [81,85,89–93,97,102,103,105], one of the overall most used monomers is PEGDA being some kind of preferred base material for VP processes [89,91,103,105].

The less common epoxy-based cationic polymerisation is rarely applied alone [98][94], it is more common to see mixture of acrylates and epoxies [100,104,109] that try to combine the advantages of the two families attempting to limit disadvantages. The difference between the two resins has also been studied in separate experiment by the same researcher in the same paper [96].

1.6.5.1.1 Free-radical photopolymerisation

As already said, acrylic and methacrylic-based resins are the most commonly used and they are based on free-radical photopolymerisation. This mechanism is based on the

production of free radicals following the homolysis of weak bonds due to the interaction with photons. Naturally, the behaviour of the system is heavily affected by the properties of the resin itself, like number of functional ends and molecular weight or chain length. Lower functionalities mean lower viscosity, while more functional groups have the power to decrease flexibility and increase reactivity and, of course, viscosity. Concerning the molecular weight, higher values bring flexibility reducing reactivity, on the contrary lower molecular weights increase reactivity and stiffness.

An example of what can take place in the very first step of radical polymerisation is reported in Figure 14. The photoinitiator, in this case Irgacure 819, is photodegraded by the action of the UV beam and the resulting reacting radicals initiate the polymerisation reaction. The reaction continues as long as there are monomers that can reach the reactive spots on the 3D network that the crosslinking is forming.

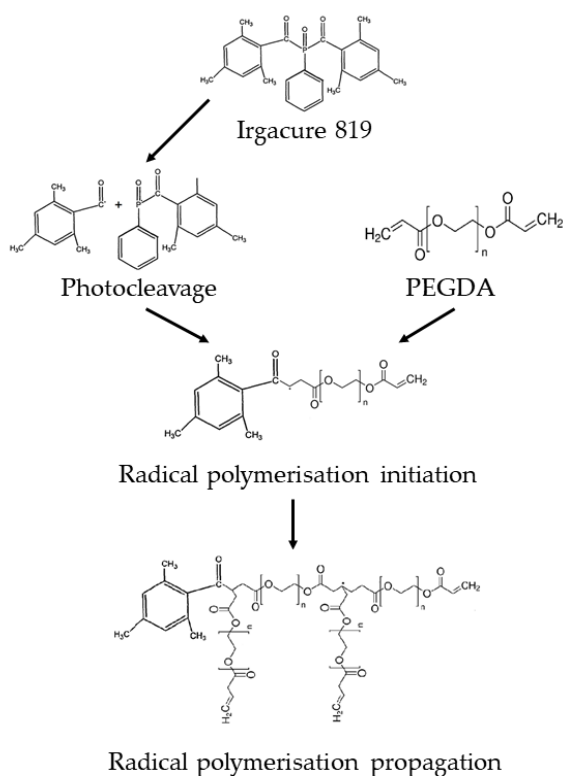


Figure 14: radical polymerisation initiation and propagation scheme of PEGDA activated by the photocleavage of the Irgacure 819 photoinitiator

1.6.5.1.2 Cationic photopolymerisation

The other main polymerisation process is the cationic chain growth typical of the epoxy and vinyl ethers-based resins. These systems are usually less reactive (the reaction takes longer) than free radical ones, but they are less prone to shrinkage and exhibit better mechanical properties [5]. Epoxy systems are more used than vinyl ether ones, but still less studied than acrylic and methacrylic resins. However, it is possible (and not uncommon) to use mixed systems of radical and cationic polymers to study and tune a dual-curing mechanism [104] or to develop a formulation that could combine the advantages of both systems (and possibly limiting the disadvantages)[100,109].

1.6.5.2 *Composite and functional materials.*

Fillers of very different nature can usually be added to a resin formulation to improve existing properties (e.g. mechanical, optical, etc.) or give new ones (e.g. electrical, magnetic, etc.), or even to introduce desired and controlled anisotropy that can serve to properly response to stresses tailoring the properties in suitable directions more than in others.

1.6.5.2.1 Functional materials

Fillers are often used to improve or give structural or functional properties inside VP formulations. Providing or increasing a certain property, results in the functionalisation of the polymer composite. This composite can be used in wider applications than the pristine matrix. Enhancements of electrical [89,91,92,103], thermal [98,109], magnetic [110], mechanical [85,93,94,98,99], electromagnetic[97], antibacterial [95] properties are reported.

In some cases, the filler content is so high that the matrix material acts more like a binder while the filler material turns out to be the principal component. Filler (ceramic or

metallic) is processed with a necessary binder that is then burned to make the real object (after sintering) [5,96].

Another common filler family is represented by fibres. Short or long fibres are added to the formulations to introduce anisotropy or to adjust and improve mechanical properties of the matrix.

An important side effect of the addition of fillers is the mitigation of shrinkage subsequent to the reduction in the mobility of the polymeric chains. This is an advantage because it enhances accuracy of the printed parts.

Naturally, the addition of fillers to the formulations also introduces problems and specific limitations that must be considered when developing a composite material for VP processes.

- **Stability:** the resin containing the fillers must be stable during the entire duration of the process which depends on many factors (e.g., layer thickness and part height), but is usually at least 1 h in the case of SLA (in DLP this issue is less problematic because of the speed of the process, but it is still present). This means the particles suspended in the resin must not undergo sedimentation or agglomeration phenomena and must not be involved in collateral reactions (e.g., oxidation must be controlled)[5].
- **Homogeneity:** the filler must be well dispersed into the resin, in fact the final properties would be strongly compromised by a poor dispersion (e.g. a good dispersion is crucial to reach percolation threshold phenomenon capable of assuring electrical conductivity in a polymer composite)[96].
- **Scattering:** filler particles must not induce excessive scattering phenomena in the light path and the transparency of the blend must be granted avoiding over-absorption. To face this problem and try to solve it, it is possible to tune the refractive index of resin and filler to be similar, thus improving processability [5].

State of the art

The Lambert–Beer law of absorption is a powerful instrument that can help in predicting the reactivity of the system, while trying to face the last limitation. Cure depth (C_d) is a crucial parameter that represents the maximum depth curable by the light power in a single layer. It is function of the penetration depth (D_p) as follows [5]:

$$C_d = D_p \ln\left(\frac{E}{E_c}\right)$$

where:

D_p is the penetration depth of the resin, i.e. the depth at which the irradiance becomes 1/e times that at the surface;

E is the laser exposure on the resin, the energy given by the laser to the resin during the scanning of the layer;

E_c is the critical exposure of the resin at laser wavelength and this means that, below this energy, polymerisation cannot be activated.

The process is clearly promoted by low E_c and high D_p while higher cure depth allows higher layer thicknesses and lower building times.

In presence of a filler, the penetration depth of the resins is given by the following expression [81]:

$$D_p = \frac{2}{3} \left(\frac{d}{\varphi Q}\right) \left(\frac{n_0}{\Delta n}\right)^2$$

where:

d is the mean particle size of the filler;

φ is the fraction volume of filler;

n_0 is the refractive index of the monomer solution;

State of the art

Δn is the refractive index difference between monomer and filler;

Q is the scattering efficiency term, which is the ratio of the energy scattered by the particle to the total energy in the incident beam intercepted by the geometric cross section of the particle.

Penetration depth is therefore function of the filler dimensions and fraction volume and of the refractive index difference between filler and the matrix resin (even if the latter can be tuned through means of a dye, as already reported).

1.6.5.2.1 Nanocomposites

As already stated, the real advantage of composite materials is the possibility to combine properties from different materials (e.g. conductivity of metal nanowires and lightness of a polymeric matrix). The addition of nanotechnology brings to the synergic composite advantages the special properties of nanometric fillers. These intrinsic characteristics of the materials, are enhanced by the freedom and advantages coming from AM in general and VP in particular [111].

A composite material becomes a nanocomposite if at least one dimension of the filler is below 100 nm [112]. The key factor in the significant improvement in mechanical and physical properties from bulk material to the corresponding nanometric one [112], is due to the higher surface-to-volume ratios and, often, exceptionally high aspect ratios of nanofillers. These two characteristics favour greatly the interaction between fillers and the matrix acting strongly on the composite properties, even at very low loadings. However, there are problems that can occur when employing nanofillers that are always complex and sometimes dangerous to handle. Moreover, the dispersion and homogenisation of nanofillers is really critical and must be conducted properly to avoid clustering and consequent decrease of properties [88,113].

Some examples of the research carried out on polymer nanocomposite materials for different applications are reported hereafter. Often authors are trying to give desired

functionalisation to printable materials starting from commercial resins and fillers. A lot of work has been done to increase the mechanical properties of nanocomposites and to understand the dependence on filler nature and content. 4–6,15–19 Polymer nanocomposites tend to become more brittle with increasing filler content, that is why one of the most challenging goal to reach is to retain ductility while increasing mechanical properties [93,99]. The addition of graphene oxide (GO) in [99] determined a change in the crystallinity of the polymer and this is identified as the main reason for the increase of ductility together with the enhancement of tensile strength. In fact, as observed in [114], crystallinity (as well as other properties related to the polymer chain) can vary significantly and continuously from the interface with the filler into core material of the matrix. A lack of embrittlement that follows the increase of mechanical properties of the nanocomposite is also found in [93], where K_{Ic} seems to not be correlated to the filler concentration.

Other researchers have been more interested in giving and improving electrical and thermal properties of materials [98,109]. In this way, it is possible to print 3D conductive complex structures for application as connectors of electrical circuits [92], or structures for dissipation and packaging in electronic devices [103].

Another important field of application is the biomedical [102], where VP is used to make complex biodegradable structures suitable for use as implants or scaffolds. Other applications of polymeric nanocomposites processed via VP are radar absorbing materials (RAM) [97], piezoelectric materials [105], or even the fabrication of a flow sensor device entirely made using VP [90]. Not all the research has been directed toward improving certain properties of the material; some [81,104] aims to achieve better understanding of the technological aspects, like process parameters [81] and filler–matrix interaction effects on the process (e.g., curing kinetics [104], rheology) or the study of dual-curing mechanisms [104] with a mixture of acrylic and epoxy resins. In [96] there is reported an attempt to replace a traditional expensive technology (hot pressing) with AM for the fabrication of amorphous thermoelectric materials.

Focusing on the fillers, the most used ones are the carbon-based, like CNTs [91,94,97,98], cellulose nanocrystals (CNCs) [100], or GO [99], as their organic nature promotes filler–matrix interaction. Metal oxides, such as nano-TiO₂ [109], Al₂O₃ [85], BST

[96], boehmite [104], hydroxyapatite [102], barium titanate (BaTiO₃) [105], calcium phosphate [85], and Fe₃O₄[90] are also often used. The use of metal oxides is a low-cost method to increase mechanical and thermal properties of the composite. The most used oxide is silica [85,93], with organic surface modification to improve adhesion and bonding between NPs and the matrix [81].

Chemical modification is also used for nanoclays like montmorillonite and attapulgite [81,104]. Pure metals are mainly represented by silver. There are many ways to obtain Ag NPs, and the in situ formation is often used. A silver precursor salt (often silver nitrate [89,103]) is generally added to a monomer to obtain NPs after the process of VP by UV irradiation or by thermal treatment. Photoreduction of Ag NPs from AgNO₃ may be activated by a UV post-treatment after fabrication, because the DLP works with visible light that cannot activate the process[103].

The advantages of generating NPs in situ, even if after the fabrication process, consist in avoiding dealing with NPs while printing, thus eluding sedimentation, agglomeration, and scattering effects. Among the disadvantages, there is possible UV degradation and not sufficient penetration of light into the core of the material. A thermal treatment in vacuum can be used also to achieve the same purpose avoiding UV [89]. Generating NPs after the fabrication process has the advantage of avoiding complications of dealing with NP suspension during printing (silver nitrate dissolves in the liquid monomer, eliminating problems connected with the two phases). Ag NPs can also be embedded in the porous matrix just after 3D fabrication [92].

Another important factor in relation to composite properties is filler content. Usually it is enough to add small quantities of nano-filler (below 1%) to significantly affect the behaviour of the resulting material [91,94,97–100,104,109]. However, not all nanofillers are so effective and it might be necessary to consider various contents, as well as the interaction between filler content and properties. Some systems can also have low printability limits and do not allow high proportions of filler. Another consideration is that increasing filler has the effect to increase viscosity, which is one of the limiting factors of VP processes. However, there are numerous works that exceed 10% filler content (up to 25% [90], 30% [93] and even 40% [92]).

Some use 0D fillers whose dimensions are all nanometric [81,90,92,93,102–105,109] while others use 1D and 2D nanometric fillers. Single-layer GO with a diameter that can reach 10 μm (while the width is just 0.9 nm) is attested [99]; others [94,98], use multiwalled CNTs with diameters of a few nanometres but lengths that can vary from 1.5 to 20 μm . Similarly, the CNCs [100] have a diameter of 4–20 nm but a length that can range over from 100 nm to a few micrometres. In [85] NPs coupled to microfibers have been used to control their orientation, but the material obtained is actually a microcomposite (even if the control over anisotropy is due to NPs).

1.6.6 Problems and limitations

There are some limitations to consider and some problems occurring when processing a material through VP techniques. Firstly, viscosity must be kept between 5 mPa/s and 5 Pa/s, higher values could slow too much the flow of the resin *de facto* impeding the recoating operation or increasing excessively printing time. Recoating is an important operation in VP technologies that consists in the flow of a new layer of liquid material to cover the previously cured one, allowing the process to continue [5]. Problems can occur even if the viscosity is too low, because resin can flow uncontrollably and go outside the vat compromising the work place and the printer itself. Naturally, the resin must be curable with a suitable cure depth to allow the reaction of an entire layer [5]. On the other side, over-curing must be avoided. It can happen that uncured or partially cured resin is still present in the printed piece after the process, a curing post-treatment step is needed then. This thermal or UV process is carried out to complete solidification of the object and increase mechanical properties. Even if it is a necessary step, sometime if the post-curing is conducted for too long, degradation can occur and a general decrease of the properties (especially for UV treatments). Damage can occur even from a properly conducted post-curing, mainly because of shrinkage, as already said, the acrylic formulations are more prone to this problem than the epoxydic ones. Shrinkage, with the deriving loss of accuracy, is due to residual radicals trapped inside the 3D structure. The process is more evident for high functionalised acrylates that rapidly react literally trapping some radicals inside the new 3D matrix. The less rapid

polymerisation of the epoxy provides less shrinkage and warping effects [5]. The idea is to take the advantages of both formulations while limiting the disadvantages; this is the starting point for the adoption of mixed formulations of acrylic and epoxydic resins. The use of mixed formulations can also influence other properties (e.g., flexibility), which can be better modified to fit different requirements, acting on relative percentages of the components.

1.6.6.1 *Preparation treatments*

The production of a nanocomposite material is quite complex since it involves the combination of different materials with different properties. To make sure that the printing process can take place correctly, pre-treatments are almost always needed.

As already said, the dispersion of all materials composing the formulation (fillers, initiators, dyes, and other external elements added to the liquid monomer) must be as homogeneous as possible to avoid gradients in properties of the printed object or even the failure of the process. So, stirring is very common and even shear dispersion is often necessary [94,98,100], even if not always high mechanical stresses are applicable to obtain homogeneity because some fillers like CNTs can be damaged with too vigorous actions. Ultrasonic dispersion [85,91,93,94,98,99] is certainly effective, but it has some drawbacks for protracted treatments. The heat generated during the sonication can damage the resin or induce early polymerisation. The problem of excessive heat can be easily avoided by recycling the sonication water when it gets too hot or adding some ice to lower the temperature [99], while the second problem seems not to interfere negatively with the final properties of the nanocomposite [98].

The homogenisation process with its mixing operations, can trap air bubbles inside the resin. This occurrence is to be avoided because it can interfere with the printing process and decrease mechanical properties. Thus, a vacuum treatment is recommended to extract eventual air bubbles [100].

Since nanocomposite materials often compose organic matrixes with inorganic fillers, the coupling between them can give interfacial issues due to weak surface bonding. Thus,

the chemical modification of fillers surfaces with organic groups able to increase the chemical affinity with the matrix and forming stronger linkages, can increase interfacial and mechanical properties and lower surface energy [81,93,104,105,109,112]. Examples of this practise can be found in [81], where the chemical modification adds acrylate surface groups to form direct covalent linkages with the polymer matrix, while in [105] reactive alkene groups are introduced onto surface; in [93] methacrylate groups for covalent bonding are provided to improve formulation stability. The organic modification of montmorillonite in [104] serves to change surfaces from hydrophilic into hydrophobic, while in [109] nano-TiO₂ has been treated with a silane coupling agent to enhance interfacial adhesion.

1.6.6.2 *Postprocessing*

Following the fabrication, there can be different post-treatments. Firstly, the object must be removed from the build platform, then eventual supports must be removed to isolate the object itself. If required by the application a surface finishing may be performed to increase surface quality.

Right after removing the object from the build platform, in VP processes, the washing of the object must be performed by immersion or rinsing in an organic solvent like isopropyl alcohol (IPA) [90,92,98,100,102], or acetone [102]. This step serves to extract eventual unreacted resin and clean the outer surfaces. It can have different lengths according to geometrical complexity and material characteristics.

Drying is another important step. After cleaning step, the object must be dried in air or under vacuum [92] or inert gas flow [102]. To assure the complete evacuation of all eventual residues trapped inside the object, for specific applications (e.g. biomedical), this step can be performed for an extended period under stringent conditions.

However, the main post-treatment is UV curing [90,91,93,94,98,100,103], almost always between 30 minutes [94] and 1 hour [98], but reaching exceptionally 2 hours [100]. The general purpose of UV post-curing is to guarantee a full conversion of the unreacted monomer, strengthen the bonding of the final object.

State of the art

There is a peculiar thermal post-treatment reported [96] that is conducted at 350° until total removal of the photoresin template (actually the matrix), the filler remain after as the only component and will be post-processed to obtain an object entirely made of it. Anyway, post-curing is not always needed and some decide not to perform it [105].

2 Materials and methods

This chapter formed the basis upon which the materials and methods section of the original research articles published (or yet to be published) during this doctorate, were constructed. Those articles are titled: “Special resins for stereolithography: in situ generation of silver nanoparticles” [2], “Acrylic resins for stereolithography 3D printing with tuneable thermo-mechanical properties” [to be published], “Development and characterisation of polymer-silver nanocomposites: a comparative study on the technological process between SLA and DLP” [to be published], “Development and characterisation of polymer-graphene nanocomposites for Vat Photopolymerisation additive manufacturing” [to be published]. The following chapter was correlated with additional material from the preliminary tests and unpublished work.

The materials presented and the methods developed, served for the AM production and the functional and structural characterisation of samples of different nature. An unfilled acrylic polymer with tuneable properties given by the control of the mean molecular weight. Several filled materials, with nanometric and micrometric fillers of organic and non-organic nature, with in situ reactive nanoparticles as well as ex situ prepared fillers. Silver nanoparticles have been produced with an *in situ* reaction contextual with the AM process starting from synthesised precursor salts. Advanced nanostructured carbon based materials like thermal expanded graphene oxide (TEGO) have been used and compared to common micrometric graphite. As common in literature, acrylic mixtures have been always used as base matrixes.

2.1 Materials

2.1.1 Base monomers

Since the most used and readily available base monomers for VP additive manufacturing are acrylic based materials, this kind of materials were used also in this

research. Many different monomers and combination of them were tried (Table 2), but in the end just few of them were chosen to be used in the final formulations and printed (Figure 15, Figure 16, Figure 17, Figure 19).

The base monomer formulations must meet specific requirements, such as guarantee the solubilisation of photoinitiators and the stability of the precursor salts without side-reactions or precipitation. Moreover, it is very important to obtain a viscosity inside the technological range accepted by the machine and in general calibrate all the process parameters to allow the print of the object.

2.1.1.1 PEGDA 250 - 700

Poly(ethylene glycol) diacrylate, average Mn 250 (CAS Number 26570-48-9) [115] was purchased from Sigma-Aldrich (Sigma-Aldrich Corporation, USA) and used as received (Figure 15). PEGDA 250 is an oligomer obtained from the polymerisation of ethylene oxide. It is one of the most common and commercially adopted polyethers, its applications in academia and industry are wide and touch many and very different fields [6,91,116].

Poly(ethylene glycol) diacrylate, average Mn 700 (CAS Number 26570-48-9) [117] was purchased from Sigma-Aldrich (Sigma-Aldrich Corporation, USA) and used as received. PEGDA 700 has the same structure of 250 (Figure 15), but the polymeric chain is longer and the whole molecule is heavier and less mobile. In some cases Ebecryl 11 [118], kindly provided by Allnex (Allnex Holding S.à.r.l., Grand Rue, Luxemburg) was used instead of PEGDA 700, as it is a commercial formulation largely based on the PEGDA 700 monomer.

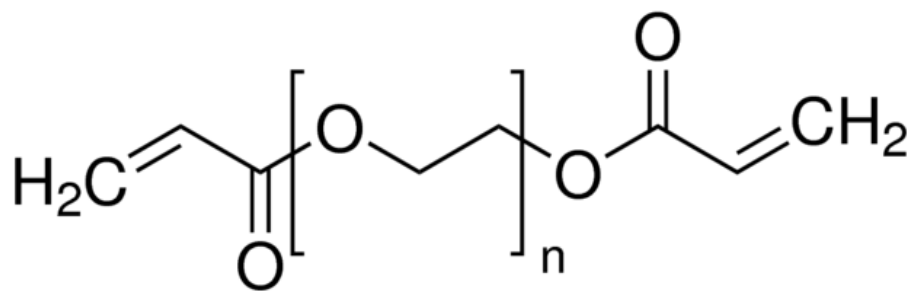


Figure 15: PEGDA molecular structure

2.1.1.2 PETIA

Pentaerythritol triacrylate (PETIA) (CAS Number 3524-68-3) [119] was kindly provided by Allnex (Allnex Holding S.à.r.l., Grand Rue, Luxemburg) and used as received. PETIA is a commercially available mixture of pentaerythritol triacrylate 60-90% w/w (Figure 16) and pentaerythritol tetraacrylate 10-30% w/w (Figure 17). Its viscosity, higher than those of PEGDAs, can be used to tune the thickness level of the formulation.

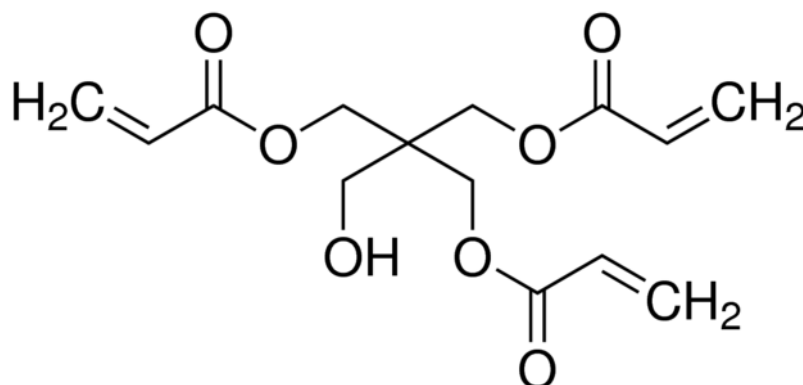


Figure 16: PETIA pentaerythritol triacrylate molecular structure

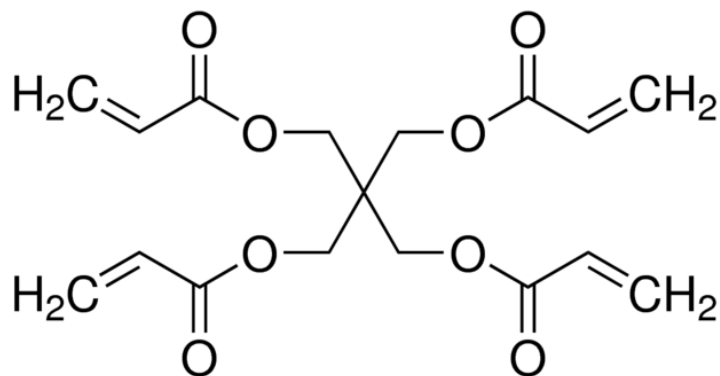


Figure 17: PETIA pentaerythritol tetraacrylate molecular structure

2.1.1.3 Ebecryl 7100

Ebecryl 7100, an amine functional acrylic resin, described as a polymeric amino acrylate in HDDA (10% w/w of hexamethylene diacrylate, CAS number: 13048-33-4, Figure 18) [120] was kindly provided by Allnex (Allnex Holding S.à.r.l., Grand Rue, Luxemburg) and used as received. It can be used to tune the viscosity of the system since it is thicker than PEGDA.

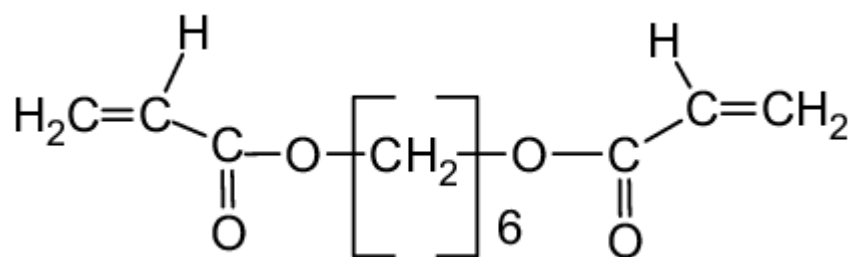


Figure 18: HDDA molecular structure

2.1.1.4 TMPTA

Trimethylolpropane triacrylate (TMPTA) (CAS Number 15625-89-5) [121] was kindly provided by Allnex (Allnex Holding S.à.r.l., Grand Rue, Luxemburg) and used as received.

Materials and methods

It is a very reactive monomer, having three functional ends and very low molecular weight, it is hardly used alone as it is very brittle once solidified.

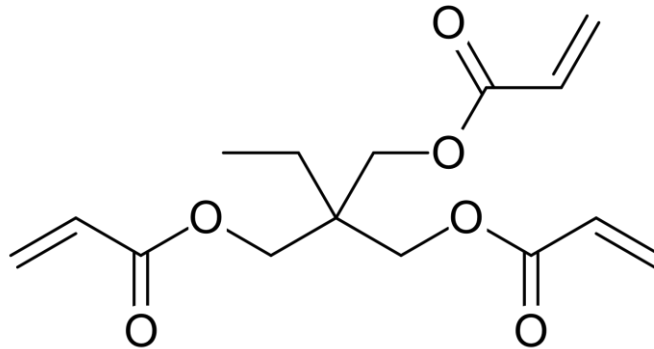


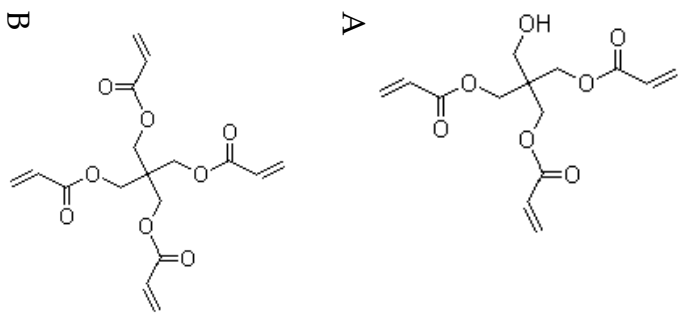
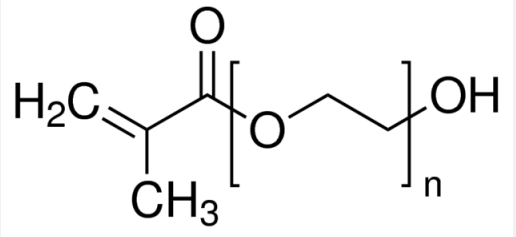
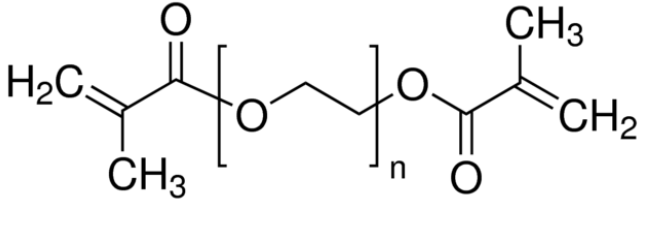
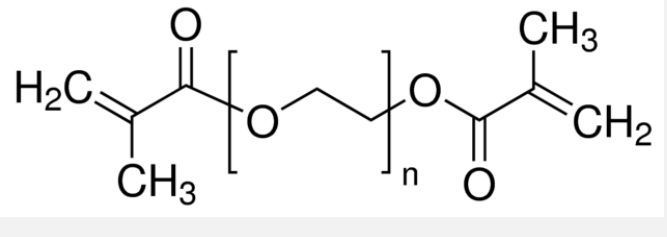
Figure 19: TMPTA molecular structure

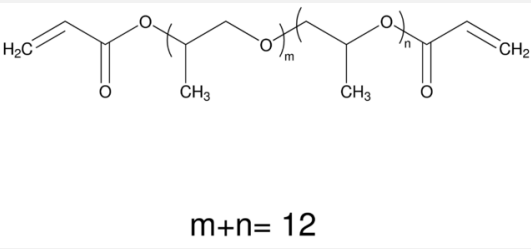
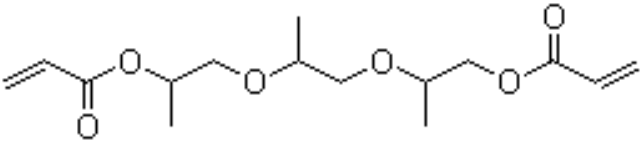
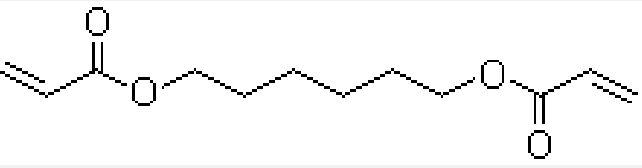
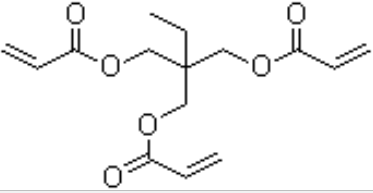
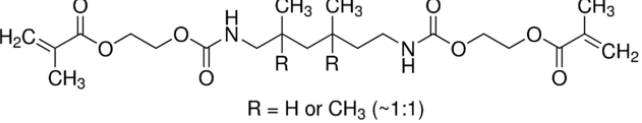
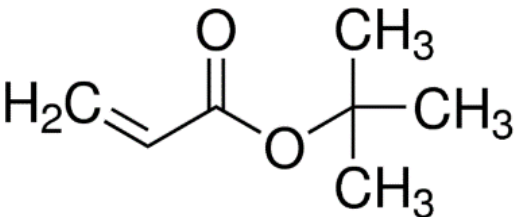
2.1.1.5 Other monomers for initial tests and matrix development

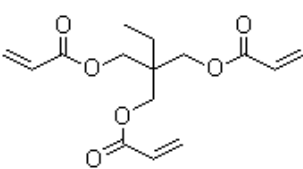
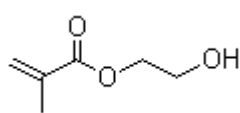
Preliminary tests for the suitability of resin formulations for VP processes and to assure that the resin and the filler fitted well together, were carried out on specific test equipment. These tests were almost 120 and were carried out using the monomers listed in the following Table 2.

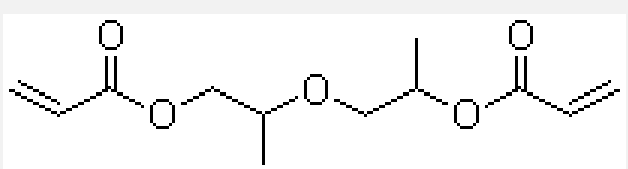
Table 2: table of all the monomers, and their relevant properties, used to test and optimise the matrix formulations [122]

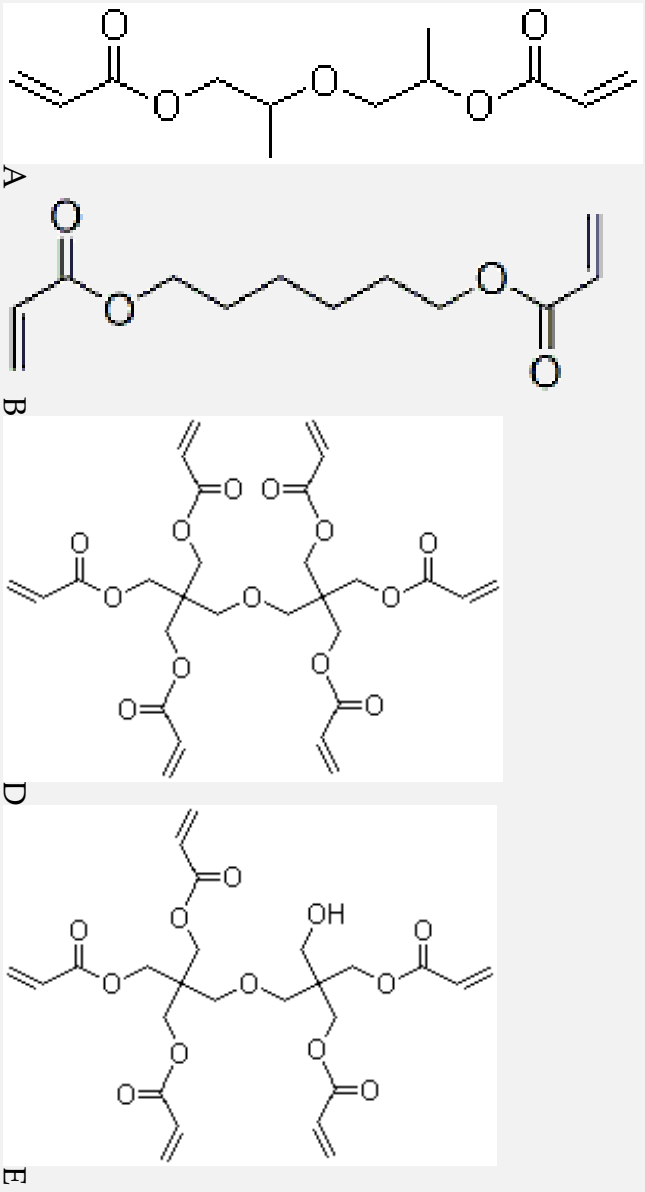
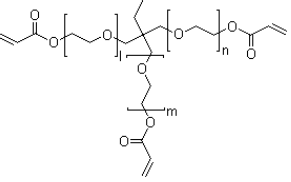
Name	Description	Formula	CAS	MW	Density [g/cm ³]	Functionality
PEGDA 250	Poly(ethylene glycol) diacrylate		26570-48-9	250	1.11	2
PEGDA 700	Poly(ethylene glycol) diacrylate		26570-48-9	700	1.11	2
Ebecryl 11	Poly(ethylene glycol) diacrylate		26570-48-9	700	1.11	2
Ebecryl 7100	Polymeric amino acrylate in HDDA (10%) (A)		13048-33-4	/	1.10	/

Name	Description	Formula
PETIA	Pentaerythritol triacrylate 60-90% w/w (A) + Pentaerythritol tetraacrylate 10-30% w/w (B)	
PEGMA 360	Poly(ethylene glycol) methacrylate	
PEGDMA 550	Poly(ethylene glycol) dimethacrylate	
PEGDMA 750	Poly(ethylene glycol) dimethacrylate	
CAS	A 3524-68-3	25736-86-1
MMW	A 298.32	360
	B 352.34	550
Density [g/cm ³]	1.18	1.105
Functionality	3:4	1
		2
		2

Name	Description	Formula	CAS	MW	Density [g/cm ³]	Functionality
PPGDA 800	Poly(propylene glycol) diacrylate	 $m+n=12$	52496-08-9	800	1.01	2
TPGDA	Tripropylene glycol diacrylate		42978-66-5	300.35	1.03	3
HDDA	1,6-Hexanediol diacrylate		13048-33-4	226	1.03	2
TMPTA	Trimethylol propane triacrylate		15625-89-5	300	1.11	3
DUDMA	Diurethane dimethacrylate, mixture of isomers	 $R = H \text{ or } CH_3 \text{ (~1:1)}$	72869-86-4	470.46	1.11	2
Tert-butylacrylate	Tert-butylacrylate		1663-39-4	128.17	0.879	1

Name	Ebecryl 12	Ebecryl 40	Ebecryl 45	Ebecryl 81	Ebecryl 109
Description	Alkoxylated triacrylate oligomer	Tetrafunctional polyether acrylate	Polyether acrylate oligomer	Amine modified polyester acrylate oligomer	50% w/w TMPTA 50% w/w HEMA (hydroxyethylmethacrylate)
Formula	/	/	/	/	 TMPTA
					 HEMA
CAS	/	/	/	/	TMPTA 15625-89-5
MW	800	571	/	/	300 (A) 170 (B)
Density [g/cm ³]	1.11	1.15	/	1.08	1.08
Functionality	3	4	4	2.5	1:3

Name	Ebecryl 113	Ebecryl 128	Ebecryl 145	Ebecryl 151
Description	Aliphatic monoacrylate	Aliphatic diacrylate	Propoxyylated neopentyl glycol diacrylate	Aliphatic diacrylate 77 – 87% w/w (A) + dipropylene glycol diacrylate (DPGDA) 10-19% w/w (B)
Formula	/	/	$\text{CH}_2=\text{CH}-\overset{\text{O}}{\parallel}{\text{C}}-\text{O}-\overset{\text{CH}_3}{\text{CH}}-\text{CH}_2-\text{O}-\text{CH}_2-\overset{\text{CH}_3}{\underset{\text{CH}_3}{\text{C}}}-\text{CH}_2-\text{O}-\text{CH}_2-\overset{\text{CH}_3}{\text{CH}}-\text{O}-\overset{\text{O}}{\parallel}{\text{C}}-\text{CH}=\text{CH}_2$	
CAS	/	/	84170-74-1	57472-68-1 (B)
MW	/	300	328	242.30 (B)
Density [g/cm ³]	0.97	1.09	1.005	/
Functionality	1	2	2	2

Name	Ebecryl 152	Ebecryl 160
Description	Dipropylene glycol diacrylate (DPGDA) 42-52% w/w (A) + Hexamethylene diacrylate 16-26% w/w (B) + Aliphatic diacrylate 16-26% w/w (C) + Dipentaerythritol hexaacrylate 3-8% w/w (D) + Dipentaerythritol pentaacrylate 3-8% w/w (E)	Ethoxylated trimethylolpropane triacrylate
Formula		
CAS	A 57472-68-1	28961-43-5
MW	A 242.30 B 226.27	450
Density [g/cm³]	/	1.09
Functionality	2: 6: 5	3

Materials and methods

Name	Ebecryl 810	Ebecryl 837	Ebecryl 841	Ebecryl 880	Ebecryl 8210
Description	Polyester acrylate oligomer 30-60%	Polyester acrylate oligomer	Mixture of multifunctional acrylated polyether oligomers	Amine modified acrylated polyether oligomer	Aliphatic urethane acrylated resin
Formula	/	/	/	/	/
CAS	52408-84-1	/	/	/	/
MW	1000	2700	/	/	/
Density [g/cm ³]	/	/	1.1	1.04	1.1
Functionality	4	6	3:4	2.5	3.5

Materials and methods

Name	Ebecryl 8254
Description	Urethane Acrylate oligomer (aliphatic)
Formula	/
CAS	/
MW	1200
Density [g/cm³]	/
Functionality	6

Materials and methods

2.1.2 Fillers

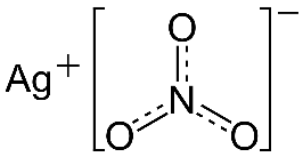
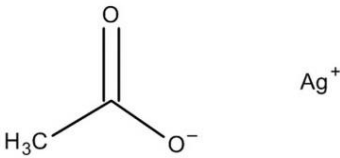
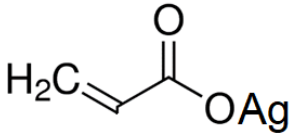
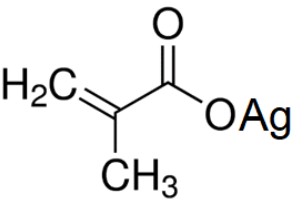
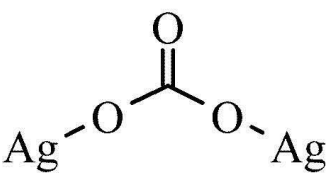
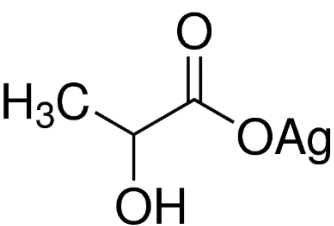
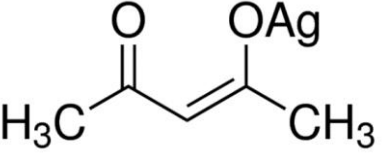
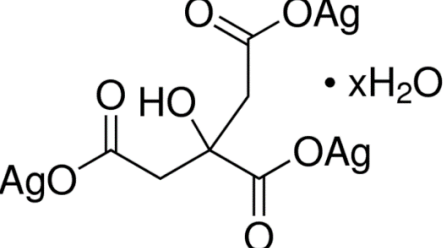
Fillers have great importance in the property balance of a composite material. In the following sections, different kind of fillers used in this work are presented. In particular silver, copper and sodium salts were used as precursors or directly as fillers, such as carbon based fillers like micro graphite and nanostructured TEGO graphene.

2.1.2.1 *Silver salts*

Silver salts were used both as direct fillers or as silver nanoparticles (NPs) precursors. Moreover, silver and sodium salts were used together for the synthesis of silver acrylate and methacrylate. All the silver salts used, even the ones that resulted to be not suitable for a VP application, are listed in Table 3.

Materials and methods

Table 3: table of all the silver salts used as silver nanoparticles precursors or as direct fillers or in the synthesis of other silver salts

Name	Formula	CAS number	MW [g/mol]
Silver nitrate		7761-88-8	169.87
Silver acetate		563-63-3	166.91
Silver acrylate (synthesised)		5651-26-3	178.923
Silver methacrylate (synthesised)		16631-02-0	192.95
Silver carbonate		534-16-7	275.75
Silver lactate		128-00-7	196.94
Silver acetylacetonate		15525-64-1	206.98
Silver citrate hydrate		206986-90-5	512.70 (anhydrous basis)

2.1.2.1.1 Silver nitrate

Silver nitrate (CAS 7761-88-8, Table 3) was purchased from Sigma-Aldrich (Sigma-Aldrich Corporation, USA) and used as received. The nitrate was used as a direct filler to induce, under UV laser radiation, the reduction of the Ag^+ to metallic silver Ag^0 but it was also used together with sodium acrylate to synthesise silver acrylate salt and with sodium methacrylate to synthesise silver methacrylate.

2.1.2.1.2 Silver acrylate and methacrylate

Silver acrylate (CAS 5651-26-3, Table 3) was synthesised starting from silver nitrate (2.1.2.1.1) and sodium acrylate (2.1.2.3.1) following the reaction scheme in Figure 20. Silver methacrylate (CAS 16631-02-0 Table 3) was synthesised starting from silver nitrate (2.1.2.1.1) and sodium methacrylate (2.1.2.3.2) following the reaction scheme in Figure 20.

Silver (meth)acrylate was used directly mixed to the formulations as silver NPs precursor. The major advantage of using silver (meth)acrylate is the absence of unreacted radicals from salt dissociation, as it happens, for instance, with the nitrate group of the silver nitrate. While Ag^+ goes to form nanoparticles, the other (meth)acrylic radical becomes a reactive group inside the acrylic formulation and goes to form part of the polymeric matrix. The absence of free radicals results in a cleaner material without by-products inside, that can more easily be used for those applications where no release is allowed (e.g. biomaterials).

Materials and methods

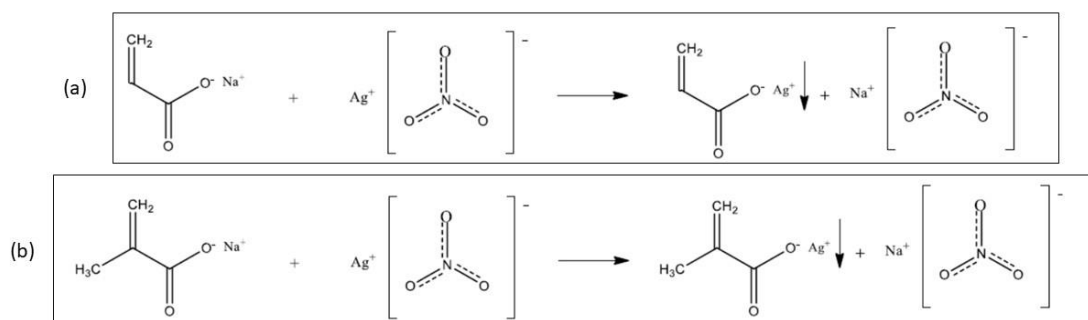


Figure 20: silver acrylate (a) and methacrylate (b) synthesis reaction scheme

Silver acrylate and methacrylate were synthesised starting from silver nitrate and sodium acrylate and methacrylate respectively. The synthesis reaction follows the scheme in Figure 20. Since silver (meth)acrylate is very reactive and unstable, in fact it oxidises easily, the precise quantities for each print were synthesised each time.

The synthesis procedure starts with the preparation of separate solutions for the silver and the sodium salts. The solutions are made in exceeding water (roughly 10 ml of water per gram of salt) to be sure that the concentration is low enough to favour the reaction. The two solution so obtained, must be mixed together until precipitation of a white solid salt (the silver (meth)acrylate). This mixing step is followed and completed by a centrifuge washing. The precipitated salt is separated from the supernatant solution by means of an ultra-centrifuge at 12.000 rpm. The salt is then washed with new water and centrifuged again. This last step is carried out twice to obtain in the end a highly pure (meth)acrylate salt, and evacuate the possible residues of unreacted silver nitrate and sodium (meth)acrylate. The water that is trapped inside the silver (meth)acrylate is extracted with a dynamic vacuum treatment. Alternatively, ethanol can be used instead of water to ease the extraction operation. The dynamic vacuum treatment is repeated after mixing with the liquid monomer to degas and further extract residual water or ethanol.

Silver methacrylate appears to be more stable than silver acrylate and can be preserved in its white unreacted state for several days without turning brown.

Materials and methods

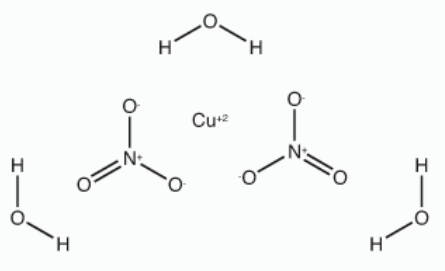
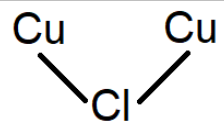
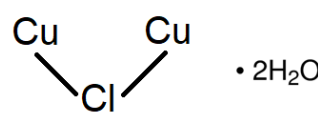
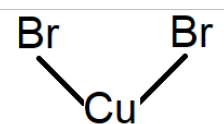
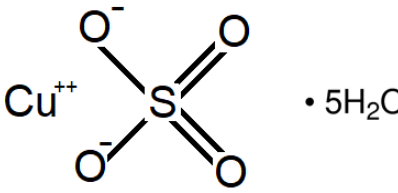
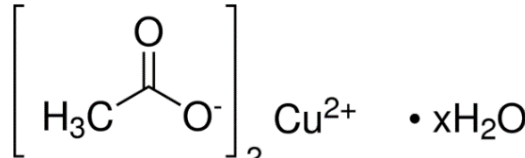
2.1.2.1.3 Silver acetate

Silver acetate (CAS 563-63-3, Table 3) was purchased from Sigma-Aldrich (Sigma-Aldrich Corporation, USA) and used as received. As for the nitrate, the silver acetate was used as a direct filler to induce formation of silver nanoparticles in the polymeric matrix. The intent was to reduce the cation of the salt Ag^+ to metallic silver Ag^0 through the UV laser radiation.

2.1.2.2 Copper salts

Copper salts have been used during the preliminary studies on copper-polymer nanocomposites to try to enhance mechanical and, above all, electrical properties. In the end, no copper-polymer formulation was found to be suitable for VP processes, but the following Table 4 gives a view on the copper salts tested and some of their properties. All the copper salts have been purchased from Sigma-Aldrich (Sigma-Aldrich Corporation, USA) and used as received.

Table 4: table of all the copper salts used and of their main properties

Name	Formula	CAS number	MW [g/mol]
Copper(II) nitrate trihydrate		10031-43-3	241.60
Copper(II) chloride		7447-39-4	134.45
Copper(II) chloride dihydrate		10125-13-0	170.48
Cupric bromide		7789-45-9	223.35
Copper sulphate pentahydrate		7758-99-8	249.69
Copper acetate monohydrate		6046-93-1	199.65

2.1.2.3 Sodium salts

Sodium salts have not been used as direct filler for the formulations, but just as a precursor of the silver (meth)acrylate in the reaction with silver nitrate. The synthesis reaction of the sodium salts with silver nitrate is schematised in Figure 20.

Materials and methods

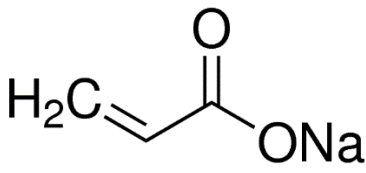
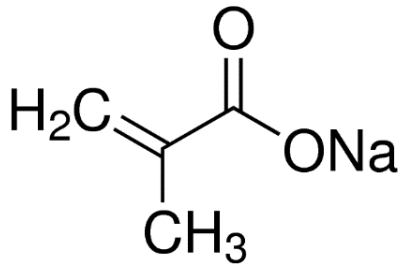
2.1.2.3.1 Sodium acrylate

Sodium acrylate (CAS 7446-81-3, Table 5) was purchased from Sigma-Aldrich (Sigma-Aldrich Corporation, USA) and used as received.

2.1.2.3.2 Sodium methacrylate

Sodium methacrylate (CAS 7446-81-3, Table 5) was purchased from Sigma-Aldrich (Sigma-Aldrich Corporation, USA) and used as received.

Table 5: a table of the sodium salts used and of their main properties

Name	Formula	CAS number	MW [g/mol]
Sodium acrylate		7446-81-3	94.04
Sodium methacrylate		5536-61-8	108.07

2.1.2.4 Graphite

Graphite (CAS 7782-42-5) was purchased from Sigma-Aldrich (Sigma-Aldrich Corporation, USA). It was used as a direct filler to improve mechanical and electrical properties, and also to try to synthesise graphene via ultra sounds exfoliation directly inside the monomer.

2.1.2.5 TEGO (*thermally expanded graphite oxide*)

TEGO graphene is a heavily reduced graphite oxide, 2% of oxygen and 0.4% hydrogen still present together with some vacancies in the structure, obtained by thermal exfoliation at high temperature (1323 K) produced by Professor Mauro Riccò research group at the Physics department of the University of Parma [123].

TEGO was obtained from highly pure graphite powder, 99% purity, average size 1.5 μm purchased from Sigma-Aldrich. The graphite powder, about 1 g, was completely oxidised following the Staudenmaier method [124,125]. The powder was added to a mixture of 17.5 ml of concentrated sulfuric acid and 9 ml of nitric acid in a fume hood and cooled by immersion in an ice bath. The mixture was kept under continuous stirring, while 11 g of potassium chlorate was slowly added over 1 h. The suspension was then stirred in a fume hood for 5 days under nitrogen flow, to avoid the potentially explosive concentration of chlorine dioxide gas. The colour of the mixture remained black. The suspension was then diluted in 800 ml of water and filtered through coarse filter paper. The filtered product was dissolved in 200 ml of 5% hydrochloric acid aqueous solution and filtered again, then carefully washed over the filter with water. Finally, the product was dried at 333 K overnight. After this step, the laboratory X-ray diffraction analysis showed that the inter-planar distance changed from 0.335 nm to 0.690 nm, due to the presence of intercalated water molecules and hydroxyl, carboxyl and epoxy groups attached to the graphene planes. When the product underwent thermal annealing at 373 K for 3 h in dynamic vacuum, which removed the water molecules, the interplanar distance decreased slightly to 0.622 nm, a value perfectly in agreement with that reported for graphite oxide (GO) [126,127].

Samples were obtained by a direct, fast annealing of GO under vacuum at 1323 K, thus obtaining the reduction and exfoliation of graphite planes, clearly visible as a sudden growth of sample volume up to thousand time of the initial GO volume (thermally expanded graphite oxide – TEGO) [128,129]. These high temperature treatments were done in order to guarantee the removal of possible residual hydrogen chemisorbed on the graphene planes [130,131]. After high temperature exfoliation, the sample have been always handled in pure Argon atmosphere (oxygen and moisture below 1 ppm). The vigorous exfoliation of graphite

Materials and methods

oxide at 1323 K led to a sample consisting of flakes with a porous layered structure whose overlapping sheet structure is evident in Figure 21 and Figure 22.

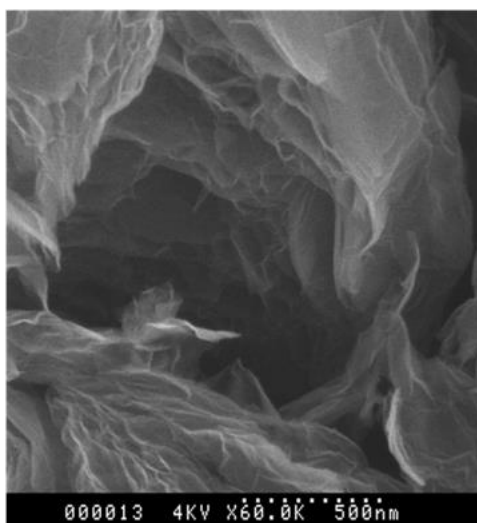


Figure 21: SEM images of GO vigorously exfoliated at 1323 K (TEGO)

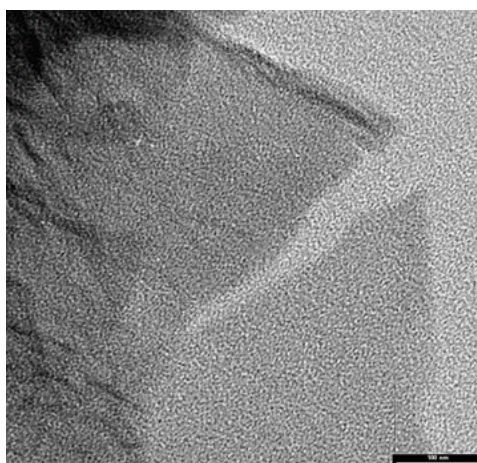


Figure 22: representative TEM image from TEGO, where stacked graphene sheets are present. Here a single layer sheet with a prominent tear and crumpling at the edge is observed. Scale bar indicates 100 nm

2.1.3 Additives

Some additives are always required to be mixed together with the base monomer and the optional filler. These additives can be photoinitiators to start the curing reaction or dyes to control the scattering of the light or even also reactive or non-reactive diluents to adjust the viscosity of the formulation.

Materials and methods

2.1.3.1 Initiators

Photoinitiators are used to start the curing reaction. Thanks to the light generated homolysis of the photoinitiator molecule, the formation of free radicals gives inputs for the polymerisation of acrylic and methacrylic monomers. Some thermal initiators have also been used for some comparative characterisation and are also presented.

2.1.3.1.1 Photoinitiators

Bis-(2,4,6-trimethylbenzoyl)-phenylphosphine oxide was used as photoinitiator and was purchased from BASF (Ludwigshafen am Rhein, Germany) under the trade name of Irgacure (Omnirad) 819 (CAS 423-340-5, Figure 23). Irgacure 819 is described as a versatile photoinitiator for radical polymerisation of unsaturated resins upon UV light exposure.

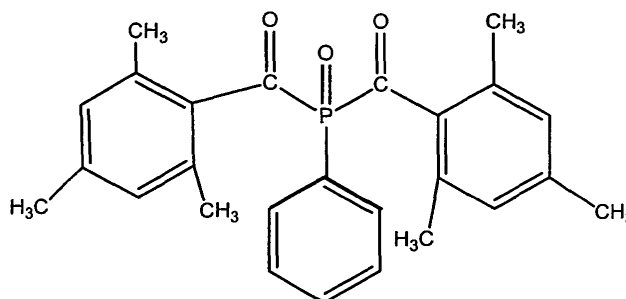


Figure 23: Bis-(2,4,6-trimethylbenzoyl)-phenylphosphine oxide (Irgacure 819) molecular structure

2.1.3.1.2 Thermoinitiators

Thermoinitiators have also been used, as already reported, for preliminary tests and comparative characterisation. However, it is important to remark that thermoinitiators have never been used in the VP machines, as there is no point in doing so on light based VP systems.

Materials and methods

Benzoyl peroxide (CAS 94-36-0, Figure 24) was purchased from Sigma-Aldrich (Sigma-Aldrich Corporation, USA) under the tradename of Luperox A75, and used as received. Benzoyl peroxide is a thermal radical polymerisation initiator.

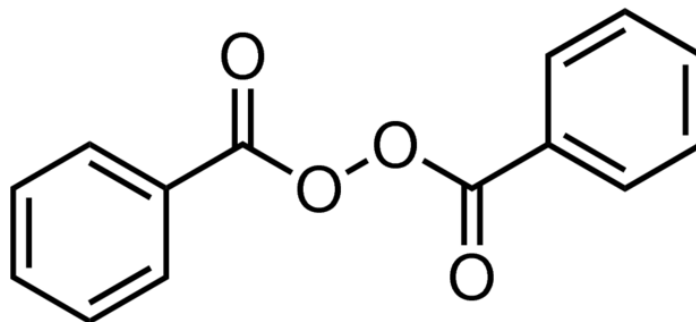


Figure 24: benzoyl peroxide molecular structure

AIBN (2,2'-Azobis(2-methylpropionitrile)) (CAS 78-67-1, Figure 25) was purchased from Sigma-Aldrich (Sigma-Aldrich Corporation, USA) and used as received. It is a thermal radical polymerisation initiator.

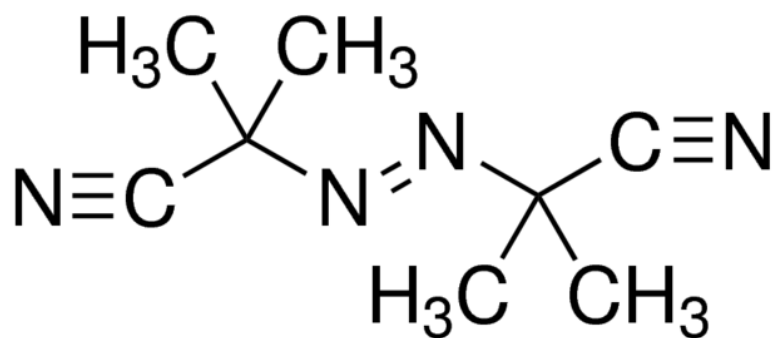


Figure 25: 2,2'-Azobis(2-methylpropionitrile) molecular structure

Materials and methods

2.1.3.2 Dyes (UV absorber)

Dyes are used in VP processes as UV absorber to limit the scattering of the light and avoid over curing.

1-Phenylazo-2-naphthol, Solvent Yellow (CAS 842-07-9, Figure 26) was purchased from Sigma-Aldrich (Sigma-Aldrich Corporation, USA) under the tradename of Sudan I, and used as received.

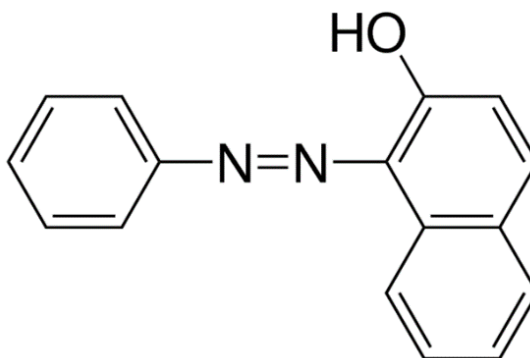


Figure 26: 1-Phenylazo-2-naphthol (Sudan I) molecular structure

2.1.3.3 Diluents

Water can be used to adjust viscosity, in the case that the liquid monomer is water miscible, or to solubilise metal salts like silver nitrate. It has also been used in the reaction synthesis of silver (meth)acrylate. The water used was always distilled.

Ethanol has been used, just like water, to dilute pure monomers in UV lamp preliminary tests, and to dissolve silver nitrate as well as in the synthesis of silver acrylate and methacrylate.

Materials and methods

PEGDA 700 has been used as a reactive diluent because of technological issues in the STLG system, since that machine required low viscosity formulations.

2.2 Technology

2.2.1 Hardware

2.2.1.1 Form 1+

A commercial inverted SLA printer (Form1+, Formlabs Inc., Somerville, MA, USA, Figure 27), was one of the machines used to process the photo-curable formulations. The objects were always printed with no supporting structures directly on the build platform. Figure 28, shows more in detail the inside of a Form 1+ printer with the inner disposition of laser and the galvanometric devices that control the laser direction with small orientable mirrors.

The recoating mechanism is based on the oscillation of the resin tank on a hinge that is situated laterally to it, this movement allows the replacement of the resin from the regions close to the printed surface to the outer borders and vice versa.



Figure 27: Form 1+ components scheme

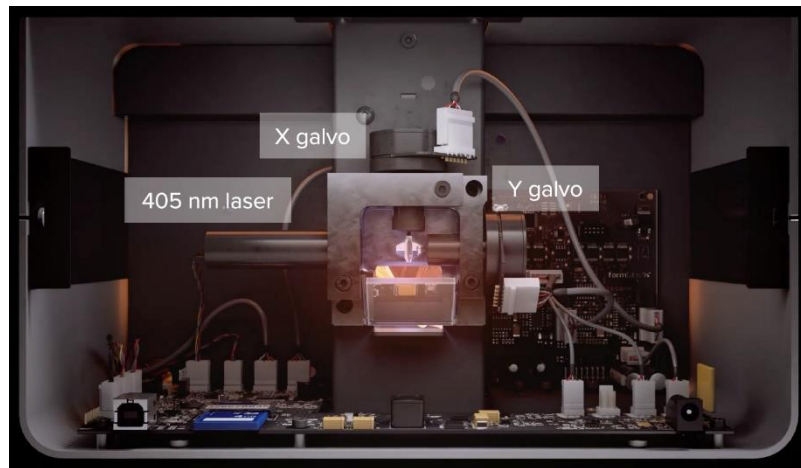


Figure 28: inside of Form 1+ case [132]

2.2.1.2 Form 2

Form 2 is simply the upgraded version of Form 1+, it is another commercial inverted SLA printer (Formlabs Inc., Somerville, MA, USA, Figure 29). The prices of the two SLA printers are very similar: around 3000 €. The main difference between Form 2 and Form 1+ is in the recoating system. The hinge based system of the Form 1+ has been updated with a blade-based one. The blade scans the surface of the resin tank to allow partially reacted resin to be replaced from the new, virgin one. Unfortunately, this recoating system is only available while using proprietary materials of Formlabs. When using a custom material, the mechanism is substituted by the build platform changing place inside the resin tank, thus mixing the resin every few layers.

The other differences between the two systems are reported in Table 6. Form 2 has bigger outer dimensions and a consequent bigger build volume. It has the same power requirements, but the laser has been improved to allow a smaller spot size. This characteristic brings to more accuracy, since the minimum feature size of the Form 2 is now smaller and the maximum curable layer thickness is greater.



Figure 29: Form 2, Formlabs

Table 6: technical specifications comparison between Form1+ and Form 2

Printer	Dimensions	Power requirement	Laser specifications	Build volume	Minimum feature size	Layer thickness
Form 1+	30 × 28 × 45 cm	100–240 V 1.5 A 50/60 Hz 60 W	405nm violet laser Spot size 155 microns	125 × 125 × 165 mm	300 micron	25-100 microns
Form 2	34.5 × 33 × 52 cm	100–240 VAC 1.5 A 50/60 Hz 65 W	405nm violet laser 250 mW. Spot size 140 microns	14.5 × 14.5 × 17.5 cm	100 micron	25-300 microns

2.2.1.3 Stereo-thermo-lithographic system - STLG

The stereo-thermo-lithographic (STLG) system (Figure 30) in the CDRSP laboratory of IPL (Leiria, Portugal), is a DLP based system. The wavelengths of the radiations that will interact with the resin have been chosen through appropriate filters

Materials and methods

The light source (Oriel 66942, Newport Corporation, Irvine CA USA, equipped with a 350 W mercury lamp) was set at a power of 300 W and provided a wide spectrum of radiation, from UV to IR. The wavelengths selected were the ones of blue light (FSR-BG38 Blue Glass Bandpass Filter, Newport Corporation, CA, USA, Figure 31), peaked around 4-500 nm (Figure 32), and a near-IR band pass filter (10LF30-1550 optical filter with centre wavelength 1550 nm and bandwidth (FWHM) of 30 ± 7 nm, from Newport Corporation, Irvine CA USA) (Figure 31). The blue light around 400 nm can be absorbed by the photoinitiator (as can be seen from the extinction diagram in Figure 33) and initiate the cross-linking reaction. The light intensity was measured with a radiometer (AccuPRO Plus XP-4000, Spectroline, Westbury, NY USA) and it was found to be 0.5 mW/cm². The use of Irgacure 819 as a photoinitiator in combination with blue light is very common and attested also in previous works not only by this research group [2,6,103,107,133–135]. While the blue light provides the energy to initiate the polymerisation reaction, IR radiation can provide the energy to pre-heat the resin and make a thermal treatment directly in situ while the printing process is still occurring.

The full spectrum radiation, once left the lamp, goes through a beam splitter that separate two different channels. Both the channels have their proper filter to select the wavelength needed and a shutter that allows to open and close the light beam irradiating from that channel, making possible to control separately the time of exposure for each channel. After this step the IR channel is aimed directly at the build platform, while the filtered blue light goes to the DMD (DMD Discovery 1100, Texas Instrument, Dallas TX USA). The DMD reflects the light with the square photomask in Figure 34, giving the desired shape to the light beam. The blue light beam is then focused on the build platform by a lens. Each shutter is programmed to enable the irradiation for a certain amount of time and, after each layer is completed, the build platform is lowered of a full layer thickness.

The vertical displacement of the build platform is secured by a positioner uniaxial MYCOSISR Translation Stage VT-80 (Physik Instrumente GmbH & Co. KG, Karlsruhe, Germany), which allows vertical increments of 1 μm (between 0.001 and 20 mm/s). The combination of two different light radiations brings to a more efficient generation of radicals, with respect to other VP techniques [75]. Also, a thermal post-treatment is possible within the printing process, reducing post-processing time and making the whole process lighter

Materials and methods

and easier. The heat provided by the IR radiation can also be exploited to pre-heat the resin making the whole system more reactive. This homemade thermo-stereolithographic system is controlled by a homemade software.

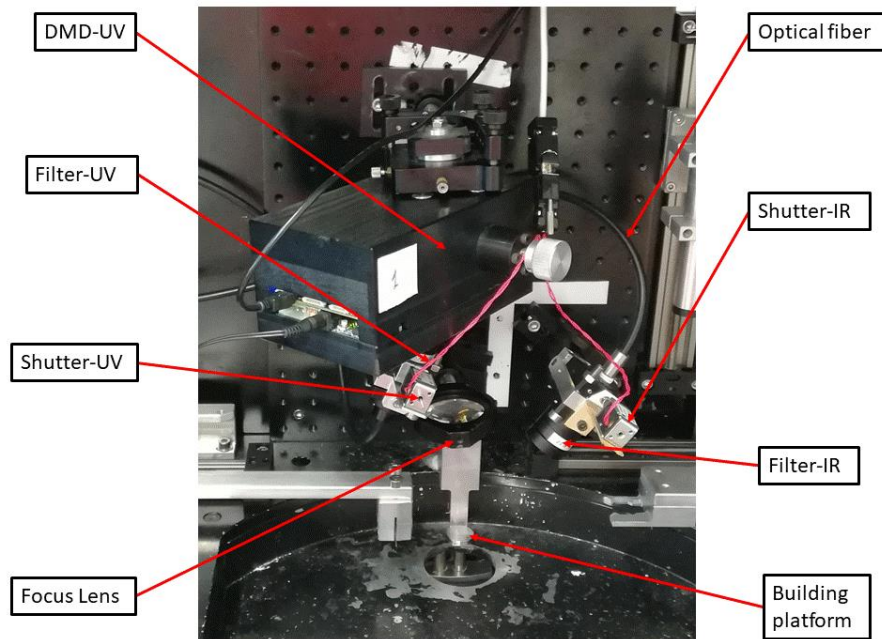


Figure 30: a photograph of the STLG printing system



Figure 31: FSR-BG38 blue glass bandpass filter (left) and 10LF30-1550 IR bandpass filter (right)

Materials and methods

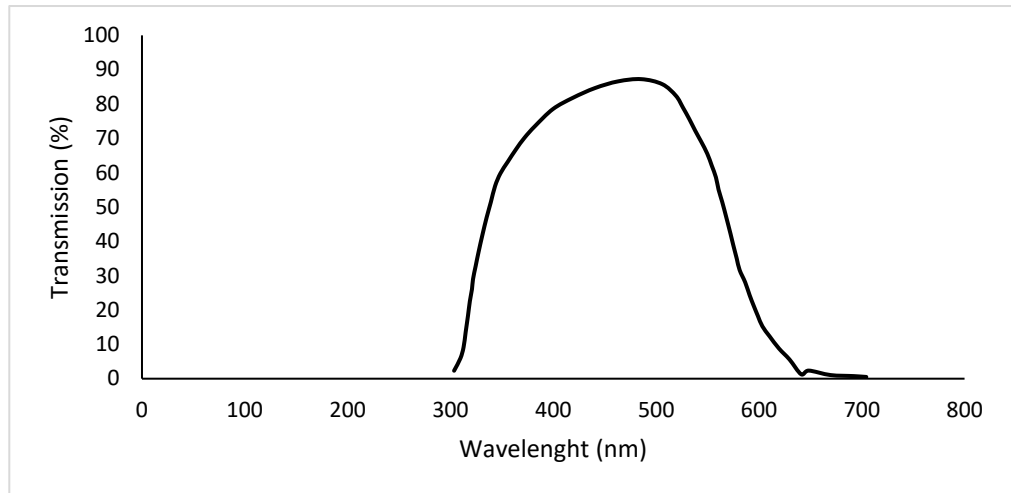


Figure 32: FSR-BG38 Blue Glass Bandpass Filter transmission diagram

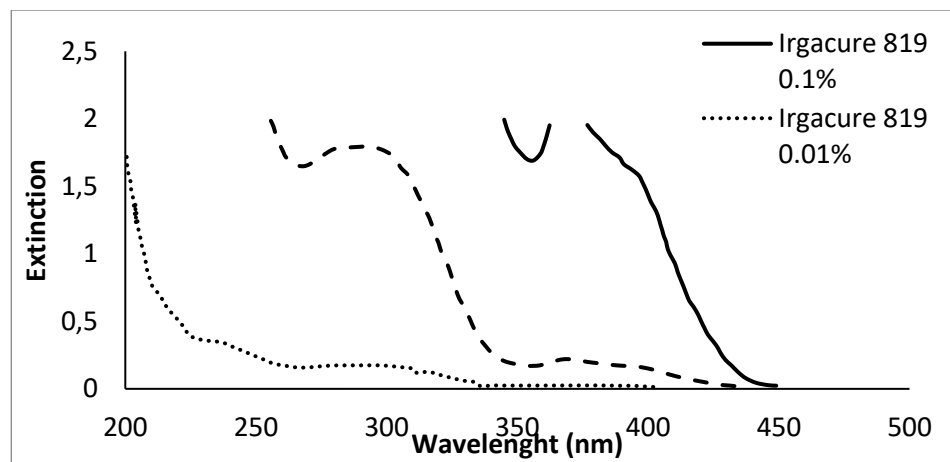


Figure 33: extinction diagram of Irgacure 819

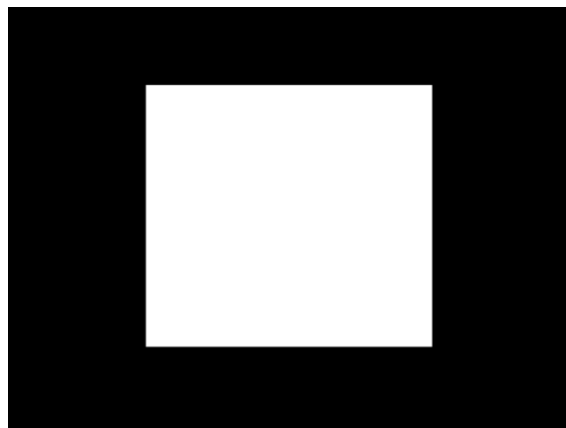


Figure 34: photomask for the DMD, 1024 x 768 pixels

Materials and methods

2.2.1.4 Process parameters

Each VP process has its own process parameters that must be managed in the right way to correctly print an object. Even small modification of the process parameters can make the difference between success and failure.

2.2.1.4.1 Disposition on the build platform

As reported, new monomer should flow in the irradiated area to replace the reacted one. This operation is called “recoating step”. Moreover, also the liquid monomer close to the irradiated area can be partially cured and, after each layer, it should be removed and replaced by virgin monomer flowing from the outer regions of the resin tank. Each printer has its own recoating system. Form 1+ has a movement of oscillation of the resin tank on the lateral hinge that can be seen on the right side of Figure 37. In the representations of sample disposition over the build platform, the hinge is on the right and the front is at the bottom.

A disposition of the samples too close to the hinge side (Figure 35) can result in poor quality of the printed objects due to overcuring (Figure 36), since the oscillation is minor closer to the hinge and the recycling of the resin can be difficult.

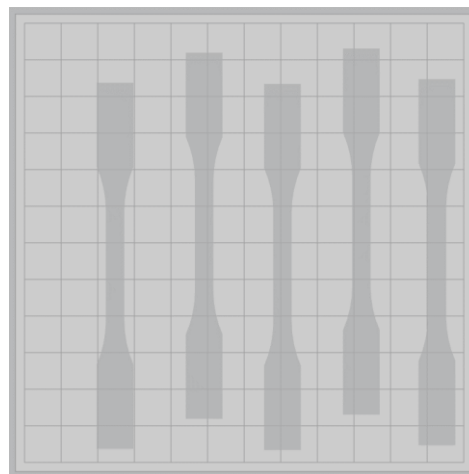


Figure 35: poor disposition of the samples on the build platform too close to the hinge on the right

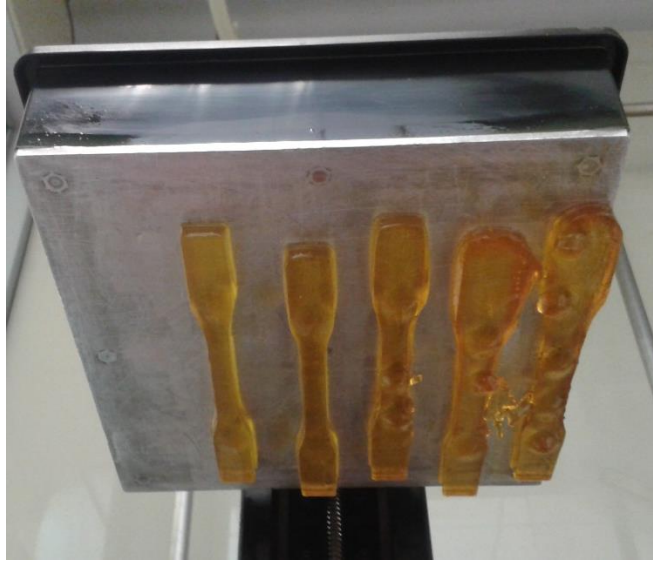


Figure 36: effects of the overcuring on the printed samples due to the poor disposition

A disposition like the one in Figure 37, can provide a better accuracy since the samples are distant from the hinge and the resin flow during oscillation is higher. The sample closer to the hinge has double spaces on each side to try to avoid resin stagnation. Unfortunately, it is still not enough and it is easy to have overcuring on it, mostly depending on the viscosity of the resin. The asymmetric disposition in Figure 39, is an attempt to avoid overcuring on the sample closer to the hinge, and it works better than the previous ones. Clearly the influence of the viscosity and the quantity and amplitude of the oscillation both strongly influence the phenomenon. As highlighted by Figure 37 and Figure 39, the spacing can partially supply to the closeness to the hinge.

Materials and methods

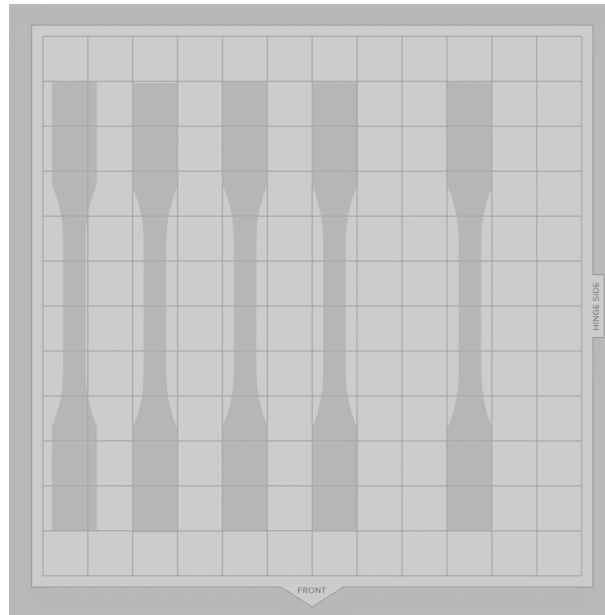


Figure 37: a better sample disposition, far from the hinge side



Figure 38: better sample disposition results, the sample on the right is still somehow slightly overcured

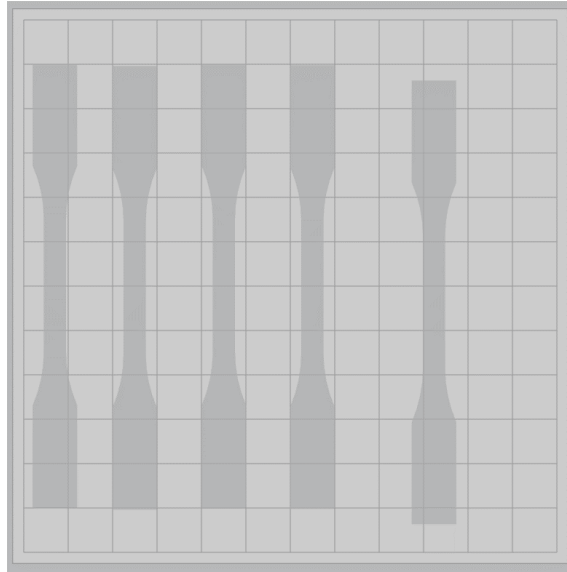


Figure 39: another better sample disposition, far from the hinge side and asymmetrical

Form 2 has completely different recoating and recycling mechanisms. A blade swipes the entire surface of the resin tank, making the choice of the disposition of the samples on the build platform less critical. In fact, it is possible to dispose the samples on the whole build platform surface just taking into account the considerations concerning distances between them.

Thanks to this new system, the relative positions of the resin tank and of the build platform can change every few layer, avoiding excessive consumption of the delicate resin tank silicone bottom. This mechanism is also the only one active in the “open mode” that can supply the resin recycling and prevent overcuring.

Open mode is an option of the Form 2 that allows to work with the blank settings of no specific Formlabs material. In open mode, the material has to be added manually to the resin tank and the blade system is disabled.

2.2.1.4.2 Offset

Another important process parameter is the offset in z direction. If the adhesion of the printed object to the build platform is too strong, it can happen that the samples cannot be easily removed from it. In these cases, it is needed to set an initial offset along the build direction capable to decrease the adhesion and ease the detachment operation, avoiding the damaging of the object during post-printing operations. Depending on the formulation, offset values can reach 1 mm.

2.2.1.4.3 Layer thickness

Layer thickness is probably the most evident process parameter, as it affects heavily dimensional accuracy in z direction and process times. Thinner layers guarantee better accuracy and the mitigation of the staircase effect (Figure 40), but they increase the printing time. A balance should be found between these two effects.

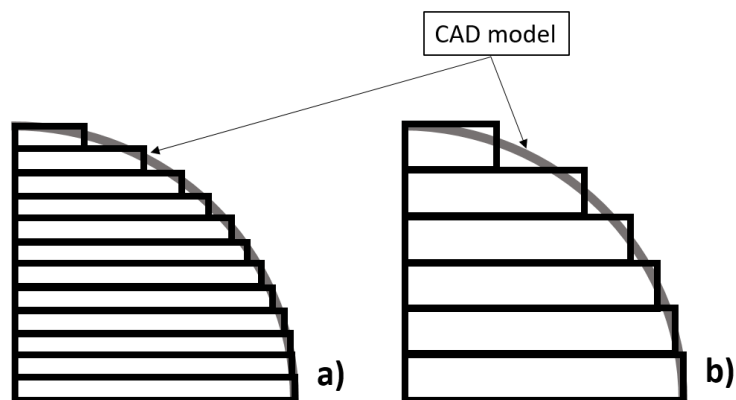


Figure 40: staircase effect depending on the layer thickness: finer (a) and higher (b)

2.2.1.4.4 DLP and SLA process parameters

DLP has some specific process parameters corresponding to the ones of SLA. The SLA laser power is the equivalent of the light emission power, as well as the time of exposure *per* layer is somehow corresponding to the laser scanning speed on the raster of the layer.

2.2.2 Software

2.2.2.1 *Preform (with Openform)*

Preform is the Formlabs printers' software. It can pre-process the STL files and set them for the printer. It can scale, orientate, generate support, dispose and slice the objects to be printed (Figure 41).

Preform has also an open version, called Openform, that allows to access to the process parameters that are normally unavailable for modification, like laser intensity and scan speed, spacing (Figure 42) and path (Figure 43). It is also possible to differentiate between base, support and model parts (Figure 44), adjusting the process parameters for each section.

Materials and methods

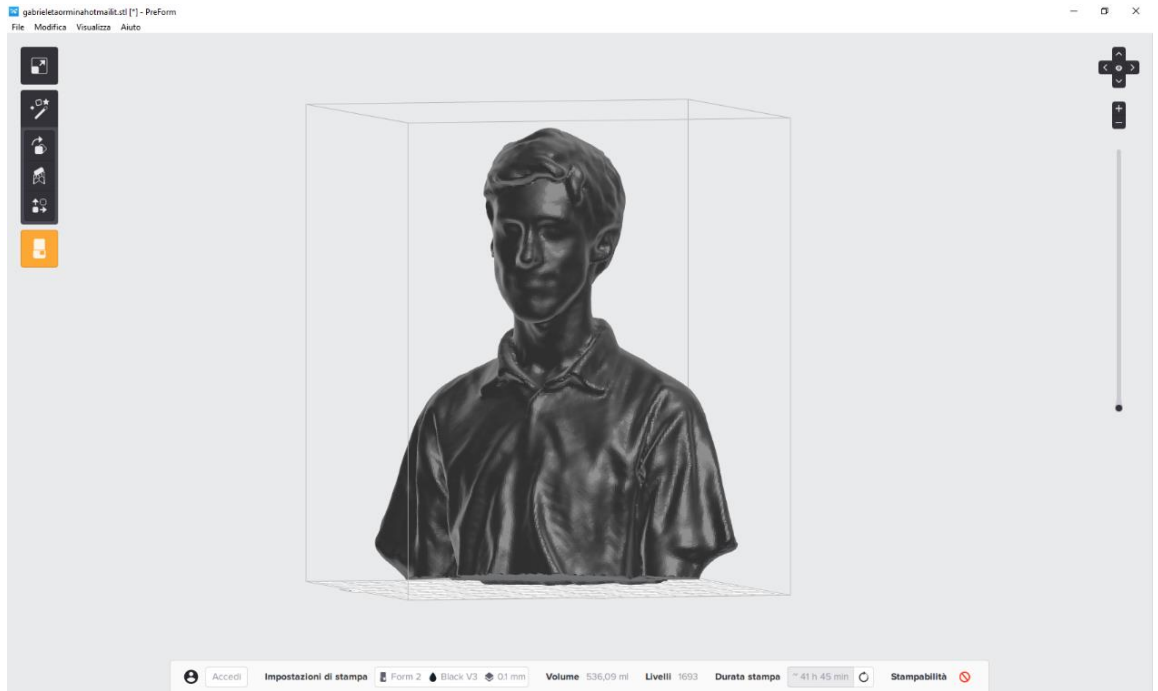


Figure 41: Preform interface

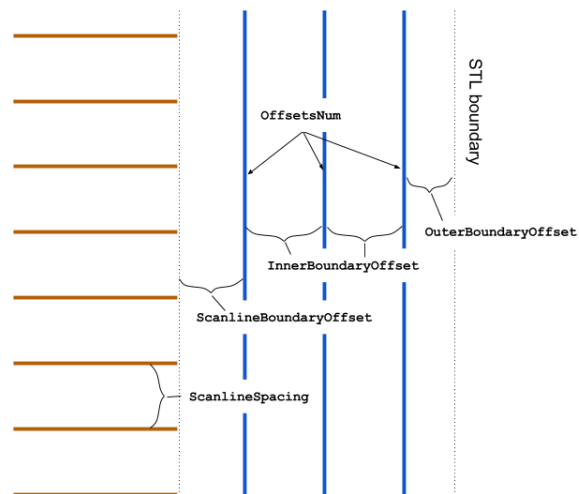


Figure 42: process parameters available with Openform

Materials and methods

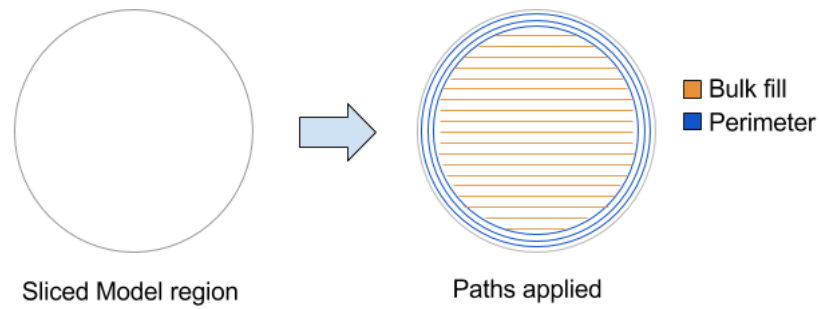


Figure 43: paths of the laser scan applied for each model slice, the perimeter is considered differently from the bulk

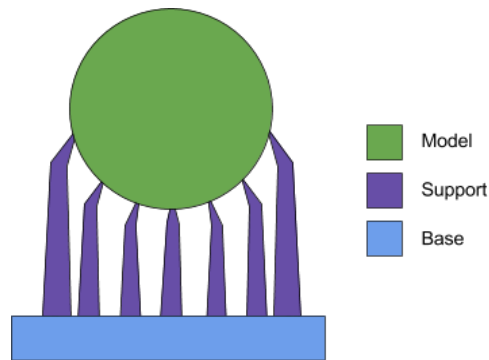


Figure 44: the three different regions of an additive manufactured object: the base attached to the build platform, the supports and the model

2.2.2.2 STLG printer manager program

The homemade thermo-stereolithographic system was controlled by a simple homemade software. The software gave the option to set the process parameters like layer thickness, illumination time for each layer and for each radiation, wait time between layers and dipping of the build platform inside the resin tank. The software was also able to receive and send the photomasks to be projected by the DMD (which has a resolution of 1024 x 768 pixels, 14 mm in size) that were drawn with Paint (Microsoft Corporation, Redmont WA, USA) on a 1024 x 768 pixels format.

Materials and methods

2.2.2.3 Electrical data measurement custom software

A simple software was coded and used to run the programmable microcontroller Genuino 101 and manage the collection of data from the electrical measurements performed (Figure 45).

```
//arduino code :
// number of analog samples to take per reading
#define NUM_SAMPLES 10
float sum = 0; // sum of samples taken
int sample_count = 0; // current sample number
float voltage = 0.0; // calculated voltage
float milli_time = 0; // time in milliseconds
void setup(){
  while(!Serial); //wait for serial connection to start
  pinMode(A2,INPUT);
  Serial.begin(9600);
  Serial.println("CLEARDATA");
  Serial.println("LABEL,Time,Time (milli Sec.),Volt"); //header for excel
}
void loop(){
  // take a number of analog samples and add them up
  while (sample_count < NUM_SAMPLES) {
    sum += analogRead(A2);
    sample_count++;
    delay(1); //here set the number of measurments per second
  }
  milli_time=millis(); //log time of measurement in milliseconds
  voltage = ((float)sum / (float)NUM_SAMPLES * 3.3000) / 1024.0; //calculate the voltage from analog readings
  //output data through serial port
  Serial.print("DATA,TIME,");
  Serial.print(milli_time);
  Serial.print(",");
  Serial.println(voltage);
  sample_count = 0;
  sum = 0;
  delay(10); //here set the time between diferent measurments
}
```

Figure 45: software for the programming of the Genuino 101 microcontroller

2.2.2.4 SolidWorks

The CAD software SolidWorks (Dassault Systems SolidWorks Corporation, Waltham, MA, USA) was used to design the model for the specimens and the objects printed. The CAD files were subsequently converted to a STL file to be processed by the printer software.

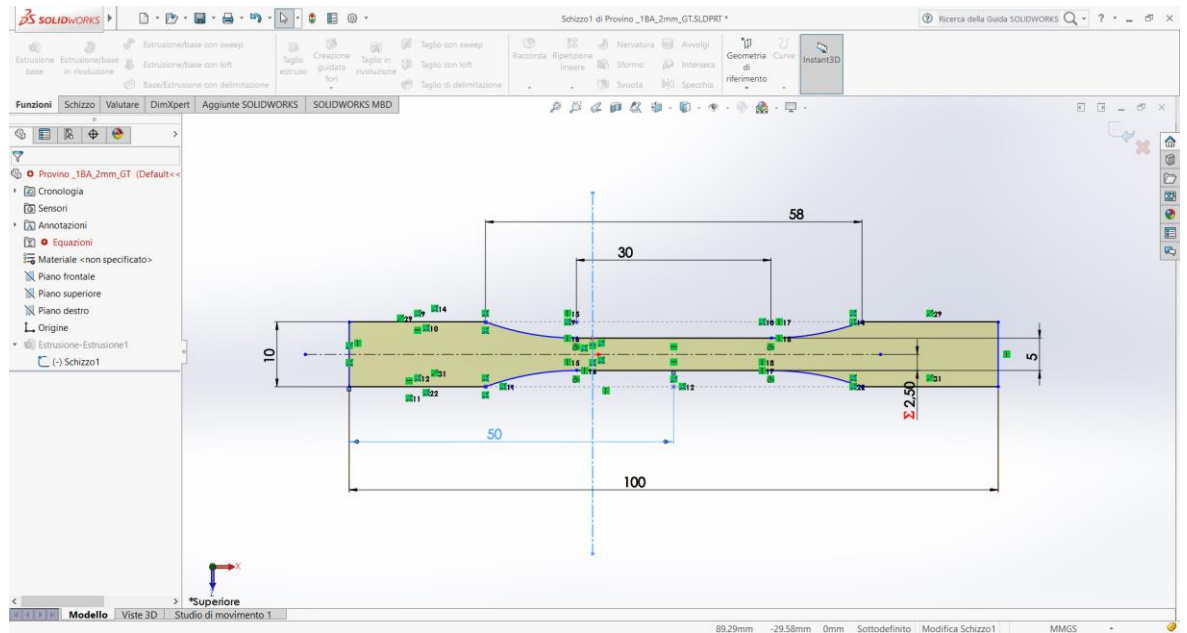


Figure 46: SolidWorks interface

2.2.2.4.1 Partial-contact models: a no-success story

The accordance between the quasi-linear strain threshold as determined from mechanical and electrical quantities suggests a strong correlation of the two observed phenomena. This brought to consider the electrical conductivity below the quasi-linear strain threshold as an indirect measurement of the effective mechanical contact, that is hardly observable using compressive tests. This idea implies that a mathematical model for the partial-contact area can be devised, to explore the interface of the sample under test. Seven models have been considered, to find the appropriate one: linear, pyramid (concave and convex), barrel (concave and convex), paraboloid (concave and convex).

Their representations are given in Figure 47, while the resulting mathematical models are summarized in the following equations. Unfortunately, none of the models given above fitted the data with the desired accuracy: the partial contact can be observed electrically, but further research is needed to find the proper model.

a) Linear: $S(h) = \frac{h}{h_{ql}}$

b) Pyramid (convex): $S(h) = \frac{h^2}{h_{ql}^2}$

c) Pyramid (concave): $S(h) = \frac{h}{h_{ql}} \left(2 - \frac{h}{h_{ql}} \right)$

d) Barrel (convex): $S(h) = \sqrt{\frac{h}{h_{ql}}}$

e) Barrel (concave): $S(h) = 1 - \sqrt{1 - \frac{h}{h_{ql}}}$

f) Paraboloid (convex):

$$S(h) = \frac{\pi}{2} \frac{h}{h_{ql}} \text{ if } h \leq h_{ql}/2$$

$$S(h) = \frac{\pi}{2} \frac{h}{h_{ql}} + \sqrt{\left| 2 \frac{h}{h_{ql}} - 1 \right|} - 2 \frac{h}{h_{ql}} \arctan \left(\sqrt{\left| 2 \frac{h}{h_{ql}} - 1 \right|} \right) \text{ if } h \geq h_{ql}/2$$

g) Paraboloid (concave):

$$S(h) = 1 - \frac{\pi}{2} \left(1 - \frac{h}{h_{ql}} \right) \text{ if } h \leq h_{ql}/2$$

$$S(h) = \frac{\pi}{2} \frac{h}{h_{ql}} - \sqrt{2 \left(1 - \frac{h}{h_{ql}} \right) - 1} - 2 \left(1 - \frac{h}{h_{ql}} \right) \arctan \left[\sqrt{2 \left(1 - \frac{h}{h_{ql}} \right) - 1} \right]$$

$$\text{if } h \geq h_{ql}/2$$

In these equations:

S : is the area projected by the model in the z direction, depending on h ;

h : is the height considered on the model;

h_{ql} : is the height of quasi-linearity at which the model is collapsed into a parallelepiped.

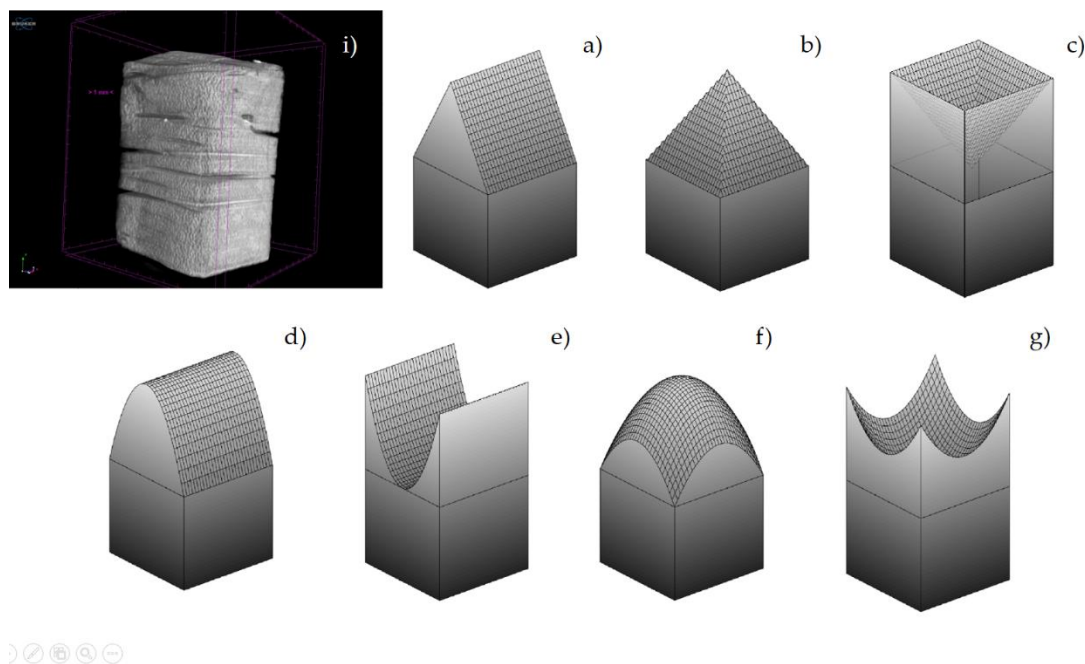


Figure 47: a micro-CT image of a STLG printed sample (i) and the images of the models used: linear (a), pyramid convex (b), pyramid concave (c), barrel convex (d), barrel concave (e), paraboloid convex (f), paraboloid concave (g)

2.3 Methods

2.3.1 Dispersion and homogenisation

Dispersion has been performed with different techniques, manually with spatulas and mechanically with magnetic stirring plates and ultraturrax or even by ultrasound (both with ultrasonic tip and bath)

UP200Ht ultrasonic tip (Hielscher, Teltow Germany) (Figure 51) at 40 W with an amplitude of 70% for 5 h in an ice and water bath kept cold to prevent reactions of thermally activated polymerisation.

Materials and methods



Figure 48: UP200Ht ultrasonic tip, Hielscher

T 25 digital ULTRA-TURRAX, (IKA, Staufen, Germany, Figure 49) is a high-performance disperser that can work at 3.000 – 25.000 rpm with small quantities of material. It has been used to disperse homogeneously silver salts inside the liquid monomers.



Figure 49: T 25 digital ULTRA-TURRAX, IKA

Materials and methods

A high-speed centrifuge (NEYA 16, REMI Neya Centrifuges, Carpi, Italy, Figure 50) capable of reaching 16.000 rpm was used to separate the supernatant from the salt in silver (meth)acrylate synthesis.



Figure 50: NEYA 16, REMI Neya Centrifuges

2.3.1 Matrix initial tests under UV lamp

Before proper VP printing process, the materials and the formulations were tested on a smaller scale to investigate reactivity of the system under UV irradiation and mechanical properties of the cured material. Every initial test was conducted under UV lamp, the liquid formulations, all containing 1% of Irgacure 819, were injected inside specially designed double glass slide moulds (Figure 51). Each formulation was cured under UV lamp for 30 minutes, 15 minutes on each side. After curing the samples were post-processed in oven at 80°C for 2 hours to complete curing.

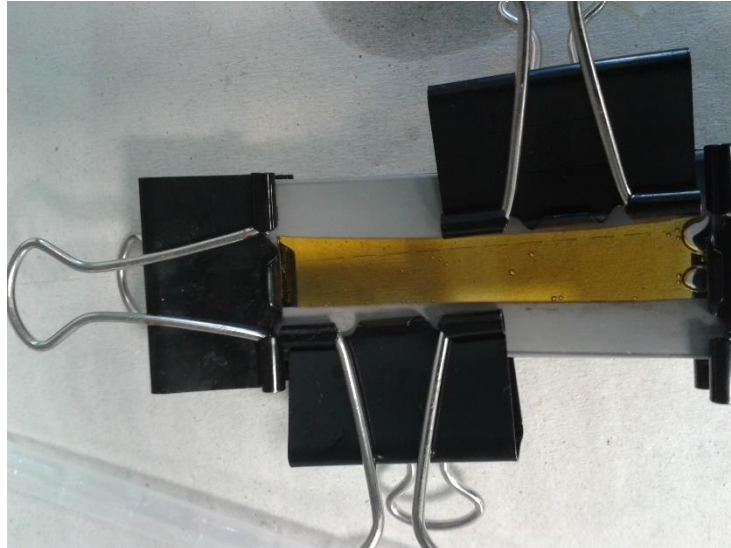


Figure 51: double glass slide mould for initial test under UV lamp

2.3.2 VP processes

The general AM process has been outlined, but hereafter some specific procedures adopted in this research are presented, to better understand all the technological issues concerning a VP process.

In Figure 52 the scheme for the realisation of unfilled PEGDA formulations is represented. The green section concerns the software procedure, from CAD design of the model to be printed, to the handling of it in the machine software, and to the final upload of the job into the SLA printer. In yellow the material part, from the preparation of the monomer formulation, to the addition of photoinitiator and dye, and to the stirring of the solution until complete homogenisation. Finally, in red the proper printing step, followed by the post-processing: washing and UV post-curing.

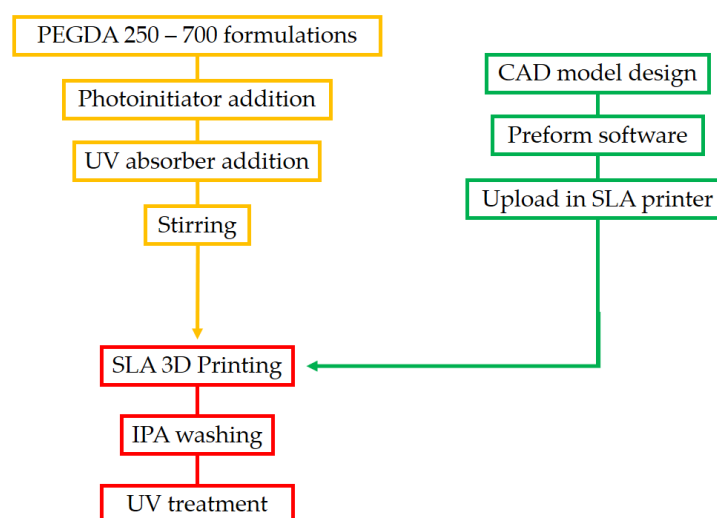


Figure 52: a scheme of the entire SLA process for unfilled samples, from the preparation of the formulations and CAD design to the post-treatments

A set of five different formulations was prepared for SLA printing: from pure PEGDA 250 (PEGDA-A) to pure PEGDA 700 (PEGDA-E), as shown in Table 7. Each of these formulations was obtained stirring the oligomers together with 0.25%wt of Irgacure 819 and 0.005%wt of Sudan I, at room temperature until complete solubilisation. Then, the obtained solution was poured into the resin tank of a commercial inverted SLA printer (Form 2, Formlabs Inc., USA) that processed the photoreactive formulations.

Sample name and composition	PEGDA-A	PEGDA-B	PEGDA-C	PEGDA-D	PEGDA-E
PEGDA 250 (%)	100	75	50	25	0
PEGDA 700 (%)	0	25	50	75	100

Table 7: table of the five different formulations prepared highlighting the relative percentages of the two monomers

The layer thickness was set to 100 μm . The specimens were produced with the stacking direction along the specimen thickness and used for the subsequent characterisations (Figure 53). The printing process lasted approximately 1.5 hours.

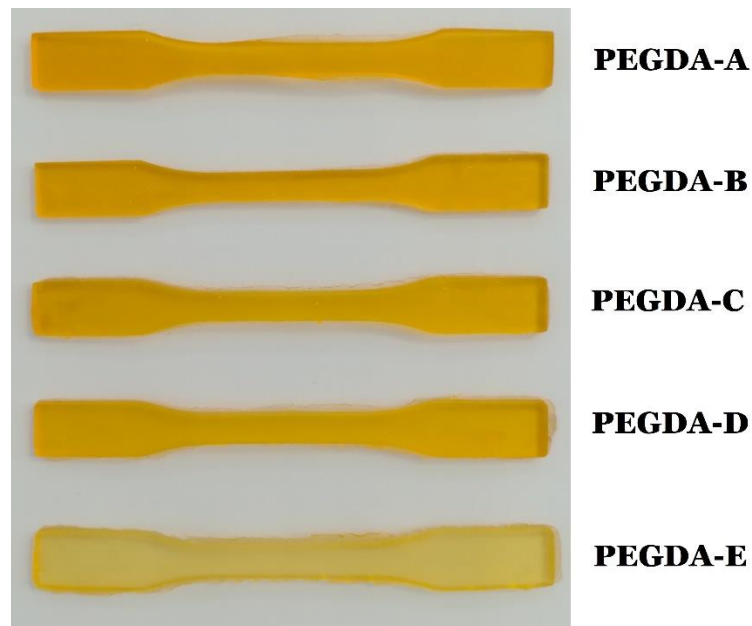


Figure 53: An image of printed samples

It was observed that the reactive formulation is stable for the whole printing period without any side-reaction or phase separation.

After printing, the specimens were detached from the build platform and rinsed in iso-propyl alcohol (IPA) for 20 minutes to fully remove all the residues of unreacted resin. An UV post-treatment was performed on the obtained specimens for 30 minutes on a UV lamp (DYMAX model 5000 Flood, 400 W UVA, metal halide bulb).

Figure 54 represents the scheme of the whole SLA process for silver nanocomposites. In green the software part, same as in the previous case of unfilled samples. In yellow the preparation of a part of the formulation: PETIA was mixed with the photoinitiator and stirred overnight until complete solubilisation of the latter (B). In blue the preparation of the other part of the monomer formulation, the one containing the silver precursor salt. The salt can be synthesised or directly added to the Ebecryl 7100, with the addition of a small quantity of EtOH to ease dispersion. Once reached a homogeneous dispersion, the EtOH was extracted and the dispersion of salt inside the monomer (A) was mixed together with the PETIA and Irgacure solution (A). In red the last steps, from mixing of the two part of the formulations to the actual SLA process to the washing and thermal curing post-treatments.

Materials and methods

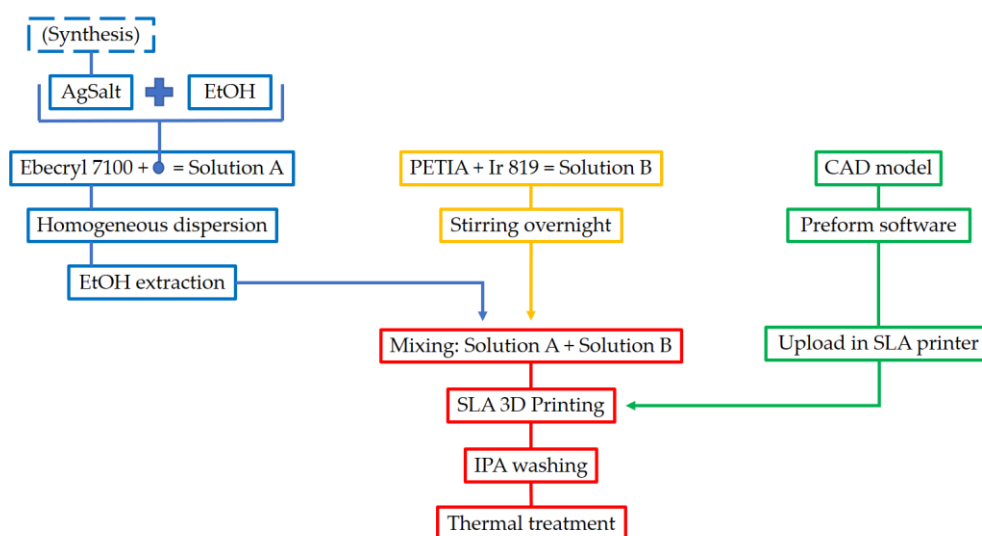


Figure 54: a scheme of the entire SLA process for silver nanocomposites, from the preparation of the formulations and CAD design to the post-treatments

The photo-curable resin was obtained by mixing together two different mixtures (A and B) for a total of 100 g, shortly before the printing step. The A mixture was formed by 33 g of PETIA with the addition of 0.25 wt % of Ir 819 with respect to the total final mass. This mixture was mixed overnight until complete dissolution of the photo-initiator. The B mixture was formed by 67 g of Ebecryl 7100 and a suitable quantity of silver salt, necessary to obtain the required concentration of AgNPs in the final sample. To ease the dispersion in the resin, a small quantity of ethanol was added to the salt and removed afterwards by a dynamic vacuum treatment on the solution carried out at room temperature. A photo-curable resin formulation was also prepared without the presence of silver salts, as reference material.

The samples were coded “AgAcr $x\%$ ” and “AgMAcr $x\%$ ” for polymers containing AgNPs obtained from silver acrylate and silver methacrylate as precursors, respectively ($x = 0.5, 1$ and 2 corresponds to the nominal weight percent of AgNPs, by assuming a complete conversion of silver salt to metallic silver).

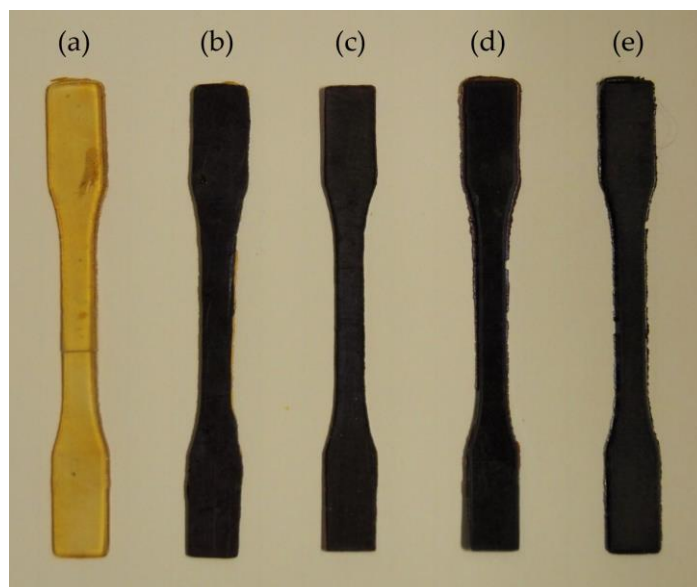


Figure 55: 3D printed specimens: (a) unfilled; (b) 0.5% AgAc; (c) 1% AgAc; (d) 2% AgAc; and (e) 1% AgMAc.

A commercial inverted SLA printer (Form 2, Formlabs Inc., Somerville, MA, USA) was used to process the photo-curable formulations. The layer thickness was set to 50 μm . The specimens were produced with the stacking direction along the specimen thickness and used for the subsequent structural and functional characterisations (Figure 55). The printing process time was between 1.5 and 2 h and the photo-curable formulation was observed to be stable for the whole period without any phase separation or side-reactions. The expected reactions occurring during the 3D printing step are shown in Figure 56.

At the end of the printing step, the specimens were detached from the build platform and rinsed in *iso*-propyl alcohol (IPA) for 20 min to fully remove all the residues of unreacted resin. Finally, a thermal post-curing treatment was carried out at 90 $^{\circ}\text{C}$ for 1 h, to complete the polymerisation process partially inhibited by the addition of the silver salt (see DSC results reported below).

Materials and methods

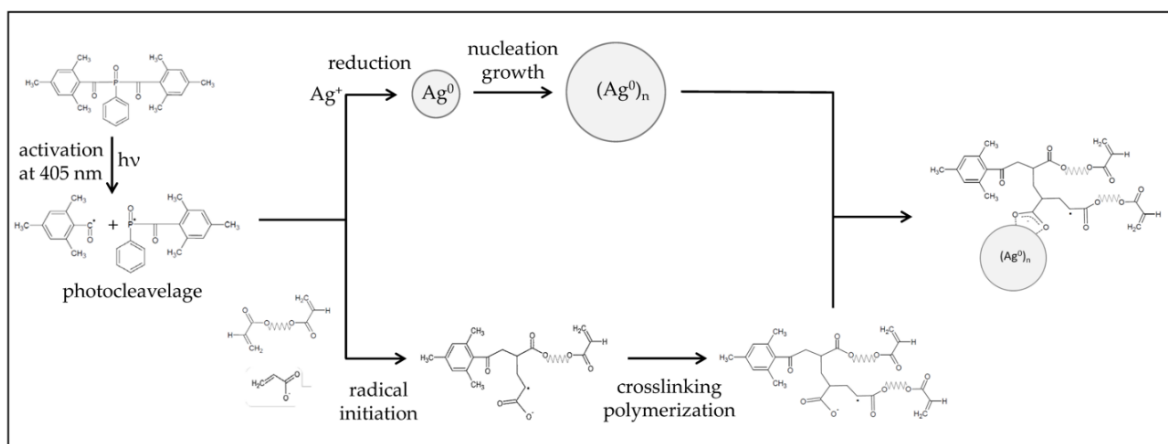


Figure 56: Scheme of the expected reactions during the 3D printing process (b).

Figure 57 represents the scheme of the whole process of STLG from preparation of the formulation and photomask design, to the post-treatments. In blue the preparation steps of the formulation. This stage is similar to the SLA process, the only part changing is the addition of carbon-based fillers like micro graphite and TEGO to the formulation and the monomer composition. In yellow the part relative to the formulation of monomer and photoinitiator. PETIA was substituted with PEGDA for technological reasons and its greater affinity with Irgacure 819. In green the software part, from the design of the photomask to be projected to its upload in the DMD and the programming of the printer custom software. The red part is relative to the last steps, the final mixing of the formulation, the proper STLG printing and the washing post-process.

Materials and methods

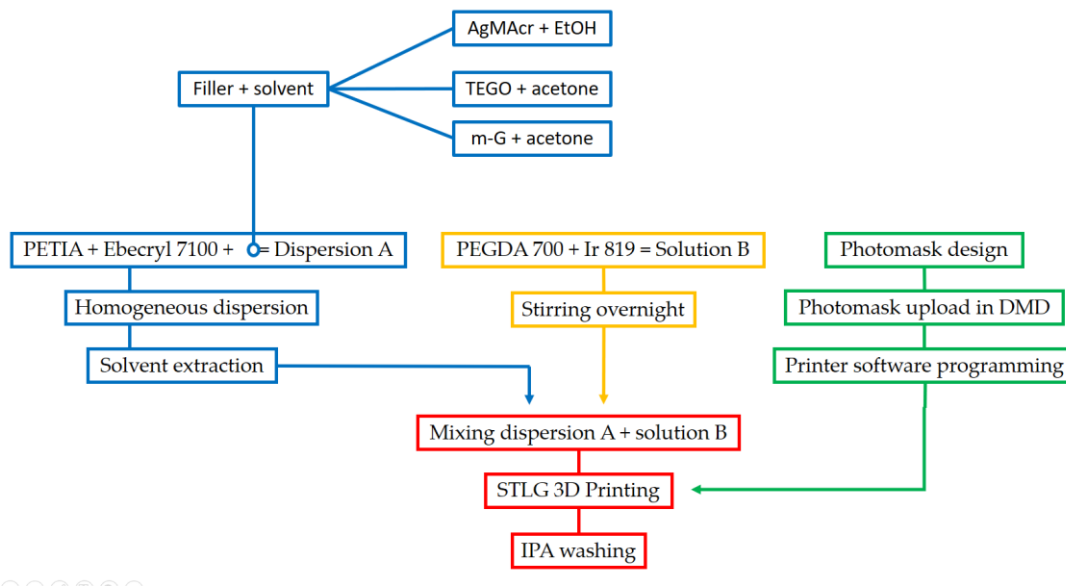


Figure 57: a scheme of the entire STL process for silver, graphite and TEGO composites, from the preparation of the formulations and DMD set up to the post-treatments

The first step in the sample preparation is the addition of the proper solvent to the different fillers. The solvent has the function to promote the dispersion of the filler into the liquid monomer matrix. The solvent adopted for the dispersion of the AgMAcr was EtOH, following the procedure adopted in 2.1.2.1.2, while acetone was used for the carbonaceous fillers (1 g for the m-G and 10 g for the TEGO). Once obtained, the mixture of filler and solvent was added to 15 g of PETIA and 30 g of Ebecryl 7100 to form the dispersion A. The dispersion A was homogenised by mechanical mixing in the case of AgMAcr or with the aid of ultrasounds for TEGO and m-G. The C-based fillers were dispersed into the resin using an UP200Ht ultrasonic tip (Hielscher, Teltow Germany) at 40 W with an amplitude of 70% for 5 h in an ice and water bath kept cold to prevent reactions of thermally activated polymerisation. The dispersion A, opportunely mixed to be as homogeneous as possible, underwent a step of solvent extraction under dynamic vacuum for 1 h, to remove all the possible residues of solvent that could have altered the properties of the composite. The dispersion A was now ready to be mixed with the dispersion B. Dispersion B was obtained stirring overnight until complete dissolution 1 g of the photoinitiator Ir 819 into PEGDA 700. After a homogenisation mixing, the total dispersion was poured into the printer's vat and was ready for the printing process.

Table 8: prospect summing up the main process parameters used to print the four different sample types

Name	Ir 819	Filler	Filler content wt%	Layer thickness (μm)	Blue light irradiation per layer (s)	IR irradiation per layer (s)
Control	1 phr	-	-	250	12	22
Silver	1 phr	AgNPs	0.5	250	12	22
m-G	1 phr	m-G	0.1	250	12	22
TEGO	1 phr	TEGO	0.1	250	12	22

All the main process parameters were kept constant (Table 8). The acrylic resin matrix composition (PEGDA 700 50%, Eb 7100 33%, PETIA 17%) is the same used in other works by this research group [2][135], whom had the same relative proportion between PETIA and Eb 7100 that is used here. The new element is the noticeable addition of the same amount of PEGDA 700 as a reactive diluent. This change in the composition is due to the technical limitations typical of a prototype printer. In this case the viscosity of the PETIA and Eb 7100 only system was too high to be successfully processed in the actual printer's vat and building platform system. The used photoinitiator quantity is set to the relatively high amount (1 phr) because of the strong absorption action performed by the filler; in fact filled compositions with even more than 0.6 phr of Ir 819 resulted in badly polymerised specimens, while unfilled compositions with just 0.125 phr reached a perfect degree of polymerisation. However, the photoinitiator quantity was kept constant also for the unfilled control samples, to better compare the results.

The filler content of the AgMAcr samples is 0.5 wt% of AgNPs obtained through *in situ* reduction of the silver methacrylate precursor, following the same steps presented also in [2].

The filler content of the carbonaceous fillers, micrometric size graphite and nanometric size TEGO, is the same (0.1 wt%). This quantity was kept constant to analyse the effect on properties of the size of the filler particles.

The layer thickness was set to 250 microns, which is higher than many commercially available VP systems. Thus, giving the whole process very short printing times. This aspect

Materials and methods

is enhanced also by the action of the IR radiation that helps to avoid any post-process curing treatment, further reducing the process time and complexity.

The differences between blue light and IR irradiation times is due to the different power of the radiations involved, the final parameters were found experimentally. This tuning process involved all the printing parameters because they are somehow all connected: an increase in the photoinitiator can compensate an increase in the filler content or a decrease in the irradiation time for example, but in the end an equilibrium must be guaranteed. If there is not enough photoinitiator or irradiation or too much filler the polymerisation could not start at all or fail during the process, vice versa it can happen to have over-polymerisation and polymerise on the whole building platform instead of the irradiated area only.

All the printing parameters, like layer thickness and irradiation times, were set in the home-made software controlling the entire system.

Regarding the sample dimension, the D695 ASTM standard for compression test [136] was followed; however, in designing the specimens, the suggested dimensions had to be normalised to match the limitations imposed by the printer itself. In fact, the suggested dimensions for the prism specimens ($12.7 \times 12.7 \times 25.4 \text{ mm}^3$) were roughly multiplied by a 0.75 factor, because of the limitations in the optical system (the irradiated area was well-focused just in the middle of the building platform) and in the maximum height allowed for the printing process (20.2 mm). Those limitations are normal while working with a prototype non-commercial printer. An image of the printed samples can be seen in Figure 58.

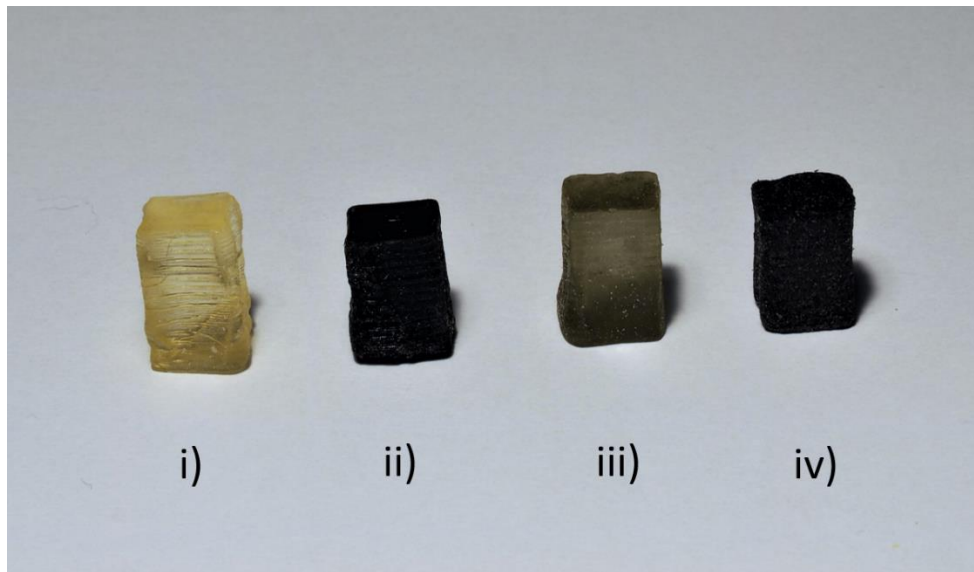


Figure 58: 3D printed specimens: i) control; ii) AgMAcr; iii) m-G; iv) TEGO

The control unfilled sample in Figure 58(i) is transparent because of the absence of any filler while the yellowish colour is given by the relatively big amount of photoinitiator. Still partially transparent is the iii) m-G filled specimen due to the micrometric size of its filler, while ii) and iv) are completely opaque and black because of the nanometric dimensions of their fillers.

2.4 Material Characterisation

Appropriate characterisation tests are vital to build and improve the knowledge on the produced samples, making it possible to understand the material properties and characteristics and allowing the process of improvement of those properties.

2.4.1 Differential Scanning Calorimetry - DSC

Differential scanning calorimeters are instruments capable to measure temperatures and heat flows associated with thermal transitions in a material. It is possible to measure

Materials and methods

with a DSC properties like glass transitions, “cold” crystallisation, phase changes, melting, crystallisation, product stability, cure / cure kinetics, and oxidative stability. In this work, DSC has been used mainly for the analysis of curing temperatures and temperature stability.

Differential scanning calorimetry (DSC) analyses have been carried out at a heating rate of 10 °C/min, generally from -10 to 200 °C in nitrogen atmosphere (DSC, TA2010, TA Instruments, New Castle, DE, USA).

2.4.2 X-ray diffraction - XRD

X-ray diffraction analysis is a characterisation technique that gives information on the crystalline nature of an observed specimen. It uses an x-ray incident beam that scatters crossing the specimen following the Bragg’s law. The resulting intensities of the scattered beam at specific angles form characteristic peaks that give information about the crystalline phases present inside the analysed specimen.

XRD analyses were carried out at in continuous-scanning mode between on wide 2θ angle ranges, on an X’Pert PRO diffractometer (PANalytical, Almelo, The Netherlands).

Since the quantities of crystalline phases to observe inside the amorphous polymer matrix were small, the tests were conducted over long time periods (often more than 10 hours) and using a thick incident beam to collect as much signals as possible (e.g. one of the measurements was carried out between 30° and 85° 2θ angle with a scanning rate of 0.00013° s⁻¹ (step size of 0.002° 2θ and 150 s as counting time)).

2.4.3 Scanning Electron Microscopy - SEM

Some of the samples were observed using a scanning electron microscope (ESEM, FEI Quanta, The Netherlands) operated in high-vacuum mode. The samples were prepared joining them to the sample holder (stub) by means of an adhesive carbon tab. Silver glue was

Materials and methods

also used to link the upper surface of the sample to the conductive carbon tab to create a conductive path that allows electrons to flow. The samples were metallised by plasma sputtering 10 nm of gold on their surface with an Emitech metallising system. This preliminary preparation was necessary to observe the samples in high vacuum because polymers are not conductive. Micrographs can be acquired at different magnifications and microanalyses can be performed where necessary. The microanalyses have been carried out by means of an X-EDS microanalysis system (INCA Oxford Instruments, U.K.).

2.4.4 Transmission Electron Microscopy - TEM

Since nanoparticles have nanometric dimensions, to better observe them it is necessary to shift from SEM to TEM. TEM microscopy was carried out (Tecnai 12 Gspirit electron microscope, FEI Company, Hillsboro, OR, USA) by using an accelerating voltage of 120 kV and LaB₆ as electron source.

2.4.5 Dynamic-mechanical thermal analysis - DMTA

DMTA can provide precious information on the mechanical and thermal properties of a material. These analyses were carried out on a TA 800Q DMA instrument (TA instruments, New Castle, DE, USA) equipped with a single-cantilever clamp. Suitable specimens with rectangular shape ($5 \times 2 \times 30 \text{ mm}^3$) were obtained from the narrow parallel-sided portion of the 3D printed dumbbell-shaped specimens. Dynamic storage modulus E' , loss modulus E'' and loss factor $\tan \delta$ were recorded on ample temperature ranges from glassy plateau to rubbery plateau, at a heating rate of $3 \text{ }^\circ\text{C}/\text{min}$, at a controlled sinusoidal strain (0.1% as maximum strain) and with a fixed frequency (1 Hz).

Moreover, the creep behaviour of silver NPs filled 3D printed specimens has been investigated by applying a constant stress (0.05 MPa) for a creep time of 10 min at several isothermal steps (temperature range from 10° to $50 \text{ }^\circ\text{C}$, temperature increment $10 \text{ }^\circ\text{C}$). Raw

Materials and methods

creep curves were used to generate a master curve at 10 °C expressed as creep compliance J_c as a function of time, according to the time-temperature superimposition (TTS) principle following the Williams-Landel-Ferry (WLF) model [137].

To predict the reduced storage modulus, the generalised Kernel equation for the reduced modulus of filled polymers was applied and a comparison with the experimental results was carried out, using the following:

$$\frac{E'}{E'_1} = \frac{1+AB\varphi_2}{1+B\Psi\varphi_2} \quad (1)$$

where E' and E'_1 are the storage moduli of the composite and of the unfilled matrix, respectively. The constant A , for spherical particles, is defined as:

$$A = \frac{7 - 5\nu}{8 - 10\nu} \quad (2)$$

being ν the Poisson's ratio. The constant B depends on the ratio between the filler and the matrix moduli, but it can be approximated to 1 for very high ratios.

Ψ is a reduced concentration term which depends on the maximum packing fraction of the particles (φ_m) according to the following definition:

$$\Psi = 1 + \frac{1-\varphi_m}{\varphi_m^2} \varphi_2 \quad (3)$$

in which φ_2 represents the filler volume fraction. To convert the percentage weight values into volume fractions, the density of the silver NPs has been taken equal to that of the bulk silver (10.49 g/cm³), while for the matrix the density was taken equal to the one of the liquid resin formulation (1.127 g/cm³).

In this work, for silver NPs, the Poisson's ratio of the matrix was taken equal to 0.5 and the maximum packing fraction of the particles φ_m was taken equal to 0.601, which is typical of the non-agglomerated packing configuration.

2.4.6 UV-Vis Spectrophotometer

A UV-Vis Spectrophotometer (Evolution 260 BIO, Thermo Fischer Scientific, Waltham, MA, USA) has been used in the characterisation of Cu NPs. UV-Vis spectroscopy can measure electronic transitions from ground state to excited state of transition metal ions solutions, and was used to try to identify the reduction of UV irradiated Cu salt solutions.

2.4.7 Durometer

The durometer gives information about the hardness of the material, it is useful for those applications that require some guaranteed standard values. It measures the penetration of the indenter inside the polymer and gives a value that can be correlated to the Shore hardness scale used to obtain the hardness value. A portable hardness tester (Affri, Induno Olona, Italy) equipped with shore A scale has been used.

2.4.8 Fourier Transform Infrared Spectroscopy - FT-IR

FTIR is a technique capable to obtain an infrared spectrum of absorption or emission of a solid, liquid or gas. An FTIR spectrometer simultaneously collects high-spectral-resolution data over a wide spectral range.

FTIR spectra were recorded on a FTIR VERTEX 70 spectrophotometer (Brucker Corporation, Billerica, MA, USA) equipped with a detector MCT Mid-Band (8000 - 600 cm⁻¹); for each sample type both the liquid formulation and the printed specimen were tested.

2.4.9 Micro computer tomography - Micro-CT

Micro computer tomography is a non-destructing technique that uses x-rays to create cross-sections of a physical object that can be used to recreate a virtual three-dimensional model.

Micro-CT scans were performed on a SkyScan 1174 v2 (Bruker, Billerica, MA, USA) at a source voltage and current of respectively 50 kV and 800 μ A, with an image pixel size of 19.6 μ m.

2.4.10 Tensile and compression tests

Tensile and compression tests can produce a lot of information on the mechanical properties of the tested material. It is possible to understand the Young's modulus, the deformation at break, the maximum stress at break, the elastic limit and other mechanical characteristic.

Tensile tests until failure were performed according to the ISO 527-2 standard and carried out by using a 2 kN load cell, at a crosshead speed of 1 mm/min, in environmental condition of temperature and relative humidity (Universal Testing Machine, TesT GmbH, Erkrath, Germany).

Compression tests until failure were carried out following the ASTM D695 – 15 standard and performed using a 100 kN load cell, at a crosshead speed of 1 mm/min, in environmental condition of temperature and relative humidity (Universal Testing Machine, Instron model 4505, Norwood MA, USA). During compression tests, electric measurements were performed with a 2-probe method, on a homemade hardware for conductivity measurements.

2.4.10.1 Data conditioning and identification of the quasi-linear region

Data collected from the Universal Testing Machine (UTM) are imported into the MATLAB environment for post-processing and synchronised with the electrical measurements coming from a custom conditioning circuit, sampled with an Analog-to-Digital Converter (ADC).

The physical sizes of the specimens are measured before the test, and no-load cross section and length are identified considering also the orientation of the sample (xy- or z-axis). For the sake of fairness, samples are considered to be broken before the effective destruction of the part under test: the specimen is considered to be broken when negative force increment higher than the bigger between 5% of the value reached or 50 N. This “50 N zone” is introduced to account for the initial transient of the instrument and possible settling disturbances occurring at the beginning of the compressive test.

2.4.10.2 Mechanical data processing

Since mechanical quantities are sampled by the UTM at constant displacement, they are resampled with a uniform time base, after the effective duration of the test is determined as stated above. This helps proper synchronisation and consistency of both mechanical and electrical data. After that, stress and strain are derived from the mechanical load (resulting from the UTM) and the absolute displacement, normalised on the *nominal* geometrical quantities.

One of the greatest challenges in characterising the tested materials is the fact that standard ASTM D695-15 [136] cannot be applied in its Fig. A1.1 because no linear region is evident in the data; moreover, also Fig. A1.2 cannot be applied, because the stress-strain experimental curve does not exhibit any concave shape. In fact, the material under test breaks in its “quasi-linear” region. This region can be defined for intermediate levels of stress: at lower displacement values the relationship is highly non-linear, due to the uneven contact

Materials and methods

surface of the sample. After that region, the samples exhibit a characteristic that is nearly linear, but with a convex shape, as with a power law with exponent α such that $1 < \alpha < 2$.

The determination of the strain in quasi-linear region is hence done as follows: stress-strain data are fitted in the last 90% portion and the intersection with strain axis is found (ϵ_0 in Figure 59). Then the error of data with respect to a linear fitting is computed and when this error goes into the 0.75-quantile, the quasi-linear strain is identified (ϵ_{ql}^m in Figure 59). The process is required because data is misrepresented by the uneven contact surface at the beginning of the test. The sum-of-square error (SSE), resulting from the fitting procedure, besides being an index of the fit quality, is also a measure of the sample non-linearity.

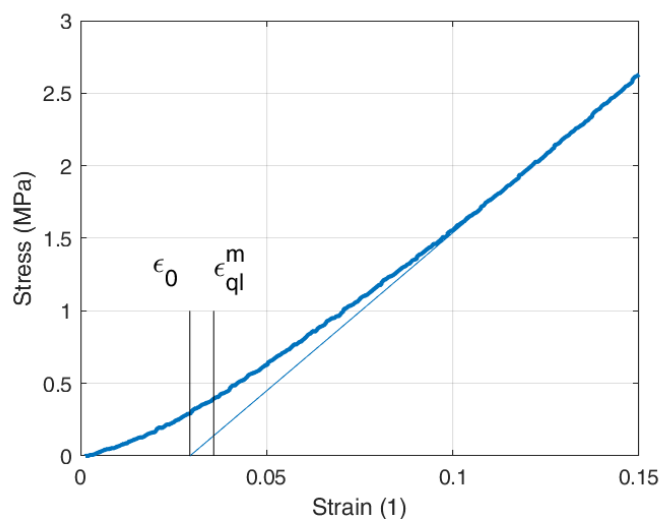


Figure 59: representative stress-strain curve of a TEGO filled sample processed through STLG. The image shows the mechanical quasi-linear strain and the process to obtain it

2.4.11 Electrical properties test systems

The electrical resistance and conduction properties of printed samples have been tested in many ways. One of the purpose in the addition of conductive nanoparticles inside a polymeric matrix is to improve electrical properties. A homemade characterisation machine has been developed for to measure the conductivity of nanocomposite materials under

Materials and methods

compression test, and the results have been checked using standard characterisation equipment.

2.4.11.1 Electrical data processing

A more complex procedure is adopted to condition the electrical information. Firstly, electrical data are truncated at the same length of the mechanical ones. Outliers are identified using a moving-median window and removed by means of linear interpolation. Electrical data, consisting of current measurements along the compression axis, are resampled and synchronised with the mechanical time series. Resistance is hence computed from current and reference voltage; conductivity curve (as a function of strain or displacement) is obtained using two different models: in one case, a constant-area model is used, in the other a constant-volume model is exploited. In the latter, the hypothesis of no barrelling is adopted, to simplify the mathematical handling of the model.

The conductivity curve resulting from the constant area model does not exhibit a flat shape, resulting in a monotonically increasing function. A single conductivity value can be obtained by averaging the constant-volume conductivity data, on the strain range from 40% to 90%. The experience shows that in this range the conductivity-strain curve is almost constant, proving the correctness of this model and negating the constant-area one. This unique value of conductivity is used to compute an “ideal” conductivity at the input strain values to cross-check for model accuracy. The quasi-linear strain threshold from electrical data is computed from one-crossing (with a 2% tolerance) of the normalised area obtained from raw conductivity data in the constant-volume model (ε_{ql}^e in Figure 60).

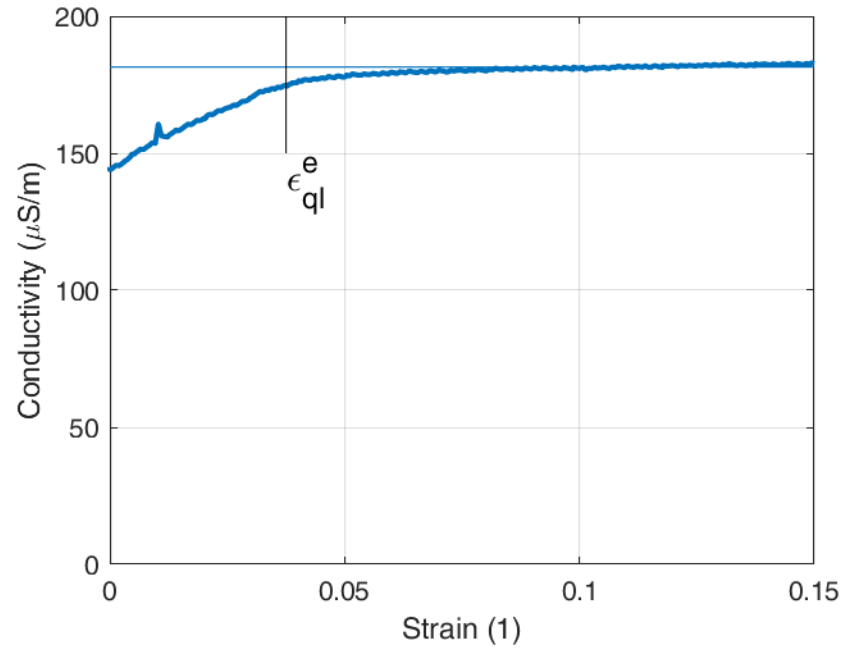


Figure 60: representative conductivity-strain curve of a TEGO filled sample processed through STLG. The image shows the electrical quasi-linear strain and the process to obtain it, as well as the unique value of conductivity.

2.4.11.2 Insulation tester

Megger MIT230 (Megger Group Limited, Dover, UK) insulation tester have been used just to confirm the electrical measurement obtained with the 2-probe homemade conductivity tester.

2.4.11.1 Homemade dynamic resistivity/conductivity tester

This is a 2-probe method, homemade hardware developed to conduct studies on the electrical properties of solid materials or structures under the effect of mechanical compression. The design of this equipment consists of a two-point ohmmeter effective for materials with high electrical resistance.

The module consists of 4 components, supports with electrical contacts adapted to the 4505 universal test system, an adjustable DC voltage source HY3003D, a micro-ammeter

Materials and methods

and a Genuino 101 microcontroller. The components must be assembled as shown in Figure 61.

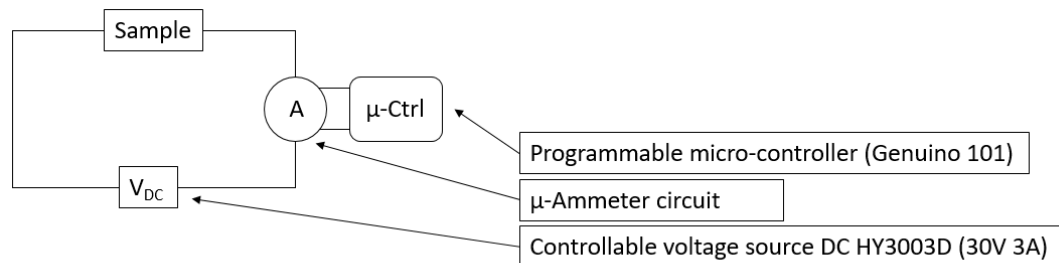


Figure 61: schematic representation of the circuit for the experimental setup

The electrical contact with the sample is made with customised supports. The two pieces of 3D printed ABS must be mounted on the compression plates of the 4505 as shown in Figure 62 and secured with screws. On each support, there must be a copper plate to make the electrical contact with the wires and the remaining instruments in the assembly.

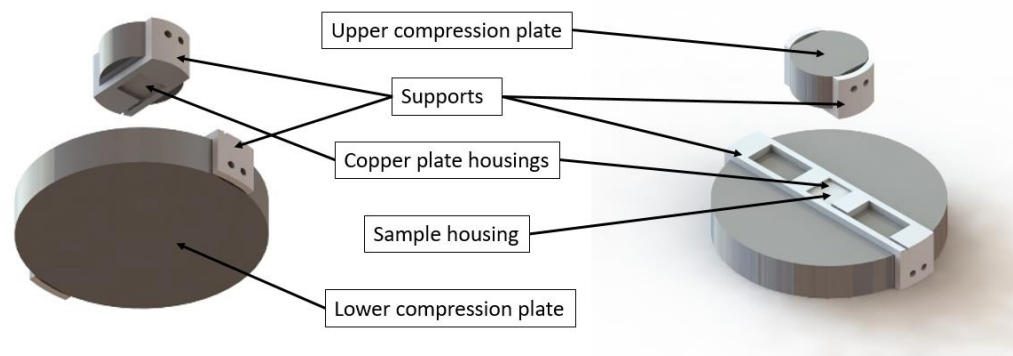


Figure 62: model of the assembly to the compression plates of the holders for the electrical testing.

The micro-ammeter is a circuit specially prepared for this application. It integrates a series of operational amplifiers to allow an output signal with the voltage proportional to the current passing through the circuit. The instrument has 5 positions with different amplifications, the output has the order of 1 V when the current is 1 mA, 100 μ A, 10 μ A, 1

Materials and methods

μA and 100 nA for positions 1,2,3,4 and 5, respectively. The Genuino 101 microcontroller is used as a voltmeter to measure the output voltage of the ammeter and record it on the computer. The data available on the microcontroller serial port is read by the parallax excel PLX-DAQ macro.

The ammeter circuit is shown in Figure 63 and consists of an amplification circuit and a low pass filter circuit. The filter is necessary because the measured currents are low and are susceptible to fluctuations in the electrical network. The switch used has n positions but only 5 are used, the rest is open circuit and the voltage at the output when the switch is in one of these positions is sufficient to saturate the microcontroller used as a voltmeter.

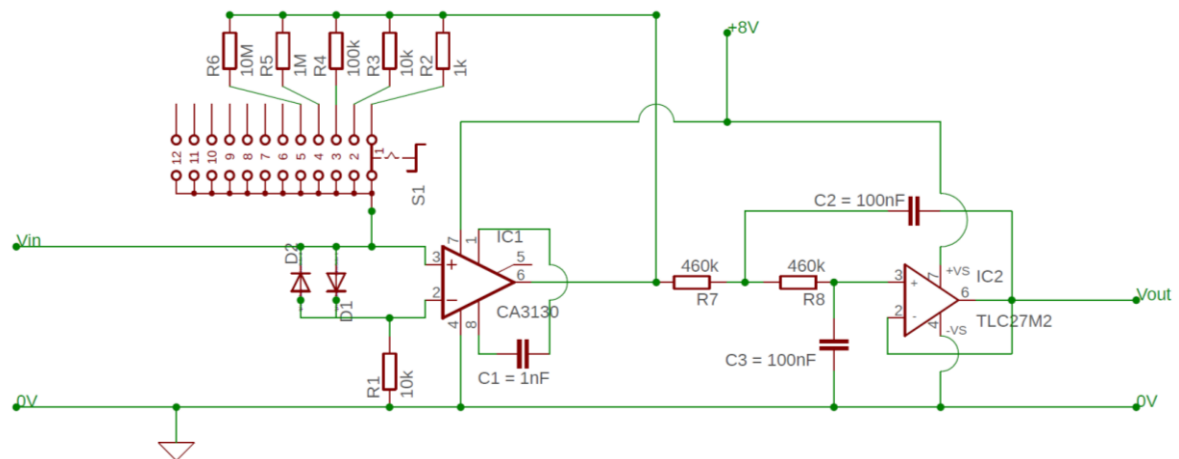


Figure 63: schematic representation of the circuit used.

3 Results and discussion

This chapter organises and presents the results obtained in the original research articles published (and to be published) during this doctorate, titled: “Special resins for stereolithography: In situ generation of silver nanoparticles” [2], “Acrylic resins for stereolithography 3D printing with tuneable thermo-mechanical properties” [to be published], “Development and characterisation of polymer-silver nanocomposites: a comparative study on the technological process between SLA and DLP” [to be published], “Development and characterisation of polymer-graphene nanocomposites for Vat Photopolymerisation additive manufacturing” [to be published].. The papers were correlated with additional material from the preliminary tests and unpublished work, as well as with the description of the work that brought to the presentation of a patent.

3.1 Preliminary tests under UV lamp

Around 120 different compositions and combinations were tried in preliminary polymerisation tests under UV lamp. These tests were conducted under UV lamp with a reduced amount of resin and fillers to gain information on the parameters of the formulation, optimise the composition and verify the reactivity of the system without wasting too much material and time. Once a formulation gave good results under UV lamp it was tested also on the VP systems and the subsequent characterisations were done, since the behaviour under UV lamp and under a laser scanning system is clearly different.

3.2 Unfilled SLA samples: PEGDA 250-700 – thermo-mechanical properties modulation

This paragraph is based upon the research article “Acrylic resins for stereolithography 3D printing with tuneable thermo-mechanical properties”. The work aims to demonstrate the possibility to tune the thermo-mechanical properties of 3D printed objects

obtained using a SLA. Two acrylate oligomers, with the same polyethyleneglycol-based chemical structure but different molecular weight, were used as starting materials in order to match the requirements of different applications. A post-print treatment was set up for all the samples to obtain a complete cross-linking degree.

3.2.1 Results - PEGDA 250-700

3.2.1.1 DSC

Figure 64 reports the DSC thermograms of PEGDA A sample, chosen as representative, respectively before (coded NT) and after (coded UV) the UV post-treatment. PEGDA A NT thermogram reveals a broad exothermic peak in the range 120-170 °C which can be associated with a post-curing process. After the UV treatment, no exothermic peak is evident.

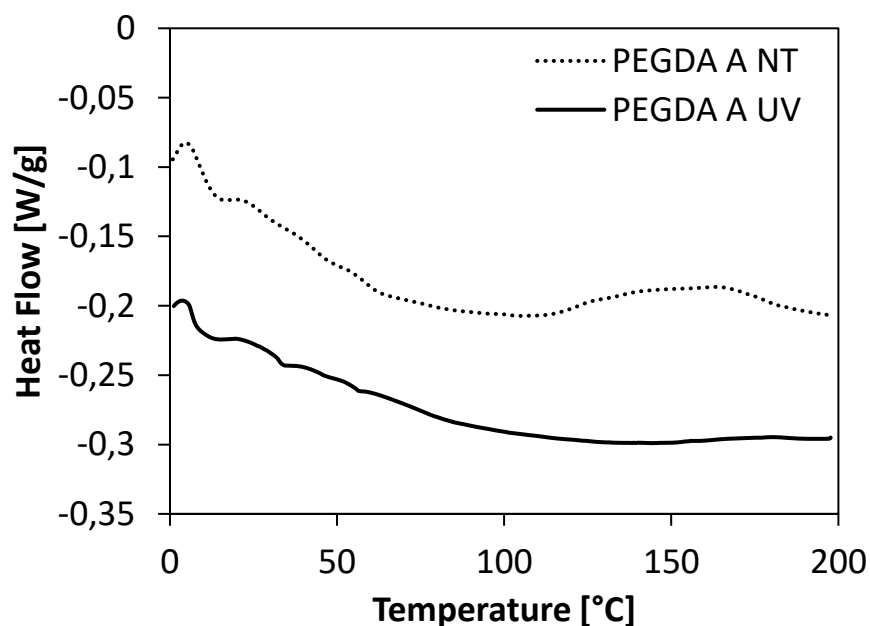


Figure 64: differential scanning calorimetry (DSC) thermogram (exothermic up) of PEGDA 250 before (PEGDA A NT) and after (PEGDA A UV) post-treatment. Sample PEGDA A is shown as representative.

3.2.1.2 FTIR

The degree of curing is estimated with the comparison of FTIR spectra between liquid and cured formulations after UV treatment. Figure 65 shows the two spectra of PEGDA 700 formulation, chosen as representative, before the printing process (a) and after the post-treatment (b): the disappearing of a peak at around 3100-3000 cm^{-1} can be observed. This peak is connected to the stretching of the =C-H bond in the methylene group [138]. Since the C=C bond is only present in the liquid acrylic monomers but it is substituted by a single C-C bond after the crosslinking, this particular =C-H bond stretching can be used as a reference signal for the residual presence of unreacted acrylic groups. The degree of cure, estimated by the ratio of the peak areas before SLA printing and after post-processing, was found to be always higher than 97% for all the formulations.

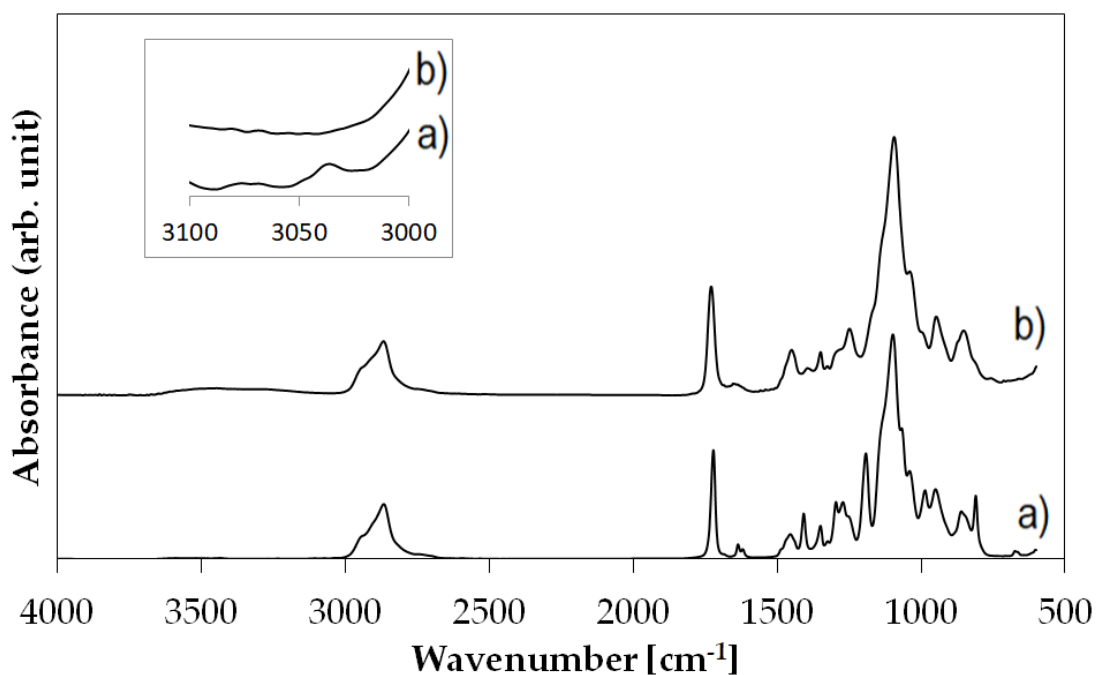


Figure 65: Fourier transform infrared spectra (FTIR) of PEGDA 700 before (a) and after (b) SLA printing and UV treatment. Only the PEGDA 700 spectra are reported here as representative of the other formulations that exhibited the same behaviour.

3.2.1.3 Tensile characterisation

The only thing that differentiates the five samples is the mean molecular weight of the formulations. This difference brings to a change in the mechanical properties of the printed objects because a decrease in the oligomer chain length generates higher cross-linking density, stiffness, and ultimate tensile strength (UTS), while longer chain lengths bring to more flexible materials. These differences can be seen from Figure 66 in which a representative stress-strain curve for each set of samples is displayed along with the others.

A more precise and detailed overview is available considering

Table 9, in which it is clear the increase in UTS and in E as the average molecular weight decreases, while no clear trend can be determined for the elongation at break.

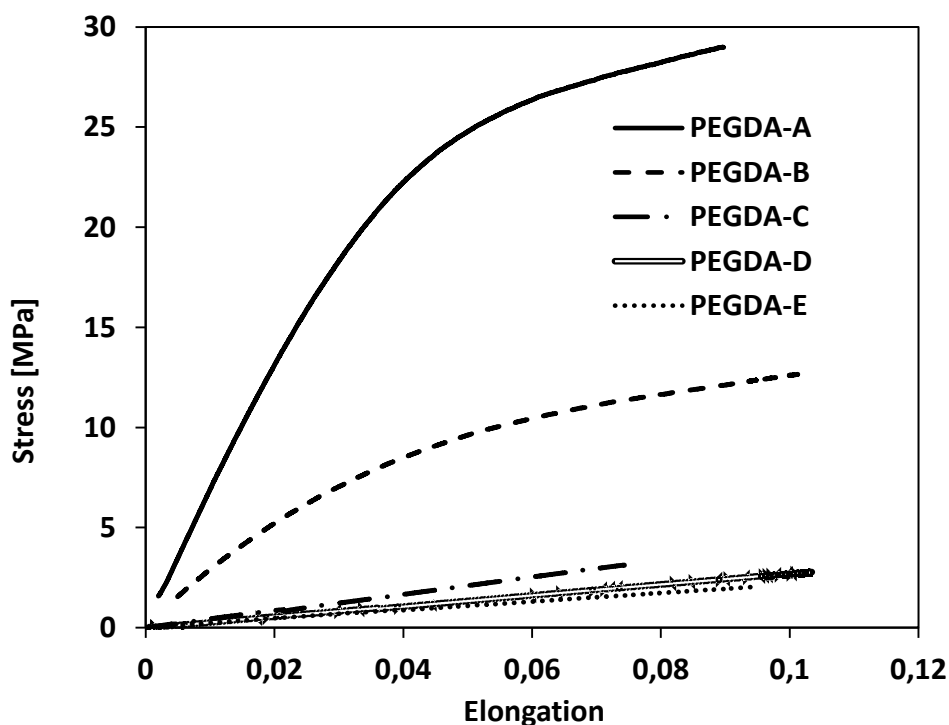


Figure 66: Representative stress-strain diagram with each formulation displayed

Table 9: mean values and standard deviations of tensile strength, tensile strain at break and Young's modulus

	UTS (MPa)	Tensile strain at break	E: Young's modulus (MPa)
PEGDA-A	30±2	0.09±0.01	710±40
PEGDA-B	12.6±0.2	0.08±0.01	340±30
PEGDA-C	3.0±0.1	0.072±0.003	41±6
PEGDA-D	2.6±1	0.09±0.05	27±6
PEGDA-E	1.5±0.5	0.07±0.02	21.0±4

3.2.1.4 DMTA characterisation

DMTA analyses results are shown from Figure 67 to Figure 69 while numerical details are reported in Table 10.

With the decrease of the average molecular weight of the oligomer formulation, the storage modulus, E' , has higher values in the glassy state at low temperatures as well as in the rubbery plateau after glass transition temperature (T_g). Furthermore, the rubbery plateau is reached at higher temperature (from around -20°C to more than 80°C) for lower crosslinking density (Figure 67).

T_g is evaluated as the temperature corresponding to the peak value of $\text{Tan } \delta$. There is a clear tendency for a broadening of the peak, a decrease of its maximum value and an increase in the T_g (it ranges from -27.5 to 61.9°C) when the crosslinking density decreases (Figure 68).

The same trend can be observed for the loss modulus, a decrease and broadening of the peak with an increase of the temperature of its value at lower crosslinking density (Figure 69). This behaviour is due to the molecular structure of the monomer. Longer chains in the base monomer allow better and more ample movements, activated at lower temperatures. Less energy is required to start the chain movements, so T_g is lower. On the contrary, shorter monomers increase the cross-linking density [139,140] impeding the segmental motion of the polymeric chains, having the same effect of a filler [135,141–146].

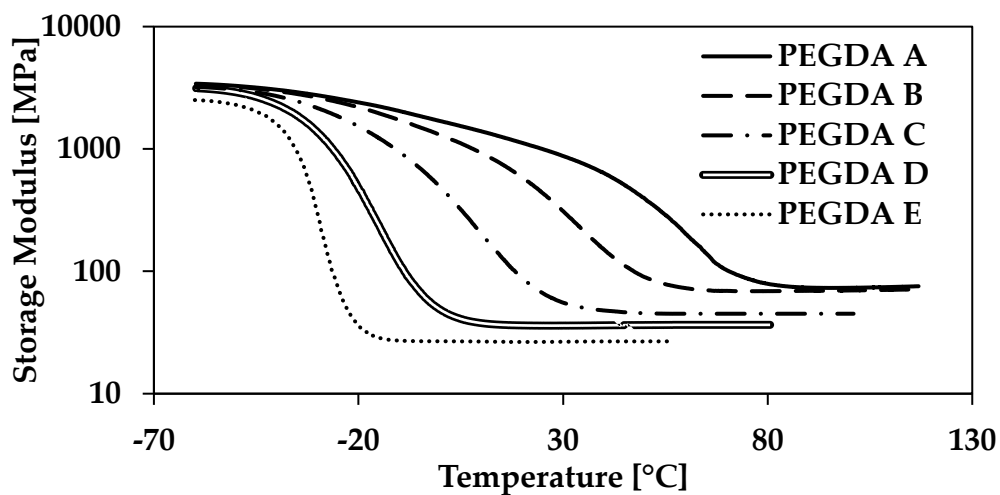


Figure 67: dynamic-mechanical thermal analysis (DMTA) thermograms of the storage modulus (E') of the five different formulations.

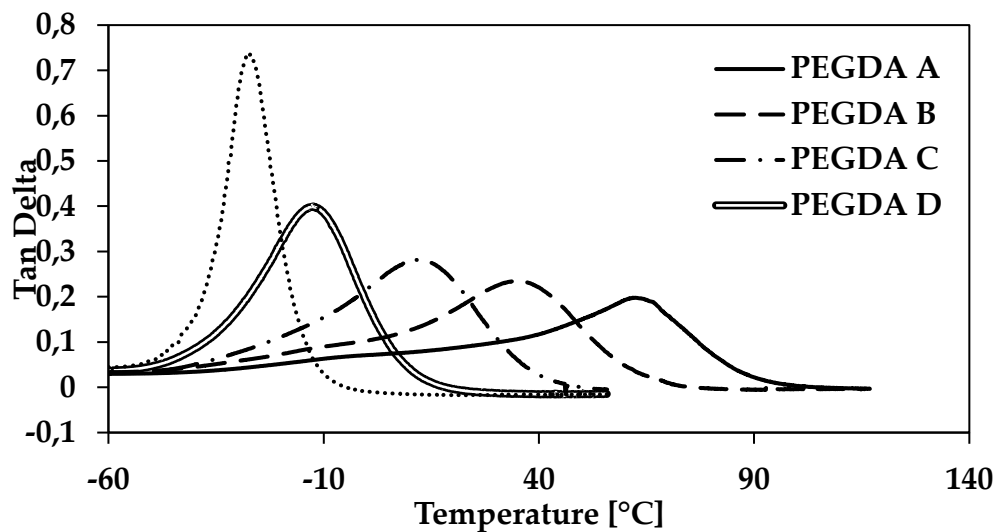


Figure 68: dynamic-mechanical thermal analysis (DMTA) thermograms of the Tan Delta of the five different formulations.

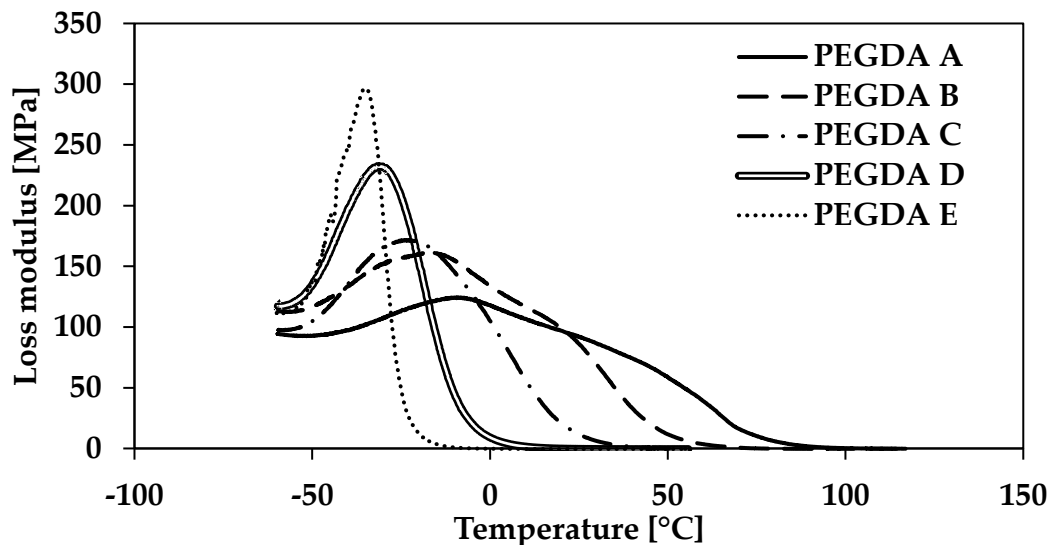


Figure 69: dynamic-mechanical thermal analysis (DMTA) thermograms of the loss modulus (E'') of the five different formulations.

Table 10: characteristic temperatures and moduli of the different printed formulations, respectively E' and E'' at 25 °C, T_g at $\text{Tan } \delta$ maximum.

	E' at 25°C (MPa)	T_g [°C]	$\text{Tan } \delta$ maximum
PEGDA-A	998	62	0.20
PEGDA-B	437	35	0.23
PEGDA-C	66	12	0.28
PEGDA-D	36	-13	0.40
PEGDA-E	26	-28	0.73

3.2.2 Discussion - PEGDA 250-700

Since the DSC thermograms (Figure 64) show a clear exothermic peak, a small amount of unreacted acrylic groups is probably still present after the SLA process, but not after the UV post-treatment. Another factor that confirms this view is the strong reduction, always higher than 97%, of methylene group stretching, only present in the FTIR spectra of the liquid monomers but not in the UV post-treated crosslinked specimens (Figure 65).

Results and discussion

This complete curing of the liquid resin only after post-processing is a common thing for SLA, where a thermal and/or UV post-treatment is usually needed.

Interestingly, the mechanical properties show a strong increase in stiffness and tensile strength only when the formulation contains more than 50% of PEGDA 250, while at lower average molecular weight the flexibilising effect of the PEGDA 700 is prevalent. Moreover, it can be noted that all these materials show a relatively low elongation at break value, floating around 8%, presumably due to thermoset nature of the cured resins.

On the other hand, the thermo-mechanical properties present a more equilibrate shifting between the extreme positions of the pure oligomers. From DMTA analysis, it is clear that the average molecular weight of the mixture is a good way to control the modulus and the glass transition of the crosslinked polymer. The T_g ranges from over 60°C with pure PEGDA 250, to almost -30°C with pure PEGDA 700 and E' can be varied between 25 to 1000 MPa at 25 ° C, depending on the application requirements.

Not many ways to modify the thermo-mechanical properties of a material, without adding any additive or filler, has been presented yet in literature. Pashneh-Tala et al. in [147] suggest to act on the degree of acrylation to control and tune the mechanical properties. Stampfl et al. in [23] propose to change the strength and elastic modulus in the product using a different monomer or acting on the degree of crosslinking. The method here proposed is even more simple and fast, acting only on the mean composition of the polymeric blend obtained by mixing two different weight of a single oligomer instead of producing a single molecular weight monomer or having to select a different monomer for any specific application.

Another factor that contributes to the lean method here developed to modify the thermo-mechanical properties, is the use of a simple and low cost unmodified commercial desktop SLA printer.

This work can be further developed functionalising this tailorable base material, that could act as a matrix for a full range of fillers to build composite materials that can take advantage of a matrix with tuneable flexibility. Examples of composites that uses a PEGDA matrix can be found in [81,103,148,149].

3.2.3 Conclusions - PEGDA 250-700

This work demonstrates that it is possible to use an SLA printer to process a single material with different molecular weights to control the thermo-mechanical properties of the 3D printed objects. The possibility to choose the properties of the material makes that material potentially suitable for a wide spectrum of applications.

DSC and IR characterisations demonstrated the complete curing of the materials after printing and post-process treatment. While the tensile tests and DMTA measurements showed how it is possible to modify the mechanical and thermo-mechanical properties by changing exclusively the relative content of the two starting acrylate oligomers in the final formulation.

The use of two commercial acrylate oligomers as starting materials, an unmodified commercial SLA printer, the relatively limited time needed to print and the leanness of post-processing steps, make the process simple and easy. Furthermore, the material in particular and the process in general, can be used as a base to build acrylate-based materials with different properties in a tailorable range.

3.2.4 Application (ceramic industry patent)

The work carried out on modulation of mechanical properties of polymers processable via AM, found application in the development of a formulation for the ceramic sector. The application consists in the VP fabrication of the polymeric pads (Figure 70) used for the surface structuring of ceramic tiles green (Figure 71 and Figure 72). The method currently adopted consists in the CNC machining of stainless steel negative matrixes that give the form to a rubber thermoset. This rubber must be vulcanised in an oven to get the desired shape from the metallic matrix. The process is longer and more expensive, AM can reduce the time required for the fabrication of the pads, eliminating the step of the negative metallic matrix, giving also the benefit of an infinite choice of surfaces not limited by a single physical matrix but only by different CAD models.

Results and discussion

This work brought to the presentation of a patent request under the name of “METODO E MATERIALI PER LA FABBRICAZIONE DI TAMPONI PER L’INDUSTRIA CERAMICA” (method and materials for the fabrication of pads for the ceramic industry). Request number: it 102018000008679.

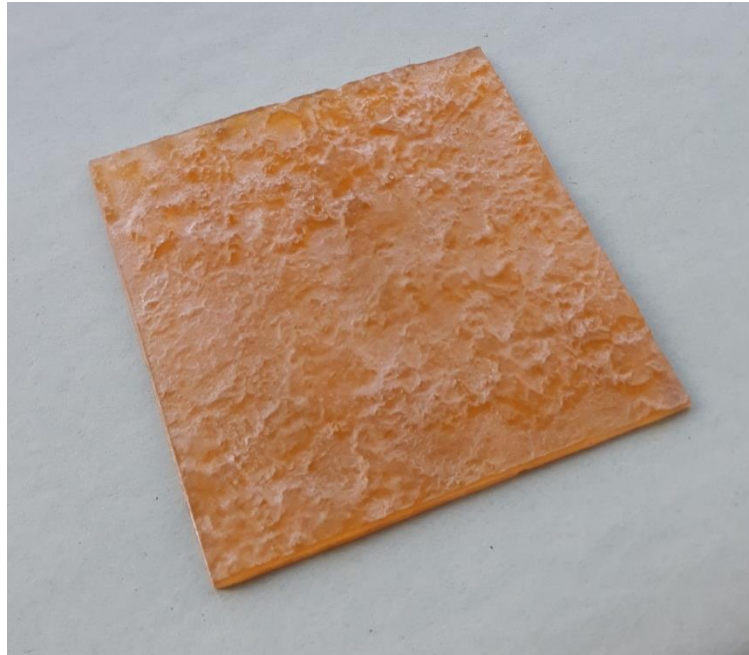


Figure 70: the printed polymeric pad with the surface to impress on the ceramic powders

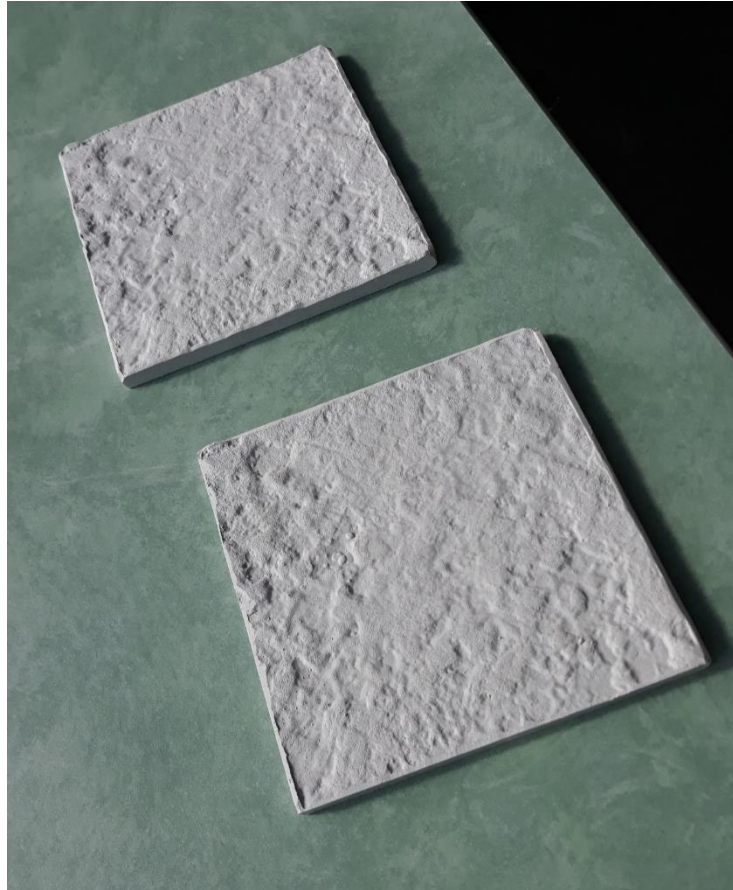


Figure 71: the pressed ceramic powder forming a green tile

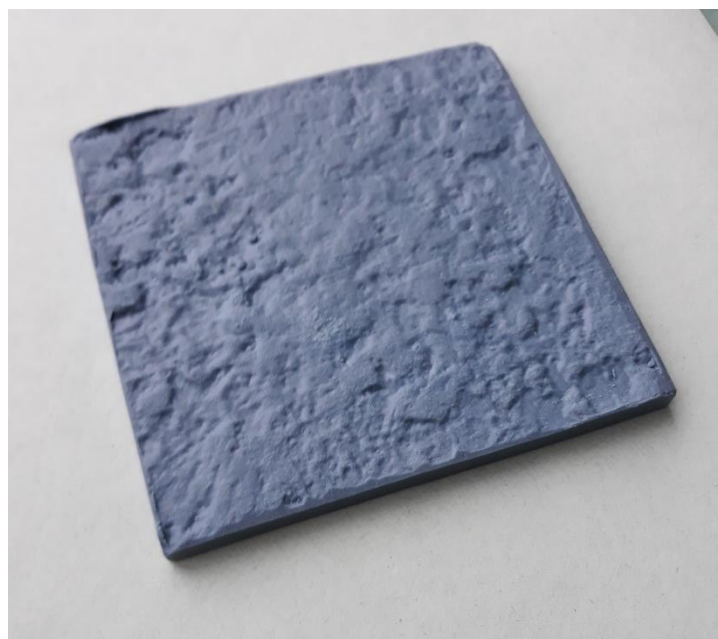


Figure 72: another example of pressed ceramic powder forming a green tile

3.3 Filled samples

Additive manufacturing of polymers has a lot of potential and serves many applications, but the fields of use of these systems can be enormously increased by the addition of fillers to the formulations. The enhancement of pristine matrix properties or the addition of completely new ones are obtainable through the addition of functional fillers.

3.3.1 SLA - AgNPs – simultaneous photopolymerisation and *in situ* photoreduction of AgNPs

This paragraph is based upon the original research article “Special Resins for Stereolithography: In Situ Generation of Silver Nanoparticles” published on Polymers [2].

3.3.1.1 Results

3.3.1.1.1 XRD analysis

XRD patterns of “AgAcr $x\%$ ” and “AgMAcr 1%” samples reported in Figure 73 confirm the transformation of silver ions to metallic silver. It is also important to underline the absence of peaks related to silver oxide (main peak at 32.9°). Therefore, the peak intensity decreases from “AgAcr 2%” to “AgAcr 0.5%” sample, according to the variation of the nanoparticle amount in the analysed samples. Moreover, the evident peak broadening is indicative of the nanometric dimension of the coherent diffraction domains.

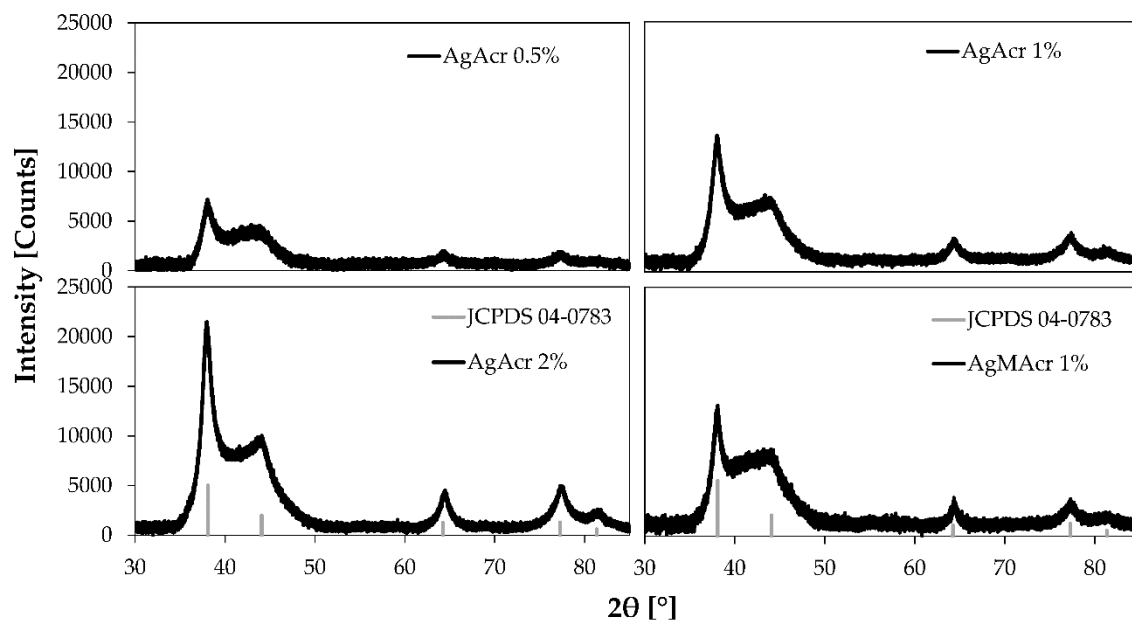


Figure 73: X-ray diffraction (XRD) diffraction pattern of 3D printed materials containing different amount of AgNPs from AgAcr and AgMAcr as precursors.

3.3.1.1.2 TEM micrographs

Typical TEM micrographs of unfilled and filled printed samples are reported in Figure 74.

TEM micrographs show that, compared to the unfilled sample, AgNPs can be observed in all filled systems, regardless of the initial load and type of used AgNPs precursor. AgNPs present an almost spherical geometry with a narrow size distribution. The measured average dimensions are 9 ± 2 , 13 ± 3 , and 11 ± 2 nm in “AgAcr 1%”, “AgAcr 2%” and “AgMAcr 1%” samples, respectively.

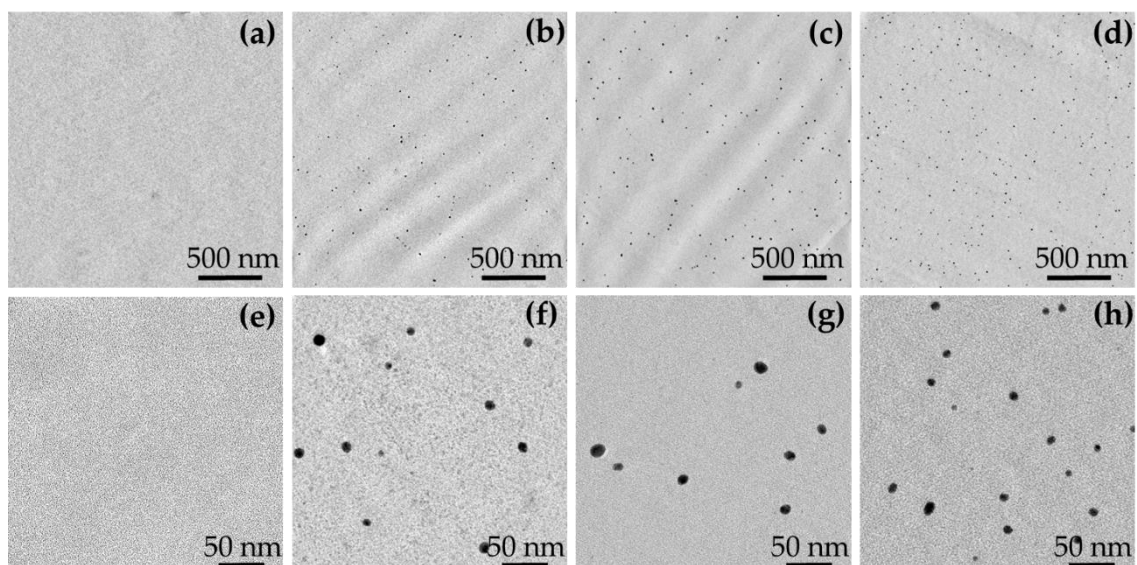


Figure 74: Transmission electron microscopy (TEM) micrographs at two different magnifications of “Unfilled” (a,e); “AgAcr 1%” (b,f); “AgAcr 2%” (c,g); and “AgMAcr 1%” (d,h); as representative.

3.3.1.1.3 DSC Analysis

Typical DSC thermograms of unfilled and filled resins, before and after a post-curing thermal treatment, are reported in Figure 75.

DSC thermogram of unfilled resins “Unfilled NT I” is characterised by the absence of any exothermic peak indicating a complete resin conversion on the 3D printed specimens without the necessity of any post-curing processes. On the contrary, all filled resins, characterised immediately after 3D printing (NT I samples), exhibit clear exothermic peaks attributable to the presence of unreacted carbon-carbon double bonds (C=C). These peaks completely disappear in the second heating scan (NT II samples) and are absent in the thermally post-cured samples (TT I samples).

Results and discussion

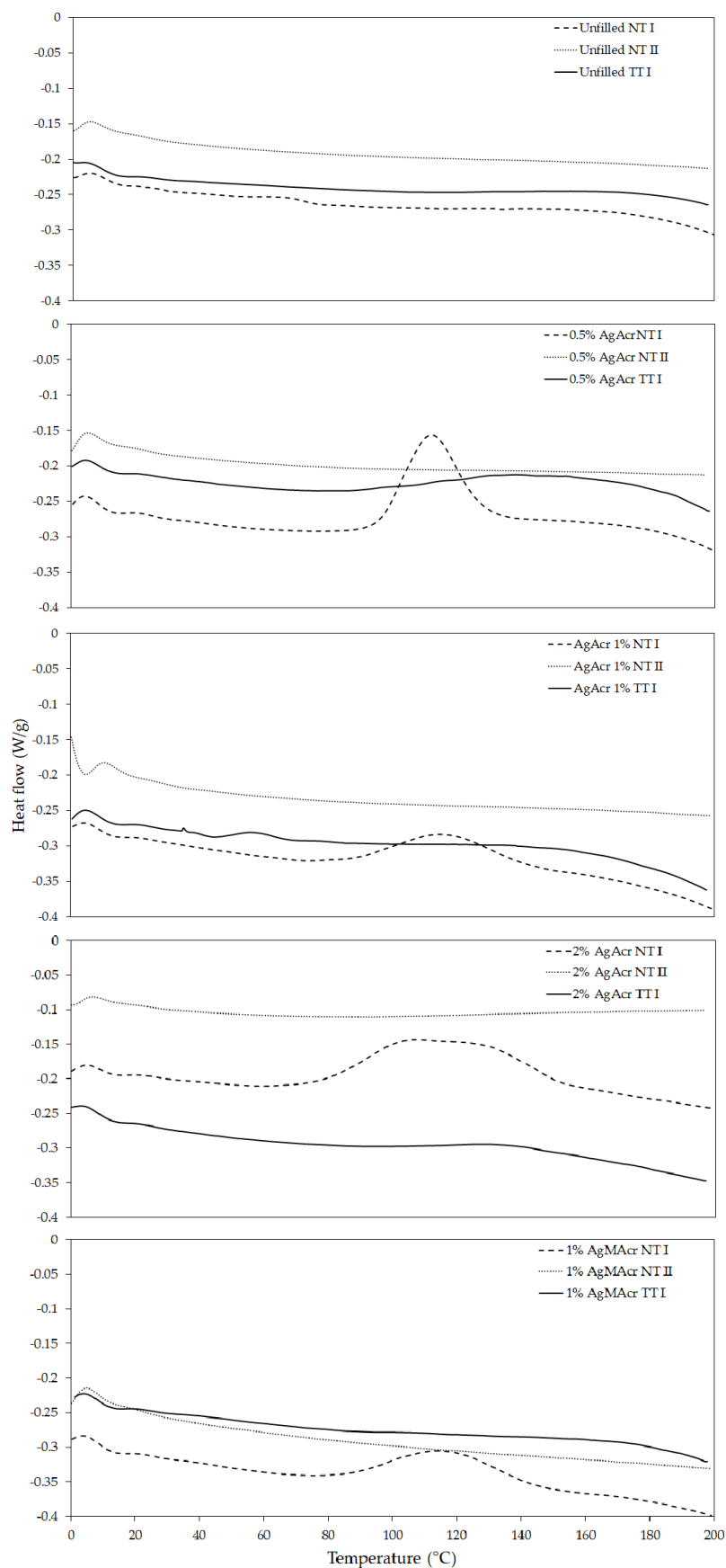


Figure 75: Differential scanning calorimetry (DSC) thermograms (exo up) of “Unfilled”, “AgAcr x%” and “AgAcr 1%” (TT: after thermal treatment; NT: no thermal treatment; I: first heating scan, II: second heating scan).

3.3.1.1.4 Tensile properties

Representative stress-strain curves of filled and unfilled resins are reported in Figure 76. The corresponding tensile properties of the 3D printed specimens are reported in Table 11.

Young's modulus values systematically increase by increasing the AgNPs concentration from a minimum of 68 MPa for "Unfilled" sample to a maximum of 153 MPa for "AgMAcr 1%" sample. Strength values follow the same trend also, with a significant maximum value of 5.0 MPa in the case of "AgAcr 2%" sample.

Strain at break values systematically decrease by increasing the AgNPs concentration from a maximum of 6.1% for "Unfilled" sample to a minimum of 2.4% for "AgMAcr 1%" sample.

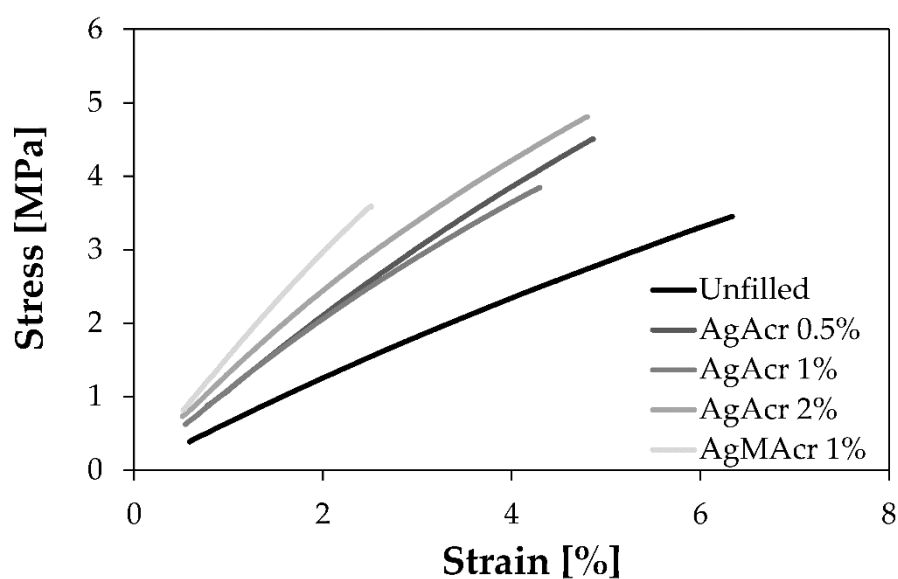


Figure 76: Representative stress-strain diagram for Ag-filled and unfilled samples.

Results and discussion

Table 11: Tensile properties of 3D printed specimens (E_t : Young's modulus; σ_M : tensile strength; ϵ_B : tensile strain at break, according to ISO 527 technical standard).

Sample	E_t (MPa)	σ_M (MPa)	ϵ_B (%)
Unfilled	68 ± 2	3.4 ± 0.3	6.1 ± 0.7
AgAcr 0.5%	111 ± 3	4.3 ± 0.4	4.8 ± 0.6
AgAcr 1%	113 ± 8	4.0 ± 0.4	4.0 ± 0.1
AgAcr 2%	142 ± 8	5.0 ± 0.8	4.7 ± 0.9
AgMAcr 1%	153 ± 5	3.4 ± 0.3	2.4 ± 0.2

3.3.1.1.5 DMTA properties

The results obtained by dynamic-mechanical analysis are reported in Table 2 in terms of glass transition temperature (T_{gDMTA} , determined from the maximum of $\tan\delta$ curve) and storage modulus measured at 60 °C.

T_{gDMTA} values systematically increase by increasing the AgNPs concentration from a minimum of 0.7 °C for "Unfilled" sample to a maximum of 11.8 °C for "AgAcr 2%" sample. Also, storage modulus values evaluated above T_{gDMTA} follow a similar trend ranging from a minimum of 65 MPa for "Unfilled" sample to a maximum of 140 MPa for "AgMAcr 1%" sample.

A comparison between the reduced storage modulus obtained from the experimental results and from predictive equations is reported in Figure 77 by applying the generalised Kernel equation for the reduced modulus of filled polymers [150].

The figure clearly shows an evident increment of the relative storage modulus (E/E_1') in the experimental results with respect to the prediction of the Kernel equation. This increment can be attributed to an action of the filler as a cross-linking agent, besides his action of pure rigid particle reinforcement.

Results and discussion

Table 12: Glass transition temperature (T_{gDMTA} , evaluated as temperature value corresponding to $\tan\delta$ peak) and storage modulus at 60 °C values for all the printed specimens, from DMTA analyses.

Sample	T_{gDMTA} (°C)	E' at 60 °C (MPa)
Unfilled	0.7	65
AgAcr 0.5%	4.9	87
AgAcr 1%	5.1	97
AgAcr 2%	11.8	130
AgMAcr 1%	10.5	140

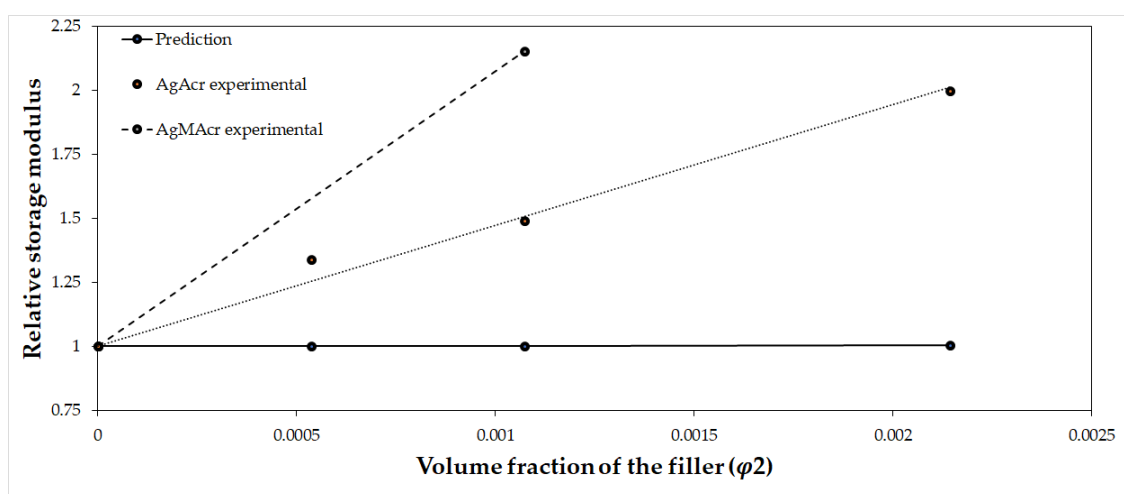


Figure 77: Relative storage modulus as a function of AgNPs volume fraction. A comparison between predicted and experimental values for the AgAcr filled series.

3.3.1.1.6 Creep Properties

Creep data (compliance as a function of temperature) obtained at several isothermal conditions ranging from 10 to 85 °C were elaborated by applying the time-temperature superimposition principle in order to get information on the creep behaviour of the investigated materials in a time scale much higher than the experimentally accessible one. A portion of the obtained master curves at the reference temperature of 10 °C is reported in Figure 78.

All compliance values were in the range of 10^{-8} Pa⁻¹ but there was a clear difference between filled and unfilled resins notwithstanding a similar slope of the curves. Once again, the materials containing in situ generated AgNPs presented a more elastic behaviour here represented in terms of creep resistance.

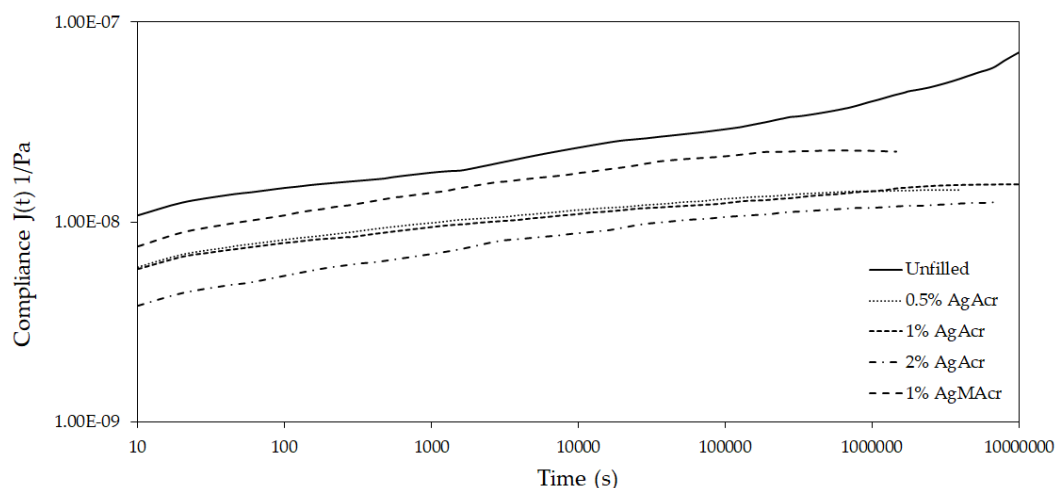


Figure 78: Master curves of compliance as a function of time at the reference temperature of 10 °C for “Unfilled”, “AgAcr x%”, and “AgMAcr 1%” samples.

3.3.1.2 Discussion

XRD analysis confirmed the conversion of silver cations deriving from soluble silver salts to metallic silver thanks to the occurrence of a reduction process attributable to both UV radiation (from SLA printer) and presence of radicals, formed after dissociation of photo-initiator. This is a very important result considering that similar systems processed with an alternative technology such as DLP evidenced the necessity to a UV-based post-curing step to generate AgNPs [89,103]. From this point of view, the power (light intensity) of the UV radiation used in SLA process was high enough to activate the chemical reduction processes to in situ generate AgNPs during the 3D printing step, contrary to what observed by using a different additive manufacturing technology (i.e. DLP) characterised by a less intensive radiation.

TEM analysis showed that the *in situ* formation of AgNPs during 3D printing allowed to optimise the dispersion and distribution of the nanofillers within the polymer matrix, avoiding problems related to the aggregation phenomena usually observed in the alternative *ex situ* preparative approaches.

DSC analysis indicated an uncomplete polymerisation reaction in the case of filled resins, i.e. in the presence of silver salts as AgNPs precursors. Presumably, two different

Results and discussion

phenomena can contribute to a conversion of carbon-carbon double bonds lower than 100%. First of all, the *in situ* generation of AgNPs converts the materials from a substantially homogeneous system to a bi-phasic heterogeneous one with the two phases having different refractive indexes, which in turn could lead to light scattering phenomena with a decrease of photo-polymerisation reaction efficiency. Secondly, the presence of rigid AgNPs in the polymer matrix is also expected to increase the rigidity and the glass transition temperature of the material and an earlier vitrification could occur with a stop of the chemical reactions due to limitation in the diffusion phenomena within a glassy matrix.

The increment in Young's modulus, due to the presence of a rigid filler, is an expected result due to hydrodynamic effect deriving from the inclusion of rigid particles in a less rigid polymer matrix. On the other hand, data indicates that the cross-linking density, which in turn dominates the modulus value above T_g , was not negatively affected by the *in situ* generation of AgNPs and related by-products formation. Moreover, the use of silver salts with counter-anions which can react directly with the acrylic monomers during the formation of the polymer network, can further stabilise the final system, limiting the formation of extractable by-products.

In addition to the significant increment of Young's modulus evidenced for all the filled samples (with a remarkable maximum value of 153 MPa for "AgMAcr 1%"), it is noteworthy also the increment of strength in the case of "AgAcr x%" series with respect to the unfilled reference resin (with a maximum value of 5.0 MPa with respect to 3.4 MPa). This behaviour is quite unexpected considering that strength usually decreases by increasing the filler content in the case of micro-composites. Conversely, in the present case a positive contribution can be considered as deriving by both the nanometric size of the filler combined with an enhanced particle/matrix interfacial adhesion according to other similar evidences reported in literature [151]. In this case, the interactions at the nanoparticle-polymer interface can benefit from the presence of carboxylate groups present in the polymeric network and deriving from the counter-anion of the starting salt. In fact, the acrylate and methacrylate groups are characterised by the co-existence of alkenyl and carboxylic functionalities in the same molecule. The alkenyl functionality has the possibility to react with the acrylic monomers, becoming part of the polymeric structure. This behaviour determines the formation of carboxylic pendants, scattered along the polymer chain, which can coordinate

the surface of the nanoparticles, improving the interactions at the interface between AgNPs and polymer.

As expected, the presence of a high-modulus filler resulted in a decrement of strain at break for all the filled resins, even if the loss in strain at break was relatively limited, with respect to the reference value of 6.1% for unfilled resin.

In accordance to quasi-static tensile properties above reported, also DMTA and creep data indicated a significant increment of rigidity, proportional to the amount of AgNPs as indicated by both glass transition temperature, storage modulus and compliance values. The comparison between experimental and predicted storage modulus values further supported the presence of an enhanced interfacial AgNPs-polymer adhesion, as already evidenced in previous papers [141,142,152].

3.3.1.3 Conclusions

This work demonstrates that the SLA process can simultaneously reduce a silver salt to *in situ* generated, well dispersed and distributed AgNPs while polymerising the liquid monomer into a solid matrix. Thanks to the selection of silver salts having reactive counter-ions, such as acrylate and methacrylate, the obtained nanocomposite material is homogeneous and without extractable by-products. In fact, the reactive counter-ions can become part of the polymeric structure and stabilise the nanoparticle-polymer interfacial interactions. The absence of by-products release, the presence of AgNPs with good dispersion and distribution, the freedom and precision allowed in the fabrication by the SLA process, are all factors that can promote this approach for the realisation of useful and valid nanocomposite materials applicable to various sectors ranging from medical and healthcare, to food packaging.

3.3.2 STLG – Ag, graphite and TEGO composites

This paragraph is based upon the work done at the CDRSP research centre of Polytechnic institute of Leiria (Portugal).

In this work, a DLP based STLG prototype machine was used to 3D print compression test specimens used for all the subsequent mechanical and functional characterisations.

The work was oriented to the realisation of silver salt *in situ* reduction with a DLP based technique operating with visible light and IR radiation, and to the enhancement of the electrical conduction properties of the composites obtained not only with the addition of silver but also with carbon based fillers such as micrometric graphite and nanostructured TEGO. A scheme of the expected reactions occurring during the printing step is reported in Figure 79.

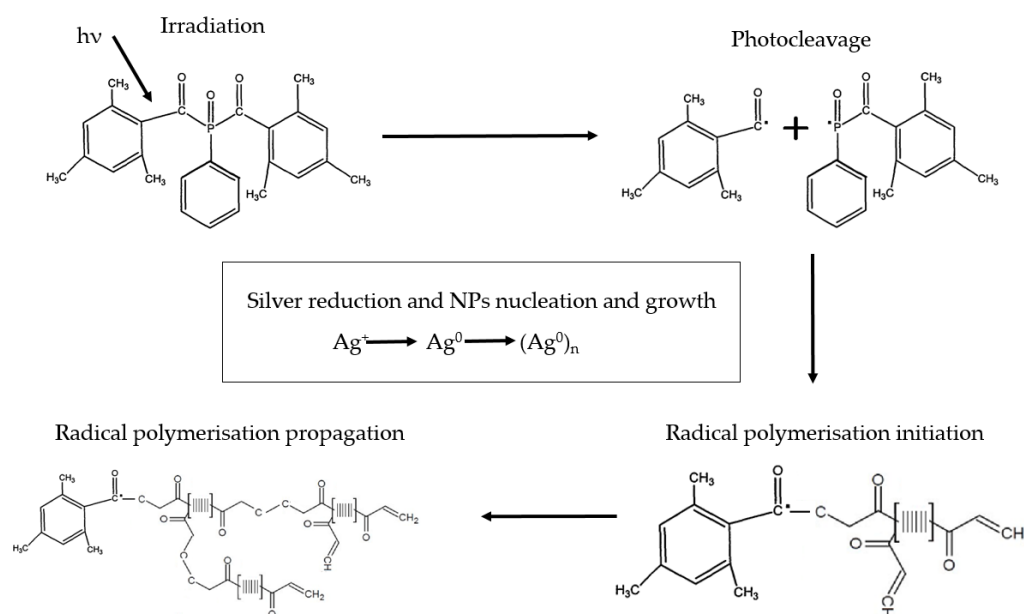


Figure 79: expected reactions during STLG 3D printing process, photodegradation of the photoinitiator and radical polymerisation initiation and propagation. In the central box, the silver ions reduction, nucleation and growth.

3.3.2.1 *Results (and discussion)*

3.3.2.1.1 DSC

The DSC thermograms (Figure 80) of all the samples are characterised by the absence of any clear exothermic peak, and no strong difference between first and second heating scans. This behaviour indicates a complete resin conversion on the 3D printed specimens within the SLA process, that avoids the necessity of any post-curing treatment. This total conversion of the resin can be due to the infrared irradiation over the resin during the printing steps that allows a resin preheat, fostering the reactivity and giving to the printed object a contextual thermal treatment.

Results and discussion

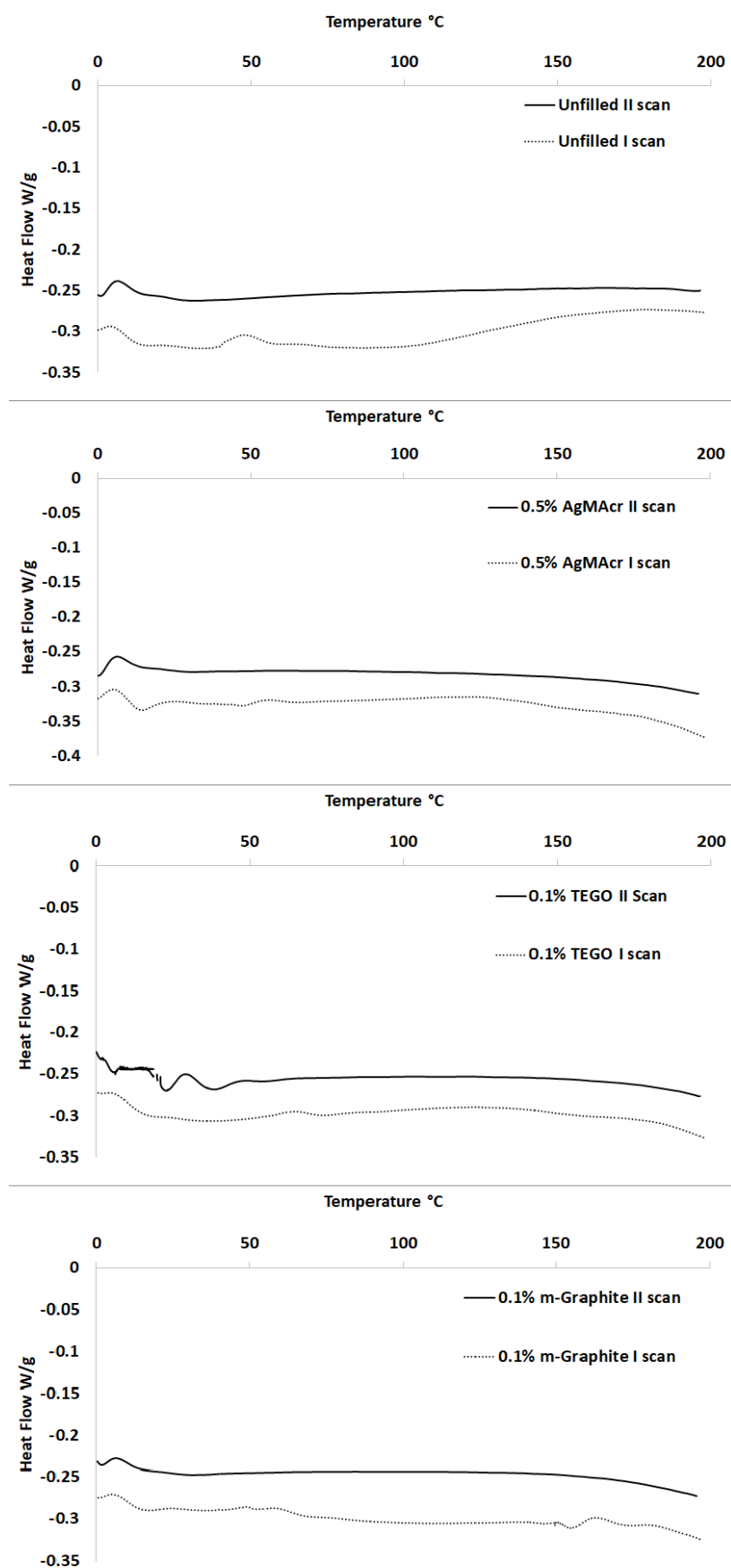


Figure 80: differential scanning calorimetry (DSC) thermograms (exothermic up) of all the different composition printed specimens (first two heating scans shown)

3.3.2.1.2 FTIR

The degree of curing is estimated with the comparison of FTIR spectra between liquid and cured formulations after STLG process. Figure 81 shows the spectra of the filled printed samples and the liquid base formulation before the printing process. The disappearing of the 3 peaks at around $3100-3000\text{ cm}^{-1}$ can be observed after the STLG process has occurred. The peaks are 3 because there are 3 monomers components in the formulation. These peaks are connected to the stretching of the =C-H bond in the methylene group [61]. Since the C=C bond is only present in the liquid acrylic monomers but it is substituted by a single C-C bond after the crosslinking, this particular =C-H bond stretching can be used as a reference signal for the residual presence of unreacted acrylic groups. Since the DSC thermograms show no clear exothermic peak in the printed samples, and FTIR also confirms the trend showing the disappearing of the acrylic-related peaks, it is possible to conclude that the STLG process is able to obtain a fully complete polymerisation, without the need of any further post-treatment. This is totally in agreement with the fact that STLG is a process based on DLP technology and DLP is more efficient in the formulation conversion than SLA systems.

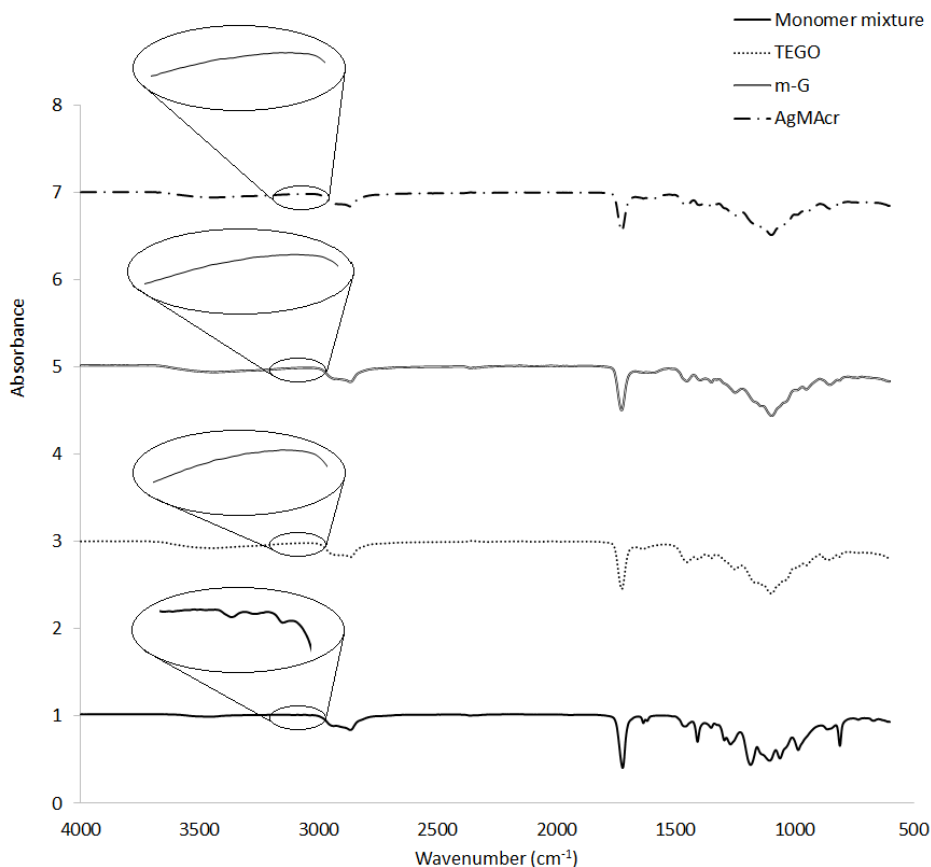


Figure 81: FTIR spectra of the liquid monomer mixture and of the 3 loaded composition printed samples.

3.3.2.1.3 XRD

Figure 82 shows the X-ray diffractogram of the sample containing 0.5% w/w AgNPs from AgMAcr as precursor. In the same graph, there are the diffraction peaks of the metallic silver (highlighted in red). There is a strong correspondence between the peaks of the printed sample and the Bragg's reflection of the face-centred-cubic form of metallic silver (ICCD-JCPDS card no. 04-0783) [153]. This means that the AgMAcr salts dispersed in the formulation has reacted with the light in a photoreduction process that brought to the formation of metallic silver nanoparticles. The size of the particles can be deduced from the peak broadening, commonly observed when the powder has nanometric size [135].

Results and discussion

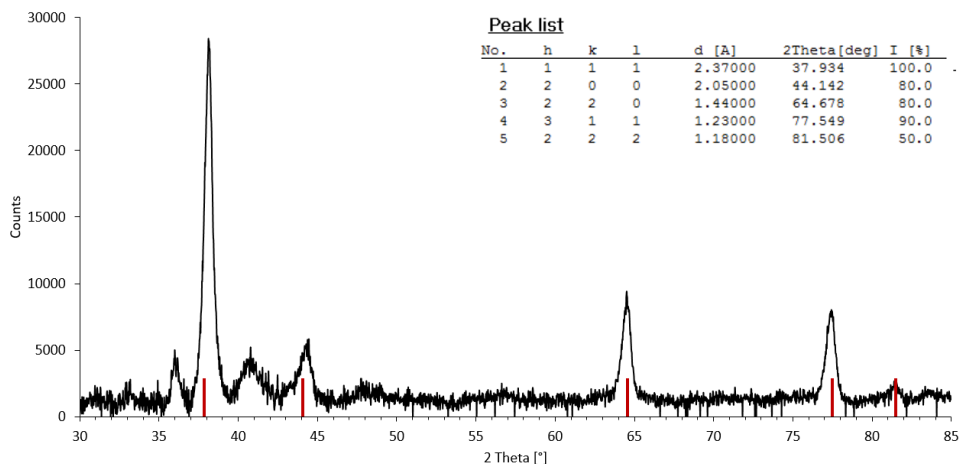


Figure 82: X-ray diffraction pattern of 3D printed material containing 0.5% w/w AgNPs from AgMAcr as precursor. In red the position of the diffraction peaks of metallic Ag as shown in the peak list (JCPDS 04-0783).

3.3.2.1.4 Micro computer tomography - m-CT

Table 13 shows the results of the volume and porosity calculation. The porosity is very low for all the samples, except for the TEGO. TEGO sample exhibit a porosity of more than 1% that can be seen also in Figure 83(IV) in the form of small bubbles evenly distributed on the volume of the sample. This is a clear example of the difficulties in the compatibilisation between fillers and the matrix. TEGO is a very hard to disperse filler, at least inside the kind of resin used, and the prolonged (5h) ultrasound dispersion adopted may not be sufficient. Probably a chemical surface modification of the TEGO with some kind of coupling agent can be recommended to try to avoid this problem. The presence of porosity can explain the decrease in mechanical properties experienced by TEGO graphene filled samples, but not completely, since a smaller decrease can be noted even for Ag and m-G filled samples.

Table 13: volume and porosity of the samples used for m-CT scans.

Sample	Volume (μm^3)	Porosity (%)
Control	7.5965E+011	7.2918E-004
Ag	7.2441E+011	4.3425E-003
m-G	8.4906E+011	7.3392E-003
TEGO	7.0002E+011	1.6265E+000

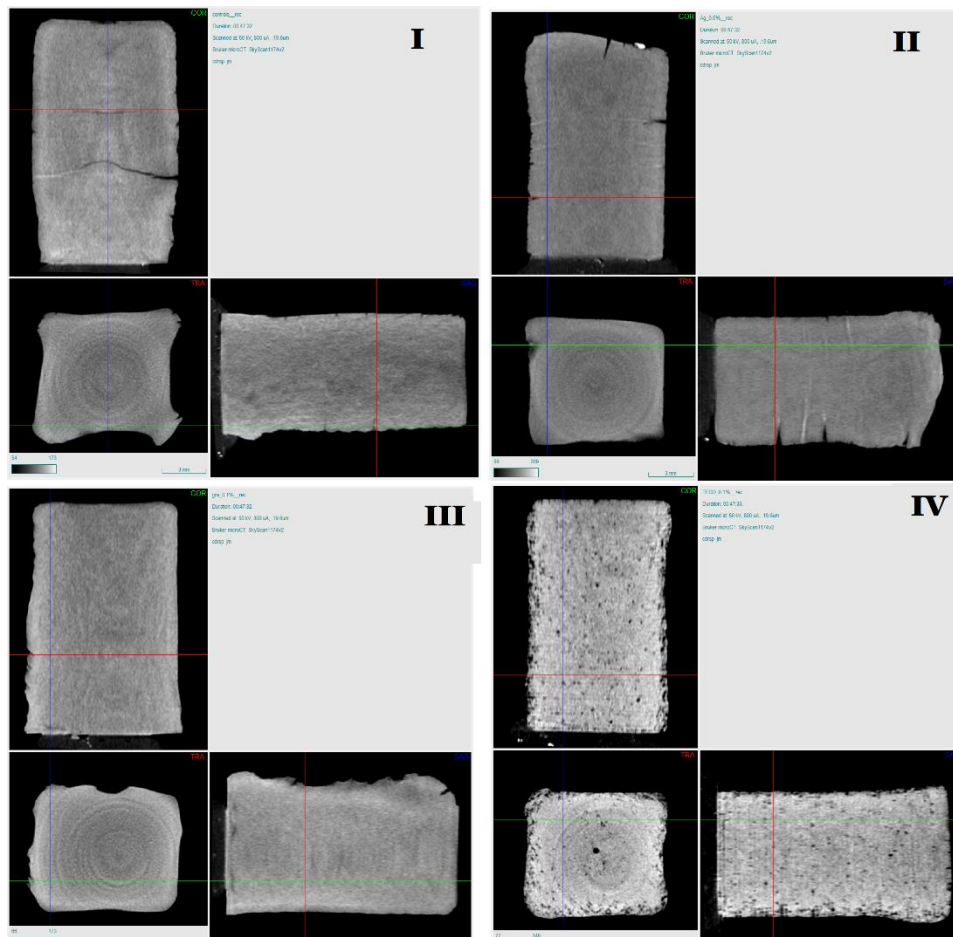


Figure 83: virtual cross sections of the fabricated objects made with micro computer-tomography (m-CT):. (I) control; (II) Ag; (III) m-G; (IV) TEGO.

3.3.2.1.5 Compression

The results of the compression tests along both the directions are presented in Table 14 and Table 15, while Figure 85 presents the representative stress strain diagrams for each sample typology.

With the exception of the deformation at break all the mechanical properties are better in z direction than in xy. This can be due to a better performance of the material if compressed on the same direction of the planes of the layers, but most probably it is due to the interference of contact issues. As can be noted from the m-CT images (Figure 83), the outer surfaces of the samples are much more defined and parallel to each other in the case of the base and top surfaces, than of the sides.

Results and discussion

Regarding the deformation at break, all the filled samples almost double the 12% value of both xy and z direction of the control, having values floating around 20% or more. The filler particle, regardless of their metallic or organic nature and regardless of their dimension also, all exhibit a good influence on deformation at break under compression of these 3D printed specimens. This result is quite impressive thinking of all the issues with increased fragility deriving from the addition of fillers to polymers that are reported in literature [99].

The compression mechanical properties, like ultimate compression strength (UCS) and Young's modulus (E), increase in the xy direction from the control unfilled samples to the filled ones. However, this is no longer true when considering the z direction, where all the opposite occurs. In the z direction, the compression properties decrease more and more from the control to the AgNPs filled samples, to the graphite ones and reach the lowest values for the TEGO. This can be due to the air bubbles trapped inside the TEGO samples and, more in general, to a non-homogeneous dispersion of the filler inside the matrix that could have brought to the formation of fillers aggregates. The filler can act properly only if well dispersed [99,154–156], if not it can actually decrease the pristine matrix properties.

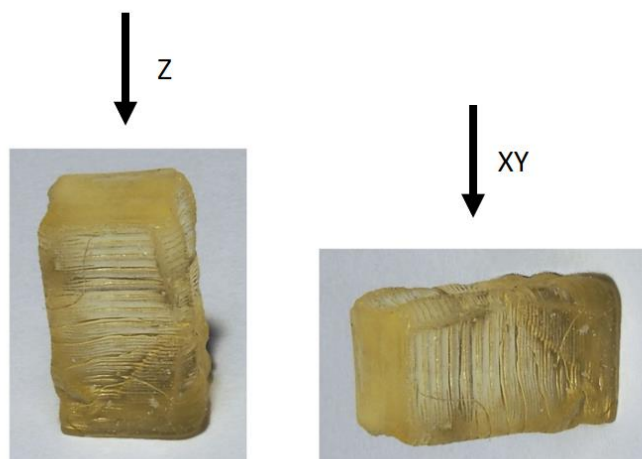


Figure 84: test direction, Z axis on the left and XY plane on the right. The layers and their direction are clearly visible.

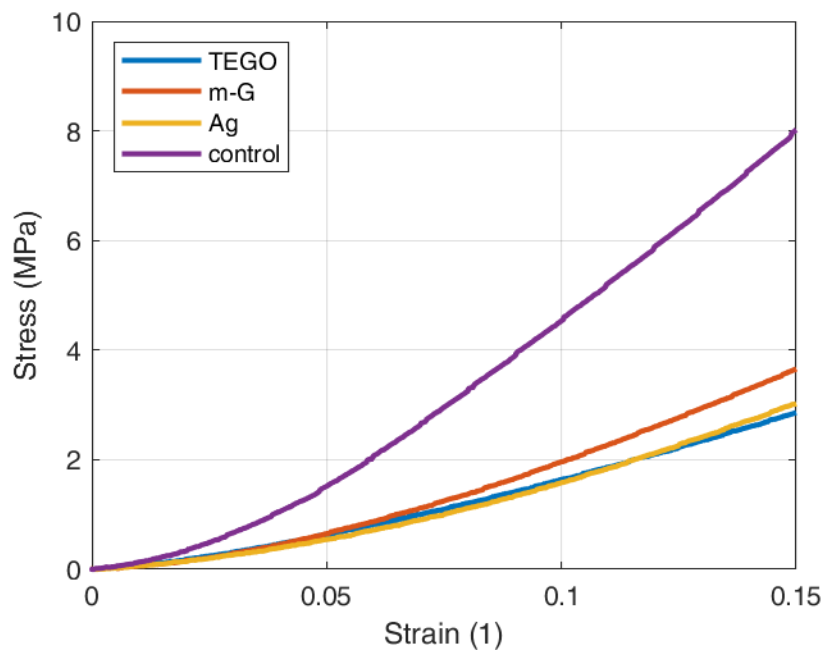


Figure 85: representative stress-strain curves for the 3D printed samples.

Table 14: tensile properties of 3D printed specimens tested on xy direction (E: Young’s modulus; UCS: ultimate compression strength; ϵ_B compression strain at break

xy	E (MPa)	UCS (MPa)	ϵ_B
control	7.31±6.39	0.735±0.678	0.12±0.07
Silver	24.26±7.34	3.55±1.27	0.22±0.04
Graphite	34.03±8.36	4.21±1.41	0.26±0.04
TEGO	6.18±3.41	2.05±0.152	0.27±0.01

Table 15: tensile properties of 3D printed specimen tested on z direction (E: Young’s modulus; UCS: ultimate compression strength; ϵ_B compression strain at break

z	E (MPa)	UCS (MPa)	ϵ_B
control	80.94±16.67	11.97±2.39	0.12±0.02
Silver	36.85±4.26	5.45±0.656	0.21±0.01
Graphite	44.95±12.47	7.71±1.87	0.24±0.02
TEGO	24.60±4.44	3.75±0.785	0.19±0.02

3.3.2.1.6 Conductivity

All the electric measurements were performed with a 2-probe method, on a homemade hardware for conductivity measurements. The measurement were taken simultaneously with the compression testing.

Table 16 and Table 17 show the conductivity results for the samples in xy and z direction respectively, while Figure 86 shows representative curves of conductivity vs compressive strain.

The addition of the fillers has a strong impact on the conductivity values of the materials, and seems not to be affected by the regressive effect of the mechanical properties. Table 16 shows the increase of 1 order of magnitude in the conductivity from the control to the filled samples. But more interesting is Table 17 where an increase of 2 order of magnitude can be noted for the TEGO samples. In z direction, conductive silver nanoparticles have the effect to increase more than 10 times the conductivity value, a better performance are able to produce the graphite filled samples with more than 20 times higher conductivity values even if the dimension of this filler are micrometric and not nanometric as the silver. But the best performance is given by the nanometric TEGO filled samples. The heavily reduced graphene oxide high conductivity, the nanometric dimensions, the flake form of TEGO that helps percolation: these three factors together guarantee an increase in the conductivity of almost 150 folds, despite of the porosity.

Figure 86 shows the curves of conductivity during compression. The initial increase is due to partial contact phenomena. In this figure, it is easily noticeable the different orders of magnitude of the conductivity.

Table 16: conductivity values in xy direction

xy	γ ($\mu\text{S/m}$)
control	0.34±0.226
Silver	6.98±1.05
Graphite	2.45±0.200
TEGO	6.74±0.722

Table 17: conductivity values in z direction

z	γ ($\mu\text{S/m}$)
control	1.06 \pm 0.0723
Silver	11.2 \pm 2.88
Graphite	27.2 \pm 4.62
TEGO	153.2 \pm 25.5

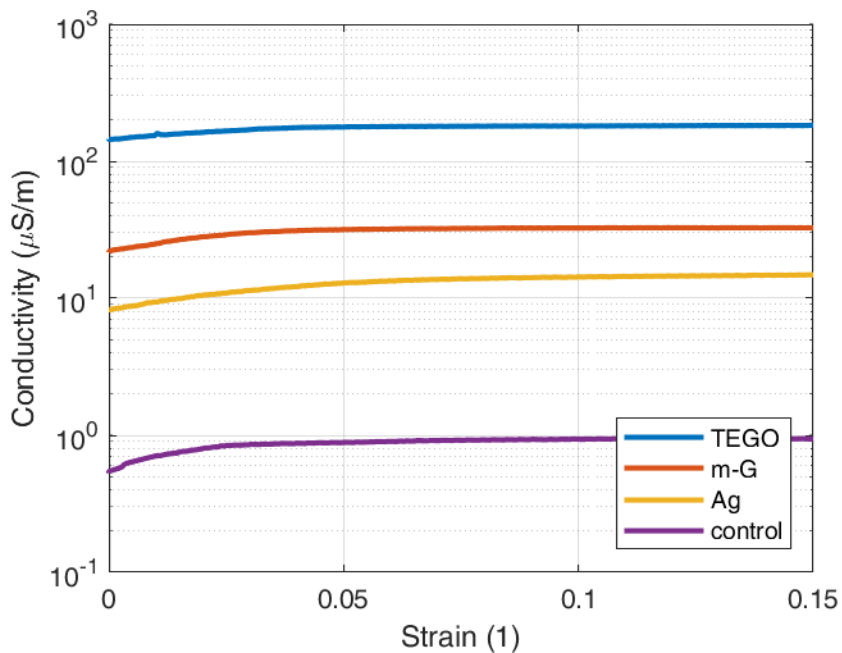


Figure 86: representative conductivity vs strain curves of the 3D printed samples

3.3.3 Discussion (final considerations)

The duration of the compression tests, the time intervening between the beginning of the compression and the failure of the specimen, can be assumed as an indication of the goodness of the results. The reproducibility of the test is higher if the times for the same kind of samples are similar. The standard deviation of test time is higher for less similar sample performances, the more a sample is uniform and the more the test times should be similar. In Table 18 and Table 19 there are reported the duration of the compression tests of filled and unfilled samples along xy and z direction. It can be noted that, not only the duration of the

Results and discussion

test in z direction is longer, but also the standard deviation is lower in percentage (with the exception of the TEGO which has low values also for the xy direction standard deviation).

Table 18: duration of compression tests in xy direction

xy	Test time (s)
control	66.4±38.52
Silver	118.0±23.31
Graphite	147.7±21.56
TEGO	130.2±6.79

Table 19: duration of compression tests in z direction

z	Test time (s)
control	194.9±21.55
Silver	199.2±7.51
Graphite	235.7±23.19
TEGO	181.6±17.94

It can be noted that the material exhibits no linear region, especially at the beginning (Figure 87 left). A quasi linear strain has been identified as the virtual zero strain point: the strain that simulates the absence of any initial partial contact. The procedure, described in the materials and methods section, brought to the identification of two quasi linear strains: one from the mechanical data (Figure 87 left, ϵ_{ql}^m) and another from the electrical data processing (Figure 87 right, ϵ_{ql}^e). These quasi linear strains, for all the samples filled and unfilled, are reported in Table 20 for the xy direction and Table 21 for the z direction. In those tables, there are reported also the ratios between the two different values of quasi linear strain. The more they are similar, the more the ratio is close to 1, and the more the procedure is confirmed. Again, it can be noted that for xy direction the ratio of control and graphite are low, meaning that these samples were affected by some noise deriving from irregularity in the outer surfaces and the non-standard method test. Silver and TEGO filled samples, which were much more regular on the lateral surfaces, show a better behaviour giving more comparable quasi linear strains. Much better results are given by the z direction tests. TEGO

Results and discussion

filled samples reach an outstanding 0.999 ratio, the control and the graphite give a much more regular output, and also silver is quite close to 1 having almost 0.8 of ratio.

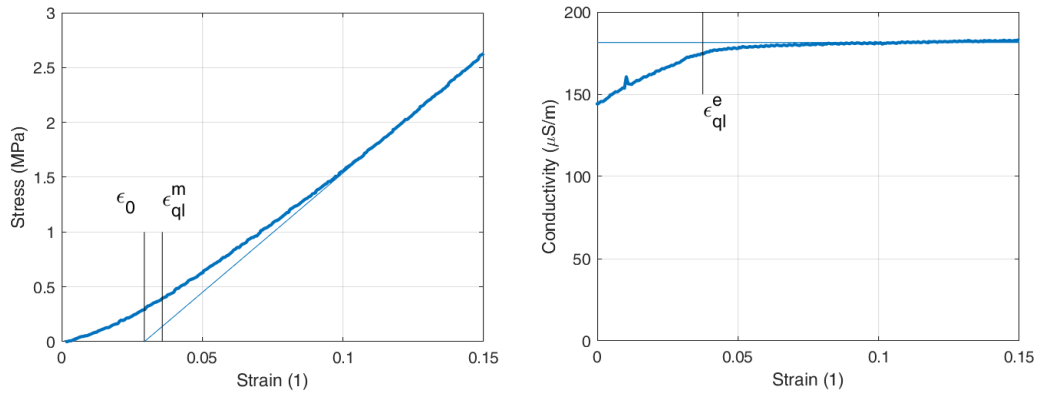


Figure 87: ϵ_{ql}^m ϵ_{ql}^e “quasi linear strain” values derived from mechanical (ϵ_{ql}^m) and electrical (ϵ_{ql}^e) data processing.

Table 20: “quasi linear strain” values derived from mechanical (ϵ_{ql}^m) and electrical (ϵ_{ql}^e) data processing for specimens in xy direction. The ratios between those quantities are reported as a proof of the goodness of the procedure.

xy	ϵ_{ql}^m	ϵ_{ql}^e	$\epsilon_{ql}^m / \epsilon_{ql}^e$
control	0.027±0.017	0.048±0.040	0.556
Silver	0.052±0.011	0.064±0.013	0.807
Graphite	0.061±0.010	0.103±0.012	0.592
TEGO	0.063±0.004	0.065±0.010	0.963

Table 21: “quasi linear strain” values derived from mechanical (ϵ_{ql}^m) and electrical (ϵ_{ql}^e) data processing for specimens in z direction. The ratios between those quantities are reported as a proof of the goodness of the procedure.

z	ϵ_{ql}^m	ϵ_{ql}^e	$\epsilon_{ql}^m / \epsilon_{ql}^e$
control	0.048±0.005	0.053±0.008	0.900
Silver	0.050±0.002	0.064±0.014	0.774
Graphite	0.058±0.006	0.050±0.026	1.176
TEGO	0.046±0.005	0.046±0.008	0.999

3.3.4 Conclusion

This work demonstrates that a DLP based technique, working with visible blue light and IR, can simultaneously reduce a silver salt to generate in situ AgNPs while polymerising the liquid monomer into a solid matrix. The DLP process usually does not have the power to reduce the silver salt that has to be post processed thermally or UV after the printing step. The addition of a contextual thermal treatment, supplied by the IR irradiation during the process, has the function to help this process avoiding any reduction post-treatment. Moreover, the silver salt selected, silver methacrylate, allows to obtain a homogeneous nanocomposite material without extractable by-products. The absence of by-products makes the silver nanocomposite potentially eligible for applications in delicate sectors like biomedical and food packaging. Another interesting aspect of the process is the very short printing time given by the DLP system united with the possibility to use very high layer thicknesses (here 250 microns was selected, but the machine can operate even on millimetres if required).

The electrical properties of the base matrix are increased by all the fillers at least of one order of magnitude and by almost 150 times in the case of TEGO. This approach, if pushed further with higher filler contents and better performing homogenisation and dispersion strategies, can produce even stronger increases in the conductivity. Here, the bases of a new conductive 3D printing material and technique are posed.

The electrical data measurement contextual to the compression testing was all homemade and prototypal, as well as the whole printer system. The method developed to process mechanical and electrical data has been developed specifically for this experiment and brought to a new way to correlate mechanical and electrical data during compression to find the “zero strain” point in condition of quasi linearity where the standard cannot be applied because of non-ductile behaviour of the material.

A study on the differences between xy and z testing direction has been also carried out for compression and electrical properties.

3.4 “Failures” (that is opportunities)

Not always everything goes as it should. It can happen that the expected results do not come, or that they turn out to be very different from the desired ones. Even if such eventualities can look as failures, they can also be precious opportunities to improve, learn and maybe correct the hypotheses and finally eventually succeed.

3.4.1 Silver nitrate *in situ* reduction

Silver nitrate was tried as a silver nanoparticles precursor salt. After the good results obtained with silver acetate [135], the preliminary tests with polymerisation under UV lamp showed that silver nitrate was able to dissolve completely into water that could have been added to the liquid PEGDA to form an homogeneous solution, avoiding the visible phase separation occurring when using silver acetate. The homogeneous solution could have been the basis for a much more homogeneous and stable dispersion of the salt and consequently of the AgNPs. Nonetheless, it was observed that when the silver nitrate and PEGDA formulation was processed through SLA, the light intensity was not able to *in situ* reduce the silver salt to metallic silver nanoparticles, and the crystalline phases, evidenced by the XRD characterisation, were mainly silver salt or silver oxide, with just a small presence of reduced metallic silver (Figure 88). The XRD analyses were repeated after thermal and UV post treatments, but with no better results.

The problem with the reactivity of silver nitrate was the opportunity to better test other silver salts and develop a method to synthesise silver acrylate and methacrylate. The addition of these salts brought to the creation of nanocomposites where silver nanoparticles were reduced and well dispersed, while the matrix was free of by-products as acrylic and methacrylic parts of the salt can react with the acrylic resin formulation, as opposed to the nitrate one.

Results and discussion

Maybe using different machine with different laser power or providing more suitable post-treatments or even different monomers, can result in a stable and complete reduction also of the silver nitrate. This can be the object of future experiments.

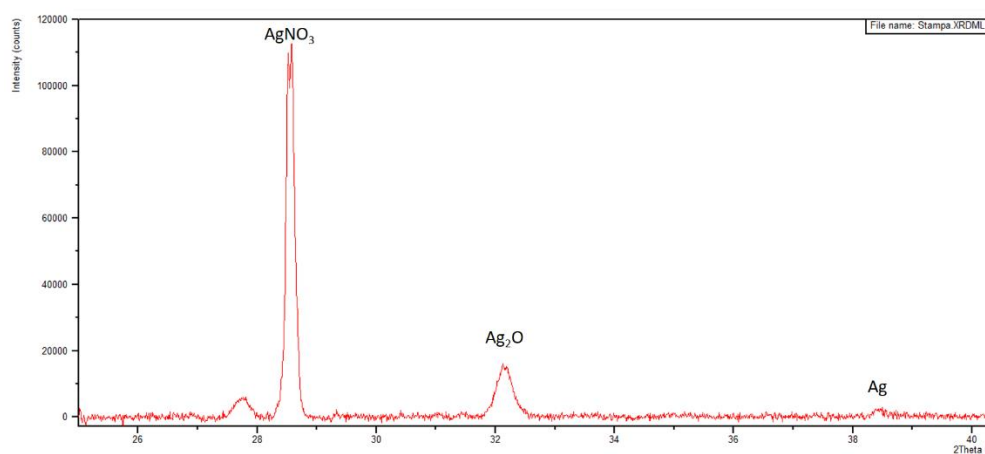


Figure 88: XRD diffraction pattern of an untreated samples right after SLA process, the silver nitrate is largely unreacted or oxidised, with just traces of metallic silver

3.4.2 TEGO compatibility and dispersion issues

TEGO graphene is potentially an outstanding filler. It has almost the same properties as graphene, but without the cost of it. In fact, the process to obtain it is less complex and expensive. The results obtained with this filler are good for the enhancement of electrical properties but poor for the increment in mechanical ones. It is largely reported [157–159], the use of graphene as a filler that enhances the mechanical properties. In the work carried on in this doctorate, it became evident that the problem with TEGO graphene is the compatibilisation with the matrix. Once the interfacial issues are solved, then the material that can be obtained should get much better properties. The dispersion and homogenisation are also critical, together with the modification of the interface; a strategy must be developed to increase the dispersability and stability of TEGO inside the liquid monomer to avoid agglomeration that inevitably decrease mechanical properties and the efficiency of the filler

Results and discussion

itself. In Figure 89 (b) and (c) the poor dispersion is visible in the small black dots of aggregated TEGO.

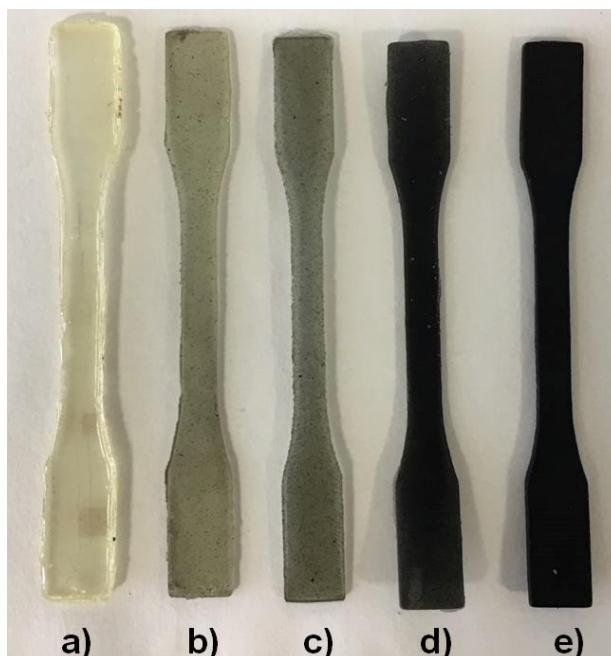


Figure 89: TEGO filled samples at different concentration (a) unfilled, (b) 0.005%, (c) 0.01%, (d) 0.05%, (e) 0.1%. at low concentration (b, c) the small black dots are the visible aggregates

3.4.3 Graphene synthesis inside monomer

To solve the interface issues between graphene and the liquid monomer, an attempt to synthesise graphene directly *in situ* inside the liquid monomer was tried. Starting from graphite it was tried to obtain graphene through prolonged ultrasound treatment directly inside the acrylic matrix (in that case PEGDA). The exfoliation of the graphite provoked by the ultrasound should have generated graphene sheets with less interfacial issues with the monomer because generated directly inside it. The treatment was carried in ice bath to prevent heat induced polymerisation and after 2.5 hours a well dispersed graphite-monomer mixture was left overnight with no stirring. The day after the PEGDA 250 dispersion was precipitated and clear again with the graphite deposited in the bottom, while the PEGDA 700 was still black, probably because of the higher viscosity. The method should be improved

and further tested. A different, more viscous, monomer and a more powerful and prolonged ultrasound treatment must be tried. The results must be characterised in deep to see if it is possible and convenient to in situ generate graphene starting from a graphite dispersion in the base monomer.

3.4.4 Partial-contact models: a no-success story (see section 2.2.2.4.1)

The partial-contact models are an attempt to determine quantitatively the mechanical partial contact in the early stage of the compression test by correlating it with the information gathered from the electrical conductivity increase. Several models have been identified and tested trying to match the data. Unfortunately, none of the models fitted the data with the desired accuracy: the partial contact can be observed electrically, but further research is needed to find the proper model.

3.4.5 Copper

Attempts were made to substitute silver with copper in the development of SLA processable nanocomposites. Copper was chosen for its lower cost and greater conductivity, together with its high antimicrobial activity. Initial tests under UV lamp were carried out to evaluate the reducibility of the copper salts under UV. Copper salts were found to be more difficult to reduce and very unstable in the reduced state because it has a strong tendency to re-oxidise as illustrated in Figure 90. Every solution tried, also the one illustrated in the following figure, was stirred to obtain homogeneous dispersion of the salt particles into the ethanol. Dispersion was then irradiated for 1 to 60 minutes to see colour changes subsequent to the copper salt reduction. After every irradiation step the solution was yellow and limpid at the top while still blue and opaque at the bottom, so it was necessary another stirring step. The process is carried out until the solution turns completely yellow and clear with no blue residues or salt particles. In Figure 90 the solution reaches the yellow clear state after 30 minutes, no changes between 30 and 60 minutes of UV treatment can be determined. The

Results and discussion

solution is then kept still overnight for 12 and 24 hours and turns completely blue again (but with no opacity) in a stable re-oxidised state.

The FTIR characterisation (here not reported) evidenced higher peak values for the copper salt than for the metallic copper, confirming the inefficacy of the treatment under UV.

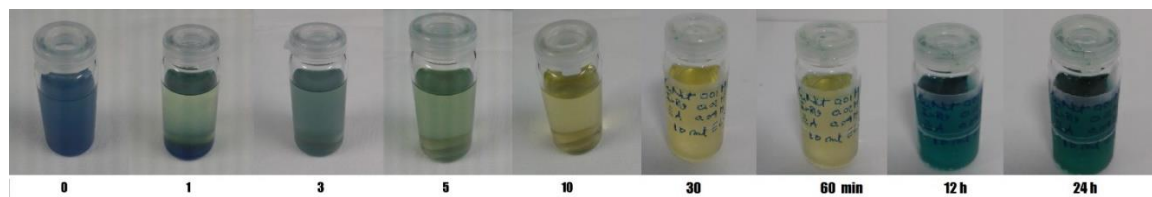


Figure 90: copper nitrate 0.01 M in 10 ml EtOH, Ir 819 0.02 M, ethanolamine as reducing agent 0.04 M, 3 minutes ultrasonic dispersion of the salt, 1 to 60 minutes UV lamp.

3.5 Future perspectives

The research effort never reaches an end, there are always new ways to improve and combine the results obtained. Hereafter some ideas to further develop this thesis are presented.

3.5.1 Variation in the filler concentration, addition and combination of different fillers

The work here presented could be implemented and further developed considering the effect of the variation of the filler concentration, the addition of other fillers and the combination of different fillers. Percolation effects could be reached with higher TEGO percentages and better dispersion or even substituting the TEGO sheets with carbon nanotubes (CNTs). The different functionalisation given by the fillers could be combined together following the specific requirements of the applications, so electrical conductivity could be combined to antimicrobial activity adding to the silver nanoparticles a certain

amount of reduced graphene oxide (rGO). Not to be excluded a synergic effect on the enhancement of properties of the combination of different fillers.

3.5.2 The variation of process parameters

An interesting aspect to be considered, is the influence of the technological parameters on the production of the composite materials. The reaction occurring are deeply connected to the process parameters involved, such as light intensity or laser scanning path and speed. Some reactions that do not start or are not completed by one technology with certain process parameters can be fully accomplished with other process parameters or different VP technologies.

3.5.3 GO: *in situ* photo-reduction to enhance conductivity

As already seen, the major limitation occurring in the preparation of TEGO composites is the compatibilisation between filler and matrix. The graphene is strongly hydrophobic and does not mix well with the tested monomers, on the contrary graphene oxide (GO) is hydrophilic. The addition of graphene oxide to the liquid formulations should be easier and it can also be favoured by the dispersion of the filler inside water as preliminary compatibilisation strategy. Once inside the formulation, GO should be reduced *in situ* with the same approach used to reduce silver salts, exploiting the same light source that supplies the energy for the polymerisation. This approach could guarantee a better dispersion and homogeneity of the filler, together with a simultaneous reaction approach capable to convert a non-conductive filler (GO) into a highly conductive one (rGO).

Conclusion

This thesis presents the work done during the doctorate studies of the author. Even if the research was funded for a specific project concerning the connection between additive manufacturing (AM) and automotive, it has been tried to maintain a certain degree of generality, and applications have been found also for other industrial sectors.

More specifically, the purpose of the work here reported was the design, development and characterisation of nanocomposite formulations to be processed through AM, with a focus on the automotive sector. Nevertheless, not only nanocomposite, but also single monomer property-changing unfilled materials and microcomposites were developed. The family of AM technique chosen is the vat photopolymerisation (VP) processes. VP works photopolymerising liquid formulations to obtain solid 3D objects with the maximum level of accuracy with respect to the others AM techniques. Together with commercial SLA printers, a prototype stereo-thermo-lithographic printer (STLG) was set up and successfully tested in a configuration never used before. Furthermore, a completely novel characterisation technique and equipment used to combine information from mechanical compression to electrical conductivity testing, was designed and produced. This equipment, and the software developed upon it, allowed a better understanding of the material properties and a deeper connection between mechanical and electrical properties.

A new simple method for the preparation of photopolymerisable acrylic resins with tuneable mechanical and viscoelastic properties is presented. The process does not involve any chemical modification of the base monomers and not even the addition of different monomers, the tuning is obtained by the simple blending of different molecular weight monomers. In this case the two monomers used were PEGDA 250 and PEGDA 700. The results showed a wide spectrum of properties: glass transition temperature was ranging from -30 to 60 ° C, while elastic modulus can take values from about 20 to 700 MPa.

A novel simultaneous SLA process of photo-polymerisation of a mixture of acrylic resins and contextual silver nanoparticles formation is presented. The formation of silver nanoparticles is activated by the *in situ* photo-reduction of silver precursor salts with carbon-

carbon double bonds (C=C) such as silver acrylate and silver methacrylate. The adoption of these kind of salts, capable to interact with the acrylic monomers and take part to the 3D crosslinking process, avoids the downside of having to deal with by-products release that can compromise the adoption of these materials for specific and delicate kinds of application (e.g. biomedical, healthcare and all the application in contact with the human body). The addition of a small amount of filler, between 0.5 and 2% of silver nanoparticles, has a good impact on the mechanical and viscoelastic properties. It has the effect to increase the T_g by even more than 10° , the Young's modulus from about 70 to more than 150 MPa, the UTS can be increased to 150% of the unfilled value, the elongation at break decrement, due to the increment of fragility expected for any filled sample, can be limited to less than 25%, the storage modulus at 60°C increases from 65 to 140 MPa.

A prototype STLG printer was set up in a never before experimented configuration with a double visible and IR radiation. This DLP based double system was capable to fully cure the polymeric matrix and simultaneously reduce silver precursor salt to metallic silver, as previously reported for SLA. The photoreduction of silver salts to metallic silver was never attested in a contextual *in situ* process on a DLP system, the energy provided is normally too low to polymerise and photo-reduce the salt. The addition of a second radiation and the direct control of all the process parameters are key factors to induce this photoreduction during the printing process. Other systems were tried on this STLG printer, in particular two carbon based systems: a microcomposite with graphite flakes and a nanocomposite with thermally expanded graphite oxide (TEGO), a highly-reduced graphite oxide that is thermally exfoliated to become a sort of less expensive graphene. This conductive filler can increase by two orders of magnitude the electrical conductivity even at low percentages (0.1% wt.), the same filler content of micrometric graphite was able to increase conductivity by one order of magnitude only (having almost the same effect as silver, which however was present in the much higher concentration of 0.5% wt.).

The projects reported brought all to the development of 3D formulations with good stability and printability, they can reach high or total degree of cure right during the VP process. Nevertheless, a set of different post-treatment were specifically adapted to each material and process, where needed. Procedures were proposed and applied for the

synthesis of silver precursor salts to act as precursor of silver nanoparticles, for monomer combination and choice, and matrix preliminary tests and optimisation.

Some of the inevitable obstacles and hitches occurring during a three-year-old doctorate were also reported to analyse them and learn from them in a way that can bring to eventually solve them or at least do not repeat them. Obstacles are perfect teachers and can give the opportunity to improve and find better solutions to the problems occurring during research activities.

Moreover, some possible future developments of this thesis project were reported as suggestions for further investigations on this interesting and evolving research field. AM is a market on tremendous expansion having tripled its turnover in the last three years, and forecasts are reported of further increments of the same nature in the next years.

References

- [1] G. Taormina, C. Sciancalepore, M. Messori, F. Bondioli, 3D printing processes for photocurable polymeric materials: technologies, materials and future trend, *J. Appl. Biomater. Funct. Mater.* (2018) 1–32. doi:10.1177/2280800018764770.
- [2] G. Taormina, C. Sciancalepore, F. Bondioli, M. Messori, Special resins for stereolithography: In situ generation of silver nanoparticles, *Polymers (Basel)*. 10 (2018). doi:10.3390/polym10020212.
- [3] ASTM International, F2792-12a - Standard Terminology for Additive Manufacturing Technologies, *Rapid Manuf. Assoc.* (2013) 10–12. doi:10.1520/F2792-12A.2.
- [4] B. Mueller, *Additive Manufacturing Technologies – Rapid Prototyping to Direct Digital Manufacturing*, *Assem. Autom.* (2012). doi:10.1108/aa.2012.03332baa.010.
- [5] P.J. Bártolo, *Stereolithography: Materials, Processes and Applications*, Springer, New York, 2011. doi:10.1007/978-0-387-92904-0.
- [6] A. Urrios, C. Parra-Cabrera, N. Bhattacharjee, A.M. Gonzalez-Suarez, L.G. Rigat-Brugarolas, U. Nallapatti, J. Samitier, C.A. Deforest, F. Posas, J.L. Garcia-Cordero, A. Folch, 3D-printing of transparent bio-microfluidic devices in PEG-DA, *Lab Chip*. 16 (2016) 2287–2294. doi:10.1039/c6lc00153j.
- [7] J.W. Stansbury, M.J. Idacavage, 3D printing with polymers: Challenges among expanding options and opportunities, *Dent. Mater.* 32 (2016) 54–64. doi:10.1016/j.dental.2015.09.018.
- [8] E. Fantino, *A new approach for the development of DLP-3D printable functional materials* By, 2017.
- [9] N. Guo, M.C. Leu, *Additive manufacturing: Technology, applications and research needs*, *Front. Mech. Eng.* (2013). doi:10.1007/s11465-013-0248-8.
- [10] T.D. Ngo, A. Kashani, G. Imbalzano, K.T.Q. Nguyen, D. Hui, *Additive manufacturing (3D printing): A review of materials, methods, applications and challenges*, *Compos. Part B Eng.* 143 (2018) 172–196. doi:10.1016/j.compositesb.2018.02.012.
- [11] L.E. Murr, S.M. Gaytan, A. Ceylan, E. Martinez, J.L. Martinez, D.H. Hernandez, B.I. Machado, D.A. Ramirez, F. Medina, S. Collins, R.B. Wicker, *Characterization of titanium aluminide alloy components fabricated by additive manufacturing using electron beam melting*, *Acta Mater.* (2010). doi:10.1016/j.actamat.2009.11.032.
- [12] L.E. Murr, S.M. Gaytan, F. Medina, E. Martinez, J.L. Martinez, D.H. Hernandez, B.I. Machado, D.A. Ramirez, R.B. Wicker, *Characterization of Ti-6Al-4V open cellular foams fabricated by additive manufacturing using electron beam melting*, *Mater. Sci. Eng. A.* (2010). doi:10.1016/j.msea.2009.11.015.
- [13] R. Ilardo, C.B. Williams, *Design and manufacture of a Formula SAE intake system using fused deposition modeling and fiber-reinforced composite materials*, *Rapid Prototyp. J.* (2010). doi:10.1108/13552541011034834.
- [14] D. Bourell, J.P. Kruth, M. Leu, G. Levy, D. Rosen, A.M. Beese, A. Clare, *Materials for additive manufacturing*, *CIRP Ann. - Manuf. Technol.* 66 (2017) 659–681. doi:10.1016/j.cirp.2017.05.009.
- [15] S.H. Ahn, M. Montero, D. Odell, S. Roundy, P.K. Wright, *Anisotropic material properties of fused deposition modeling ABS*, *Rapid Prototyp. J.* (2002). doi:10.1108/13552540210441166.
- [16] M. Montero, S. Roundy, D. Odell, *Material characterization of fused deposition modeling (FDM) ABS by designed experiments*, *Proc. Rapid Prototyp. Manuf. Conf.* (2001).
- [17] S.H. Masood, K. Mau, W.Q. Song, *Tensile Properties of Processed FDM Polycarbonate Material*, *Mater. Sci. Forum.* (2010). doi:10.4028/www.scientific.net/msf.654-656.2556.
- [18] A.G. Salazar-Martín, M.A. Pérez, A.A. García-Granada, G. Reyes, J.M. Puigoriol-Forcada, A

- study of creep in polycarbonate fused deposition modelling parts, *Mater. Des.* (2018). doi:10.1016/j.matdes.2018.01.008.
- [19] M.C. Wurm, T. Möst, B. Bergauer, D. Rietzel, F.W. Neukam, S.C. Cifuentes, C. von Wilmsowsky, In-vitro evaluation of Polylactic acid (PLA) manufactured by fused deposition modeling, *J. Biol. Eng.* (2017). doi:10.1186/s13036-017-0073-4.
- [20] A.S. El-Gizawy, S. Corl, B. Graybill, Process-induced Properties of FDM Products, *ICMET, Int. Conf. Mech. Eng. Technol. Congr. Expo.* (2011).
- [21] M. Rinaldi, V. Cherubini, V. Massarelli, V. Canala, F. Nanni, Polyetherimide based nanocomposites for aerospace applications, *J. Appl. Biomater. Funct. Mater.* (2016). doi:10.5301/jabfm.5000272.
- [22] V.S.D. Voet, T. Strating, G.H.M. Schnelting, P. Dijkstra, M. Tietema, J. Xu, A.J.J. Woortman, K. Loos, J. Jager, R. Folkersma, Biobased Acrylate Photocurable Resin Formulation for Stereolithography 3D Printing, *ACS Omega*. 3 (2018) 1403–1408. doi:10.1021/acsomega.7b01648.
- [23] J. Stampfl, S. Baudis, C. Heller, R. Liska, A. Neumeister, R. Kling, A. Ostendorf, M. Spitzbart, Photopolymers with tunable mechanical properties processed by laser-based high-resolution stereolithography, *J. Micromechanics Microengineering*. 18 (2008) 125014. <http://stacks.iop.org/0960-1317/18/i=12/a=125014>.
- [24] I.Q. Vu, L.B. Bass, C.B. Williams, D.A. Dillard, Characterizing the effect of print orientation on interface integrity of multi-material jetting additive manufacturing, *Addit. Manuf.* (2018). doi:10.1016/j.addma.2018.05.036.
- [25] I. Gibson, D. Rosen, B. Stucker, I. Gibson, D. Rosen, B. Stucker, Material Jetting, in: *Addit. Manuf. Technol.*, 2015. doi:10.1007/978-1-4939-2113-3_7.
- [26] C.E. Corcione, A. Greco, A. Maffezzoli, Photopolymerization kinetics of an epoxy-based resin for stereolithography, *J. Appl. Polym. Sci.* (2004). doi:10.1002/app.20347.
- [27] P. Cruz, E.D. Shoemaker, P. Adam, J. Leachman, Tensile strengths of polyamide based 3D printed polymers in liquid nitrogen, in: *IOP Conf. Ser. Mater. Sci. Eng.*, 2015. doi:10.1088/1757-899X/102/1/012020.
- [28] A.M. Abdullah, T.N.A. Tuan Rahim, D. Mohamad, H.M. Akil, Z.A. Rajion, Mechanical and physical properties of highly ZrO₂ / β -TCP filled polyamide 12 prepared via fused deposition modelling (FDM) 3D printer for potential craniofacial reconstruction application, *Mater. Lett.* (2017). doi:10.1016/j.matlet.2016.11.052.
- [29] M. Schmid, A. Amado, K. Wegener, Polymer powders for selective laser sintering (SLS), in: *AIP Conf. Proc.*, 2015. doi:10.1063/1.4918516.
- [30] C. Yan, Y. Shi, L. Hao, Investigation into the differences in the selective laser sintering between amorphous and semi-crystalline polymers, *Int. Polym. Process.* (2011). doi:10.3139/217.2452.
- [31] J. Yang, Y. Shi, Q. Shen, C. Yan, Selective laser sintering of HIPS and investment casting technology, *J. Mater. Process. Technol.* (2009). doi:10.1016/j.jmatprotec.2008.04.056.
- [32] O.S. Carneiro, A.F. Silva, R. Gomes, Fused deposition modeling with polypropylene, *Mater. Des.* (2015). doi:10.1016/j.matdes.2015.06.053.
- [33] L. Wang, D.J. Gardner, Effect of fused layer modeling (FLM) processing parameters on impact strength of cellular polypropylene, *Polymer (Guildf)*. (2017). doi:10.1016/j.polymer.2017.02.055.
- [34] W.S. Tan, C.K. Chua, T.H. Chong, A.G. Fane, J. An, Selective laser sintering of polypropylene feed spacers for spiral wound membrane modules, in: *Proc. Int. Conf. Prog. Addit. Manuf.*, 2016. doi:10.3850/2424-8967_V02-306.
- [35] F.A.M.M. Gonçalves, A.C. Fonseca, M. Domingos, A. Gloria, A.C. Serra, J.F.J. Coelho, The

- potential of unsaturated polyesters in biomedicine and tissue engineering: Synthesis, structure-properties relationships and additive manufacturing, *Prog. Polym. Sci.* (2017). doi:10.1016/j.progpolymsci.2016.12.008.
- [36] J. Seppälä, H. Korhonen, R. Hakala, M. Malin, Photocrosslinkable polyesters and poly(ester anhydride)s for biomedical applications, *Macromol. Biosci.* (2011). doi:10.1002/mabi.201100198.
- [37] W. Wu, P. Geng, G. Li, D. Zhao, H. Zhang, J. Zhao, Influence of layer thickness and raster angle on the mechanical properties of 3D-printed PEEK and a comparative mechanical study between PEEK and ABS, *Materials (Basel)*. (2015). doi:10.3390/ma8095271.
- [38] M. Rinaldi, T. Ghidini, F. Cecchini, A. Brandao, F. Nanni, Additive layer manufacturing of poly (ether ether ketone) via FDM, *Compos. Part B Eng.* (2018). doi:10.1016/j.compositesb.2018.03.029.
- [39] M. Schmidt, D. Pohle, T. Rechtenwald, Selective laser sintering of PEEK, *CIRP Ann. - Manuf. Technol.* (2007). doi:10.1016/j.cirp.2007.05.097.
- [40] J. Xiao, Y. Gao, The manufacture of 3D printing of medical grade TPU, *Prog. Addit. Manuf.* (2017). doi:10.1007/s40964-017-0023-1.
- [41] S. Yuan, F. Shen, J. Bai, C.K. Chua, J. Wei, K. Zhou, 3D soft auxetic lattice structures fabricated by selective laser sintering: TPU powder evaluation and process optimization, *Mater. Des.* (2017). doi:10.1016/j.matdes.2017.01.098.
- [42] L. Hao, S. Mellor, O. Seaman, J. Henderson, N. Sewell, M. Sloan, Material characterisation and process development for chocolate additive layer manufacturing, *Virtual Phys. Prototyp.* (2010). doi:10.1080/17452751003753212.
- [43] I. Maskery, N.T. Aboulkhair, M.R. Corfield, C. Tuck, A.T. Clare, R.K. Leach, R.D. Wildman, I.A. Ashcroft, R.J.M. Hague, Quantification and characterisation of porosity in selectively laser melted Al-Si10-Mg using X-ray computed tomography, *Mater. Charact.* (2016). doi:10.1016/j.matchar.2015.12.001.
- [44] K. Kempen, L. Thijs, J. Van Humbeeck, J.-P. Kruth, Processing AlSi10Mg by selective laser melting: parameter optimisation and material characterisation, *Mater. Sci. Technol.* (2014). doi:10.1179/1743284714y.0000000702.
- [45] E. Brandl, U. Heckenberger, V. Holzinger, D. Buchbinder, Additive manufactured AlSi10Mg samples using Selective Laser Melting (SLM): Microstructure, high cycle fatigue, and fracture behavior, *Mater. Des.* (2012). doi:10.1016/j.matdes.2011.07.067.
- [46] D. Buchbinder, H. Schleifenbaum, S. Heidrich, W. Meiners, J. Bültmann, High power Selective Laser Melting (HP SLM) of aluminum parts, in: *Phys. Procedia*, 2011. doi:10.1016/j.phpro.2011.03.035.
- [47] B. Vandenbroucke, J.P. Kruth, Selective laser melting of biocompatible metals for rapid manufacturing of medical parts, *Rapid Prototyp. J.* (2007). doi:10.1108/13552540710776142.
- [48] X.Z. Xin, N. Xiang, J. Chen, D. Xu, B. Wei, Corrosion characteristics of a selective laser melted Co-Cr dental alloy under physiological conditions, *J. Mater. Sci.* (2012). doi:10.1007/s10853-012-6325-2.
- [49] M. Khan, P. Dickens, Selective Laser Melting (SLM) of pure gold, *Gold Bull.* (2010). doi:10.1007/BF03214976.
- [50] M. Khan, P. Dickens, Selective laser melting (SLM) of gold (Au), *Rapid Prototyp. J.* (2012). doi:10.1108/13552541211193520.
- [51] A. Carlotto, A. Loggi, P. Sbornicchia, D. Zito, D. Maggiani, A. Molinari, I. Cristofolini, Optimization of SLM technology: Main parameters in the production of gold and platinum jewelry, in: *Euro PM 2014 Congr. Exhib. Proc.*, 2014.

- [52] S. Li, Q. Wei, Y. Shi, C.K. Chua, Z. Zhu, D. Zhang, Microstructure Characteristics of Inconel 625 Superalloy Manufactured by Selective Laser Melting, *J. Mater. Sci. Technol.* (2015). doi:10.1016/j.jmst.2014.09.020.
- [53] K.N. Amato, S.M. Gaytan, L.E. Murr, E. Martinez, P.W. Shindo, J. Hernandez, S. Collins, F. Medina, Microstructures and mechanical behavior of Inconel 718 fabricated by selective laser melting, *Acta Mater.* (2012). doi:10.1016/j.actamat.2011.12.032.
- [54] T. Niendorf, S. Leuders, A. Riemer, H.A. Richard, T. Tröster, D. Schwarze, Highly anisotropic steel processed by selective laser melting, *Metall. Mater. Trans. B Process Metall. Mater. Process. Sci.* (2013). doi:10.1007/s11663-013-9875-z.
- [55] E. Yasa, J.P. Kruth, Microstructural investigation of selective laser melting 316L stainless steel parts exposed to laser re-melting, in: *Procedia Eng.*, 2011. doi:10.1016/j.proeng.2011.11.130.
- [56] R. Wauthle, S.M. Ahmadi, S. Amin Yavari, M. Mulier, A.A. Zadpoor, H. Weinans, J. Van Humbeeck, J.P. Kruth, J. Schrooten, Revival of pure titanium for dynamically loaded porous implants using additive manufacturing, *Mater. Sci. Eng. C.* (2015). doi:10.1016/j.msec.2015.05.001.
- [57] L. Thijs, F. Verhaeghe, T. Craeghs, J. Van Humbeeck, J.P. Kruth, A study of the microstructural evolution during selective laser melting of Ti-6Al-4V, *Acta Mater.* (2010). doi:10.1016/j.actamat.2010.02.004.
- [58] P. Edwards, M. Ramulu, Fatigue performance evaluation of selective laser melted Ti-6Al-4V, *Mater. Sci. Eng. A.* (2014). doi:10.1016/j.msea.2014.01.041.
- [59] Y.-C. Hagedorn, N. Balachandran, W. Meiners, K. Wissenbach, R. Poprawe, SLM of Net-Shaped High Strength Ceramics: New Opportunities for Producing Dental Restorations, in: *Proc. 22nd Solid Free. Fabr. Symp.*, 2011.
- [60] J. Wilkes, Y.C. Hagedorn, W. Meiners, K. Wissenbach, Additive manufacturing of ZrO₂-Al₂O₃ ceramic components by selective laser melting, *Rapid Prototyp. J.* (2013). doi:10.1108/13552541311292736.
- [61] J. Deckers, K. Shahzad, J. Vleugels, J.P. Kruth, Isostatic pressing assisted indirect selective laser sintering of alumina components, *Rapid Prototyp. J.* (2012). doi:10.1108/13552541211250409.
- [62] T.F. McNulty, D.J. Shanefield, S.C. Danforth, A. Safari, Dispersion of lead zirconate titanate for fused deposition of ceramics, *J. Am. Ceram. Soc.* (1999). doi:10.1111/j.1151-2916.1999.tb01996.x.
- [63] J.J. McIntosh, S.C. Danforth, V.R. Jamalabad, Shrinkage and deformation in components manufactured by fused deposition of ceramics, *Solid Free. Fabr. Proc.* (1997).
- [64] M.K. Agarwala, R. Van Weeren, R. Vaidyanathan, A. Bandyopadhyay, G. Carrasquillo, V. Jamalabad, N. Langrana, A. Safari, S.H. Garofalini, S.C. Danforth, J. Burlew, R. Donaldson, P. Whalen, C. Ballard, Structural Ceramics by Fused Deposition of Ceramics, *Solid Free. Fabr. Symp.* (1995).
- [65] M.L. Griffith, J.W. Halloran, Freeform Fabrication of Ceramics via Stereolithography, *J. Am. Ceram. Soc.* (2005). doi:10.1111/j.1151-2916.1996.tb09022.x.
- [66] C. Hinczewski, S. Corbel, T. Chartier, Stereolithography for the fabrication of ceramic three-dimensional parts, *Rapid Prototyp. J.* (1998). doi:10.1108/13552549810222867.
- [67] H. Wu, D. Li, N. Guo, Fabrication of integral ceramic mold for investment casting of hollow turbine blade based on stereolithography, *Rapid Prototyp. J.* (2009). doi:10.1108/13552540910979749.
- [68] J. Klein, M. Stern, G. Franchin, M. Kayser, C. Inamura, S. Dave, J.C. Weaver, P. Houk, P. Colombo, M. Yang, N. Oxman, Additive Manufacturing of Optically Transparent Glass, *3D*

Print. Addit. Manuf. (2015). doi:10.1089/3dp.2015.0021.

- [69] J. Luo, H. Pan, E.C. Kinzel, Additive Manufacturing of Glass, in: Vol. 2B Adv. Manuf., 2014. doi:10.1115/IMECE2014-39227.
- [70] C. Gosselin, R. Duballet, P. Roux, N. Gaudillière, J. Dirrenberger, P. Morel, Large-scale 3D printing of ultra-high performance concrete - a new processing route for architects and builders, *Mater. Des.* (2016). doi:10.1016/j.matdes.2016.03.097.
- [71] R.A. Buswell, W.R. Leal de Silva, S.Z. Jones, J. Dirrenberger, 3D printing using concrete extrusion: A roadmap for research, *Cem. Concr. Res.* (2018). doi:10.1016/j.cemconres.2018.05.006.
- [72] E. Zanchetta, M. Cattaldo, G. Franchin, M. Schwentenwein, J. Homa, G. Brusatin, P. Colombo, Stereolithography of SiOC Ceramic Microcomponents, *Adv. Mater.* (2016). doi:10.1002/adma.201503470.
- [73] I. Gibson, D.W. Rosen, B. Stucker, *Additive Manufacturing Technologies*, Springer, 2010. doi:10.1007/978-1-4419-1120-9.
- [74] C. Zhou, Y. Chen, Z. Yang, B. Khoshnevis, Development of a Multi-material Mask-Image-Projection-based Stereolithography for the Fabrication of Digital Materials, *Annu. Solid Free. Fabr. Symp.* (2011) 65–80.
- [75] T. Patrício, R. Pereira, L. Oliveira, P. Bártolo, Polyethylene glycol and polyethylene glycol/hydroxyapatite constructs produced through stereo-thermal-lithography, *Adv. Mater. Res.* 749 (2013) 87–92. doi:10.4028/www.scientific.net/AMR.749.87.
- [76] T. For, T. Micromachining, TWO-PHOTON POLYMERIZATION, (n.d.) 3–4.
- [77] J. Serbin, A. Egbert, A. Ostendorf, B.N. Chichkov, R. Houbertz, G. Domann, J. Schulz, C. Cronauer, L. Fröhlich, M. Popall, Femtosecond laser-induced two-photon polymerization of inorganic-organic hybrid materials for applications in photonics., *Opt. Lett.* (2003).
- [78] C. Heller, N. Pucher, B. Seidl, K. Kalinyaprak-Icten, G. Ullrich, L. Kuna, V. Satzinger, V. Schmidt, H.C. Lichtenegger, J. Stampfl, R. Liska, One- and two-photon activity of cross-conjugated photoinitiators with bathochromic shift, *J. Polym. Sci. Part A Polym. Chem.* (2007). doi:10.1002/pola.22078.
- [79] S. Maruo, O. Nakamura, S. Kawata, Three-dimensional microfabrication with two-photon-absorbed photopolymerization, *Opt. Lett.* (1997). doi:10.1364/ol.22.000132.
- [80] S. Kawata, H.B. Sun, T. Tanaka, K. Takada, Finer features for functional microdevices., *Nature.* (2001). doi:10.1038/35089130.
- [81] K. Kim, W. Zhu, X. Qu, C. Aaronson, W.R. McCall, S. Chen, D.J. Sirbuly, 3D optical printing of piezoelectric nanoparticle-polymer composite materials, *ACS Nano.* 8 (2014) 9799–9806. doi:10.1021/nn503268f.
- [82] R. Januszewicz, J.R. Tumbleston, A.L. Quintanilla, S.J. Mechem, J.M. Desimone, Layerless fabrication with continuous liquid interface production, 113 (2016) 11703–11708. doi:10.1073/pnas.1605271113.
- [83] X. Kuang, Z. Zhao, K. Chen, D. Fang, G. Kang, H.J. Qi, High-Speed 3D Printing of High-Performance Thermosetting Polymers via Two-Stage Curing, *Macromol. Rapid Commun.* 39 (2018) 1–8. doi:10.1002/marc.201700809.
- [84] N.D. Dolinski, Z.A. Page, E.B. Callaway, F. Eisenreich, R. V. Garcia, R. Chavez, D.P. Bothman, S. Hecht, F.W. Zok, C.J. Hawker, Solution Mask Liquid Lithography (SMaLL) for One-Step, Multimaterial 3D Printing, *Adv. Mater.* 30 (2018) 1–6. doi:10.1002/adma.201800364.
- [85] J.J. Martin, B.E. Fiore, R.M. Erb, Designing bioinspired composite reinforcement architectures via 3D magnetic printing, *Nat. Commun.* 6 (2015) 8641. doi:10.1038/ncomms9641.
- [86] R.M. Erb, R. Libanori, N. Rothfuchs, A.R. Studart, Composites reinforced in three dimensions

- by using low magnetic fields, *Science* (80-.). (2012). doi:10.1126/science.1210822.
- [87] R.M. Erb, K.H. Cherenack, R.E. Stahel, R. Libanori, T. Kinkeldei, N. Münzenrieder, G. Tröster, A.R. Studart, Locally reinforced polymer-based composites for elastic electronics, *ACS Appl. Mater. Interfaces*. (2012). doi:10.1021/am300508e.
- [88] V. Vishwakarma, S. Samal, N. Manoharan, Safety and risk associated with nanoparticles-a review, *J. Miner. Mater. Charact. Eng.* 9 (2010) 455–459. <http://www.scirp.org/Journal/PaperInformation.aspx?paperID=20745>.
- [89] E. Fantino, A. Chiappone, F. Calignano, M. Fontana, F. Pirri, I. Roppolo, In situ thermal generation of silver nanoparticles in 3D printed polymeric structures, *Materials (Basel)*. 9 (2016) 21–23. doi:10.3390/ma9070589.
- [90] S.J. Leigh, C.P. Pursell, J. Bowen, D.A. Hutchins, J.A. Covington, D.R. Billson, A miniature flow sensor fabricated by micro-stereolithography employing a magnetite/acrylic nanocomposite resin, *Sensors Actuators, A Phys.* 168 (2011) 66–71. doi:10.1016/j.sna.2011.03.058.
- [91] G. Gonzalez, A. Chiappone, I. Roppolo, E. Fantino, V. Bertana, F. Perrucci, L. Scaltrito, F. Pirri, M. Sangermano, Development of 3D printable formulations containing CNT with enhanced electrical properties, *Polymer (Guildf)*. 109 (2017) 246–253. doi:10.1016/j.polymer.2016.12.051.
- [92] I. Cooperstein, M. Layani, S. Magdassi, 3D printing of porous structures by UV-curable O/W emulsion for fabrication of conductive objects, *J. Mater. Chem. C*. 3 (2015) 2040–2044. doi:10.1039/C4TC02215G.
- [93] R.M. Matthias Gurr, Daniel Hofmann, Michael Ehm, Yi Thomann, Rainer Kubler, Acrylic Nanocomposite Resins for Use in Stereolithography and Structural Light Modulation Based Rapid Prototyping and Rapid Manufacturing Technologies, *Adv. Funct. Mater.* (2008) 2390–2397. doi:10.1002/adfm.200800344.
- [94] J.H. Sandoval, R.B. Wicker, Functionalizing stereolithography resins: effects of dispersed multi-walled carbon nanotubes on physical properties, *Rapid Prototyp. J.* 12 (2006) 292–303. doi:10.1108/13552540610707059.
- [95] C. Baker, A. Pradhan, L. Pakstis, D.J. Pochan, S.I. Shah, Synthesis and antibacterial properties of silver nanoparticles, *J. Nanosci. Nanotechnol.* 5 (2005) 244–249. doi:10.1166/jnn.2005.034.
- [96] M. He, Y. Zhao, B. Wang, Q. Xi, J. Zhou, Z. Liang, 3D Printing Fabrication of Amorphous Thermoelectric Materials with Ultralow Thermal Conductivity, *Small*. 11 (2015) 5889–5894. doi:10.1002/smll.201502153.
- [97] Z.L. Yuanyuan Zhang, Houmin Li, Xi Yang, Tao Zhang, Kaiqiang Zhu, Wei Si, H. Sun, Additive Manufacturing of Carbon Nanotube- Photopolymer Composite Radar Absorbing Materials Yuanyuan, *Polym. Compos.* (2016). doi:10.1002/pc.
- [98] J.H. Sandoval, K.F. Soto, L.E. Murr, R.B. Wicker, Nanotailoring photocrosslinkable epoxy resins with multi-walled carbon nanotubes for stereolithography layered manufacturing, *J. Mater. Sci.* 42 (2007) 156–165. doi:10.1007/s10853-006-1035-2.
- [99] D. Lin, S. Jin, F. Zhang, C. Wang, Y. Wang, C. Zhou, G.J. Cheng, 3D stereolithography printing of graphene oxide reinforced complex architectures, *Nanotechnology*. 26 (2015) 434003. doi:10.1088/0957-4484/26/43/434003.
- [100] S. Kumar, M. Hofmann, B. Steinmann, E.J. Foster, C. Weder, Reinforcement of Stereolithographic Resins for Rapid Prototyping with Cellulose Nanocrystals, *Appl. Mater. Interfaces*. (2012).
- [101] M.P. Lee, G.J.T. Cooper, T. Hinkley, G.M. Gibson, M.J. Padgett, L. Cronin, Development of a 3D printer using scanning projection stereolithography, *Sci. Rep.* 5 (2015) 9875. doi:10.1038/srep09875.

- [102] A. Ronca, L. Ambrosio, D.W. Grijpma, Preparation of designed poly(d,l-lactide)/nanosized hydroxyapatite composite structures by stereolithography, *Acta Biomater.* 9 (2013) 5989–5996. doi:10.1016/j.actbio.2012.12.004.
- [103] E. Fantino, A. Chiappone, I. Roppolo, D. Manfredi, R. Bongiovanni, C.F. Pirri, F. Calignano, 3D Printing of Conductive Complex Structures with in Situ Generation of Silver Nanoparticles, *Adv. Mater.* 28 (2016) 3712–3717. doi:10.1002/adma.201505109.
- [104] C. Esposito Corcione, R. Striani, F. Montagna, D. Cannoletta, Organically modified montmorillonite polymer nanocomposites for stereolithography building process, *Polym. Adv. Technol.* 26 (2015) 92–98. doi:10.1002/pat.3425.
- [105] Z. Weng, Y. Zhou, W. Lin, T. Senthil, L. Wu, Structure-property relationship of nano enhanced stereolithography resin for desktop SLA 3D printer, *Compos. Part A Appl. Sci. Manuf.* 88 (2016) 234–242. doi:10.1016/j.compositesa.2016.05.035.
- [106] M.P. De Beer, H.L. Van Der Laan, M.A. Cole, R.J. Whelan, M.A. Burns, T.F. Scott, Rapid, continuous additive manufacturing by volumetric polymerization inhibition patterning, *J. Phys. A Math. Theor.* 52 (2019). doi:10.1126/sciadv.aau8723.
- [107] X. Chen, H.O.T. Ware, E. Baker, W. Chu, J. Hu, C. Sun, The Development of an All-polymer-based Piezoelectric Photocurable Resin for Additive Manufacturing, *Procedia CIRP.* 65 (2017) 157–162. doi:10.1016/j.procir.2017.04.025.
- [108] S. Bilgi, C. Demir, Identification of photooxidation degradation products of C.I. Reactive Orange 16 dye by gas chromatography-mass spectrometry, *Dye. Pigment.* 66 (2005) 69–76. doi:10.1016/j.dyepig.2004.08.007.
- [109] D. Yugang, Z. Yuan, T. Yiping, L. Dichen, Nano-TiO₂-modified photosensitive resin for RP, *Rapid Prototyp. J.* 17 (2011) 247–252. doi:10.1108/13552541111138360.
- [110] J. Vovrosh, G. Voulazeris, P.G. Petrov, J. Zou, Y. Gaber, L. Benn, D. Woolger, M.M. Attallah, V. Boyer, K. Bongs, M. Holynski, Additive manufacturing of magnetic shielding and ultra-high vacuum flange for cold atom sensors, *Sci. Rep.* (2018). doi:10.1038/s41598-018-20352-x.
- [111] R.D. Farahani, M. Dub, D. Therriault, Three-Dimensional Printing of Multifunctional Nanocomposites: Manufacturing Techniques and Applications, *Adv. Mater.* (2016) 5794–5821. doi:10.1002/adma.201506215.
- [112] D.C.C. Okpala, The Benefits and Applications of Nanocomposites, *Int. J. Adv. Eng. Technol.* 5 (2014) 12–18. doi:10.1017/S0022226700013931.
- [113] B. Fadeel, Clear and present danger? Engineered nanoparticles and the immune system, *Swiss Med. Wkly.* 142 (2012). doi:10.4414/smw.2012.13609.
- [114] P.M. Ajayan, L.S. Schadler, P. V Braun, *Nanocomposite Science and Technology*, 2003. doi:10.1016/S1369-7021(03)01139-8.
- [115] Sigma-Aldrich, Product Specification: poly(ethylene glycol) diacrylate - average Mn 250, (n.d.) 63103.
- [116] B. Tiller, A. Reid, B. Zhu, J. Guerreiro, R. Domingo-roca, J.C. Jackson, J.F.C. Windmill, Piezoelectric Microphone via a Digital Light Processing 3D Printing Process, *Mater. Des.* (2019) 107593. doi:10.1016/j.matdes.2019.107593.
- [117] Sigma-Aldrich, Poly(ethylene glycol) diacrylate - average Mn 700, (n.d.) 63103.
- [118] H.A. Photoinitiator, Ebecryl 11, (2013) 2013.
- [119] L. Stream, O.F. The, M.R. Process, PETIA, (2017) 2–3.
- [120] Ebecryl 7100, (2017) 7100.
- [121] I. Della, S. Preparato, E. Della Società, TMPTA SDS, 44 (2004) 4–6.
- [122] E. ROSE, *The Condensed Chemical Dictionary*, Soil Sci. (1957). doi:10.1097/00010694-195702000-00012.

- [123] M. Gaboardi, A. Bliersbach, G. Bertoni, M. Aramini, G. Vlahopoulou, D. Pontiroli, P. Mauron, G. Magnani, G. Salviati, A. Züttel, M. Riccò, Decoration of graphene with nickel nanoparticles: study of the interaction with hydrogen, *J. Mater. Chem. A*. 2 (2014) 1039–1046. doi:10.1039/C3TA14127F.
- [124] L. Staudenmaier, Verfahren zur Darstellung der Graphitsäure, *Berichte Der Dtsch. Chem. Gesellschaft*. (1899). doi:10.1002/cber.18990320208.
- [125] R. Muszynski, B. Seger, P. V. Kamat, Decorating graphene sheets with gold nanoparticles, *J. Phys. Chem. C*. (2008). doi:10.1021/jp800977b.
- [126] H.K. Jeong, Y.P. Lee, M.H. Jin, E.S. Kim, J.J. Bae, Y.H. Lee, Thermal stability of graphite oxide, *Chem. Phys. Lett.* (2009). doi:10.1016/j.cplett.2009.01.050.
- [127] T. Szabó, O. Berkesi, P. Forgó, K. Josepovits, Y. Sanakis, D. Petridis, I. Dékány, Evolution of surface functional groups in a series of progressively oxidized graphite oxides, *Chem. Mater.* (2006). doi:10.1021/cm060258+.
- [128] M.J. McAllister, J.L. Li, D.H. Adamson, H.C. Schniepp, A.A. Abdala, J. Liu, M. Herrera-Alonso, D.L. Milius, R. Car, R.K. Prud'homme, I.A. Aksay, Single sheet functionalized graphene by oxidation and thermal expansion of graphite, *Chem. Mater.* (2007). doi:10.1021/cm0630800.
- [129] H.C. Schniepp, J.L. Li, M.J. McAllister, H. Sai, M. Herrera-Alonso, D.H. Adamson, R.K. Prud'homme, R. Car, D.A. Seville, I.A. Aksay, Functionalized single graphene sheets derived from splitting graphite oxide, *J. Phys. Chem. B*. (2006). doi:10.1021/jp060936f.
- [130] D.Z. Chen, Y. Zhu, M.D. Stoller, W. Cai, A. Velamakanni, R.D. Piner, D. Chen, R.S. Ruoff, Exfoliation of Graphite Oxide in Propylene Carbonate and Thermal Oxide Platelets, *ACS Nano*. 4 (2010) 1227–1233. doi:10.1021/nn901689k.
- [131] D.C. Elias, R.R. Nair, T.M.G. Mohiuddin, S. V. Morozov, P. Blake, M.P. Halsall, A.C. Ferrari, D.W. Boukhvalov, M.I. Katsnelson, A.K. Geim, K.S. Novoselov, Control of graphene's properties by reversible hydrogenation: Evidence for graphane, *Science* (80-.). (2009). doi:10.1126/science.1167130.
- [132] B. FrantzDale, M. Keeter, Formlabs_OpenFL.pdf, (n.d.). https://formlabs.com/media/upload/Formlabs_OpenFL.pdf.
- [133] A. Chiappone, I. Roppolo, E. Naretto, E. Fantino, F. Calignano, M. Sangermano, F. Pirri, Study of graphene oxide-based 3D printable composites: Effect of the in situ reduction, *Compos. Part B Eng.* 124 (2017) 9–15. doi:10.1016/j.compositesb.2017.05.049.
- [134] S. Jradi, L. Balan, X.H. Zeng, J. Plain, D.J. Lougnot, P. Royer, R. Bachelot, S. Akil, O. Soppera, L. Vidal, Spatially controlled synthesis of silver nanoparticles and nanowires by photosensitized reduction, 095605 (2010). doi:10.1088/0957-4484/21/9/095605.
- [135] C. Sciancalepore, F. Moroni, M. Messori, F. Bondioli, Acrylate-based silver nanocomposite by simultaneous polymerization–reduction approach via 3D stereolithography, *Compos. Commun.* 6 (2017) 11–16. doi:10.1016/j.coco.2017.07.006.
- [136] ASTM standard D695, Standard Test Method for Compressive Properties of Rigid Plastics, *ASTM Int.* (2015) 1–8. doi:10.1520/D0695-15.2.
- [137] J.D. Ferry, H.S. Myers, Viscoelastic Properties of Polymers, *J. Electrochem. Soc.* (2007). doi:10.1149/1.2428174.
- [138] R.M. Silverstein, F.X. Webster, D.J. Kiemle, Silverstein - Spectrometric Identification of Organic Compounds 7th ed, 2005. <http://www.dcne.ugto.mx/Contenido/MaterialDidactico/amezquita/Analitica4/Silverstein - Spectrometric Identification of Organic Compounds 7th ed.pdf>.
- [139] B. Kiran, K. Manga, Y. Zhou, Y. Yan, K.P. Loh, Multilayer Hybrid Films Consisting of

- Alternating Graphene and Titania Nanosheets with Ultrafast Electron Transfer and Photoconversion Properties, (2009) 3638–3643. doi:10.1002/adfm.200900891.
- [140] Y. Wang, Y. Wang, H. Zhang, L. Zhang, A Novel Approach to Prepare a Gradient Polymer with a Wide Damping Temperature Range by In-Situ Chemical Modification of Rubber During Vulcanization, (2006) 1162–1167. doi:10.1002/marc.200600106.
- [141] C. Sciancalepore, Non-hydrolytic sol-gel synthesis and reactive suspension method: an innovative approach to obtain magnetite-epoxy based nanocomposite materials, 2016.
- [142] G. Barrera, C. Sciancalepore, M. Messori, P. Allia, P. Tiberto, F. Bondioli, Magnetite-epoxy nanocomposites obtained by the reactive suspension method: Microstructural, thermo-mechanical and magnetic properties, *Eur. Polym. J.* 94 (2017) 354–365. doi:10.1016/j.eurpolymj.2017.07.022.
- [143] L.T.D. HIROAKI MIYAGAWA, MICHAEL J. RICH, Amine-Cured Epoxy/Clay Nanocomposites. II. The Effect of the Nanoclay Aspect Ratio, *J. Polym. Sci. Part B Polym. Phys.* 42 (2004) 4391–4400. doi:10.1002/polb.20289.
- [144] S. Mondal, D. Martin, Hydrolytic degradation of segmented polyurethane copolymers for biomedical applications, *Polym. Degrad. Stab.* 97 (2012) 1553–1563. doi:10.1016/j.polymdegradstab.2012.04.008.
- [145] C.R. Wold, M.D. Soucek, Viscoelastic and thermal properties of linseed oil-based ceramer coatings, *Macromol. Chem. Phys.* 201 (2000) 382–392. doi:10.1002/(SICI)1521-3935(20000201)201:3<382::AID-MACP382>3.0.CO;2-9.
- [146] A.L. Goffin, J.M. Raquez, E. Duquesne, G. Siqueira, Y. Habibi, A. Dufresne, P. Dubois, Poly(ϵ -caprolactone) based nanocomposites reinforced by surface-grafted cellulose nanowhiskers via extrusion processing: Morphology, rheology, and thermo-mechanical properties, *Polymer (Guildf)*. 52 (2011) 1532–1538. doi:10.1016/j.polymer.2011.02.004.
- [147] S. Pashneh-Tala, R. Owen, H. Bahmaee, S. Rekštytė, M. Malinauskas, F. Claeysens, Synthesis, Characterization and 3D Micro-Structuring via 2-Photon Polymerization of Poly(glycerol sebacate)-Methacrylate–An Elastomeric Degradable Polymer, *Front. Phys.* 6 (2018). doi:10.3389/fphy.2018.00041.
- [148] W. Zhu, J. Li, Y.J. Leong, I. Rozen, X. Qu, R. Dong, Z. Wu, W. Gao, P.H. Chung, J. Wang, S. Chen, 3D-Printed Artificial Microfish, *Adv. Mater.* 27 (2015) 4411–4417. doi:10.1002/adma.201501372.
- [149] L. Vigna, A. Fasoli, M. Cocuzza, F.C. Pirri, L.D. Bozano, M. Sangermano, A Flexible, Highly Sensitive, and Selective Chemiresistive Gas Sensor Obtained by In Situ Photopolymerization of an Acrylic Resin in the Presence of MWCNTs, *Macromol. Mater. Eng.* 1800453 (2018) 1800453. doi:10.1002/mame.201800453.
- [150] O.Y. Erenkov, P. V. Igumnov, V.L. Nikishechkin, Mechanical properties of polymer composites, *Russ. Eng. Res.* (2010). doi:10.3103/s1068798x1004012x.
- [151] S.Y. Fu, X.Q. Feng, B. Lauke, Y.W. Mai, Effects of particle size, particle/matrix interface adhesion and particle loading on mechanical properties of particulate-polymer composites, *Compos. Part B Eng.* (2008). doi:10.1016/j.compositesb.2008.01.002.
- [152] D. Morselli, F. Bondioli, M. Sangermano, M. Messori, Photo-cured epoxy networks reinforced with TiO₂ in-situ generated by means of non-hydrolytic sol-gel process, *Polymer (Guildf)*. 53 (2012) 283–290. doi:10.1016/j.polymer.2011.12.006.
- [153] H.W. Lu, S.H. Liu, X.L. Wang, X.F. Qian, J. Yin, Z.K. Zhu, Silver nanocrystals by hyperbranched polyurethane-assisted photochemical reduction of Ag⁺, *Mater. Chem. Phys.* (2003). doi:10.1016/S0254-0584(03)00147-0.
- [154] D. Lin, C. Ye, Y. Liao, S. Suslov, R. Liu, G.J. Cheng, Mechanism of fatigue performance

enhancement in a laser sintered superhard nanoparticles reinforced nanocomposite followed by laser shock peening, in: *J. Appl. Phys.*, 2013. doi:10.1063/1.4799154.

- [155] D. Lin, C. Richard Liu, G.J. Cheng, Single-layer graphene oxide reinforced metal matrix composites by laser sintering: Microstructure and mechanical property enhancement, *Acta Mater.* (2014). doi:10.1016/j.actamat.2014.07.038.
- [156] D. Lin, C. Richard Liu, G.J. Cheng, Laser sintering of separated and uniformly distributed multiwall carbon nanotubes integrated iron nanocomposites, *J. Appl. Phys.* (2014). doi:10.1063/1.4869214.
- [157] S. Dul, A.P. Id, L. Fambri, Effects of the Nanofillers on Physical Properties of Acrylonitrile-Butadiene-Styrene Nanocomposites: Comparison of Graphene Nanoplatelets and Multiwall Carbon Nanotubes, (2018). doi:10.3390/nano8090674.
- [158] M.A. Rafiee, J. Rafiee, Z. Wang, H. Song, Z.Z. Yu, N. Koratkar, Enhanced mechanical properties of nanocomposites at low graphene content, *ACS Nano.* (2009). doi:10.1021/nn9010472.
- [159] H. Fan, L. Wang, K. Zhao, N. Li, Z. Shi, Z. Ge, Z. Jin, Fabrication, mechanical properties, and biocompatibility of graphene-reinforced chitosan composites, *Biomacromolecules.* (2010). doi:10.1021/bm100470q.

Appendix A - Publications

1.1. Review

1.1.1.G. **Taormina**, C. Sciancalepore, M. Messori, F. Bondioli "3D printing processes for photocurable polymeric materials: technologies, materials and future trend" Journal of applied biomaterials & functional materials

1.2. Original research articles

1.2.1.G **Taormina**, Corrado Sciancalepore, Federica Bondioli, Massimo Messori "Special resins for stereolithography: In situ generation of silver nanoparticles" Polymers 10 (2), 212

Appendix B – Patent

- Request number: 102018000008679

Request presented on: 18/09/2018

Title: METODO E MATERIALI PER LA FABBRICAZIONE DI TAMPONI PER L'INDUSTRIA CERAMICA (Method and materials for the fabrication of pads for ceramic industry)

Inventors: G. TAORMINA, F. BONDIOLI, M. MESSORI, C. SCIANCALEPORE

Appendix C - Conferences

Oral presentations

- 1.1. G. Taormina, C. Sciancalepore, M. Messori, F. Bondioli

“Preparation of acrylate-based silver nanocomposite by simultaneous polymerization-reduction approach via 3D printing technique”

Macrogiovani 2017, Trento, June 22-23 2017

- 1.2. G. Taormina, C. Sciancalepore, M. Messori, F. Bondioli

“Preparation of acrylate-based silver nanocomposite by simultaneous polymerization–reduction approach via 3D printing technique”

3rd Parma Nano-day 2017, Parma, July 12-14 2017

- 1.3. Massimo Messori, Corrado Sciancalepore, Gabriele Taormina and Federica Bondioli

“Photo-curable resins modified with in situ generated silver nanoparticles for stereolithography”

Nordic Polymer Days 2017, Stockholm, June 19-21 2017

- 1.4. C. Sciancalepore, G. Taormina, M. Messori, F. Bondioli

“Innovative acrylate-based silver nanocomposite resin for 3D stereolithography”

Convegni Nazionali INSTM e AIMAT 2017, Ischia, July 12-15 2017

- 1.5. Gabriele Taormina, Corrado Sciancalepore, Massimo Messori, Federica Bondioli

“Advanced resins for stereolithography: In situ generation of silver nanoparticles”

Poster presentations

- 1.6. G. Taormina, C. Sciancalepore, F. Bondioli, M. Messori

“Preparation of acrylate-based silver nanocomposite by simultaneous polymerization-reduction approach via 3D printing technique”

Eupoc 2017, Gargnano, May 21-25 2017

- 1.7. G. Taormina, C. Sciancalepore, M. Messori, F. Bondioli

“Preparation of acrylate-based silver nanocomposite by simultaneous polymerization-reduction approach via 3D printing technique”

Macrogirovani 2017, Trento, June 22-23 2017

- 1.8. G. Taormina, C. Sciancalepore, M. Messori, F. Bondioli

“Preparation of acrylate-based silver nanocomposite by simultaneous polymerization–reduction approach via 3D printing technique”

3rd Parma Nano-day 2017, Parma, July 12-14 2017

- 1.9. C. Sciancalepore, G. Taormina, M. Messori, F. Bondioli, Photo-curable resins modified with in situ generated silver nanoparticles for additive manufacturing, *Advances in Functional Materials*, 14-17 August 2017, Los Angeles, CA

- 1.10. M. Messori, C. Sciancalepore, G. Taormina, F. Bondioli

Photo-curable resins modified with in situ generated silver nanoparticles for stereolithography

Italian-Nordic Polymer Future Workshop

14-15 September 2017, Pisa (Italy)

